HIGH-FIELD ^{31}P MAGNETIC RESONANCE SPECTROSCOPY (MRS) IN HUMAN BRAIN

A DISSERTATION

SUBMITTED TO THE FACULTY OF THE GRADUATE SCHOOL

OF THE UNIVERSIT OF MINNESOTA

BY

Hongyan Qiao

IN PARTIAL FULFILLMENT OF THE REQUIREMENTS

FOR THE DEGREE OF

DOCTOR OF PHILOSOPHY

ADVISOR: Wei Chen, Ph. D

January 2010

Acknowledgements

I would like to acknowledge the efforts, guidance, and support of my advisor, Wei Chen, who has had a direct impact on my personal and professional life. Thank you for your support, and thank you for teaching me how to do science.

I would like to thank Bruce Hammer, James Holte and Jianyi Zhang who generously serve on my thesis committee and provide expert opinions and feedback.

I would also like to thank Fei Du for his kind help and advice on my thesis.

I would also like to take this time to thank Xiaohong Zhu, Xiaoliang Zhang, Nanyin Zhang and Yi Zhang, for your support and help during my Ph. D study.

Thank you, Brian Hanna, Janis Zeltins and John Strupp for your technical computer support.

Thank you, Kamil Ugurbil for your earlier innovate work which opened the doors at the University of Minnesota to study of *in vivo* human brain MRI/MRS at ultra high fields.

I would like to thank my parents and family, whose support and guidance have helped me sail through difficult chapters of my life. My father and mother have been ultra-supportive, and this thesis is dedicated to their efforts.

Dedication

This dissertation is dedicated to my family.

Abstract

The pioneer paper of Moon & Richards in 1973 recorded the ^{31}P NMR spectrum of red blood cells. After this breakthrough, the application of ^{31}P NMR to biological systems has become more and more popular. The range of those ^{31}P NMR studies is pretty broad, from the simple observation of anaerobic metabolism to the elegant combination of physiology and spectroscopy. However, the severe overlap of multiplet resonances and relatively low detection sensitivity in the ^{31}P spectra acquired at low fields pose many limitations in *in vivo* applications. These limitations can be potentially overcome at high fields. The goal of this project is to study the advantages of high-field ^{31}P MRS in human brain through the following specific aims:

- To investigate the improvement of sensitivity and spectral resolution of *in vivo* ^{31}P MRS in human brain at high fields (4T, 7T) and their field dependence;
- To achieve 3D ^{31}P chemical shift imaging covering whole human brain, quantify metabolite concentrations and other physiological parameters provided by *in vivo* ^{31}P MRS, and study the bioenergetic differentiations among different brain tissues;
- To study creatine kinase enzyme activity via ^{31}P magnetization transfer experiments.

TABLE OF CONTENTS

LIST OF TABLES

LIST OF FIGURES

Chapter 5

KEY WORDS AND ABBREVIATIONS

Key Words

In vivo ^{31}P magnetic resonance spectroscopy MRS; human brain; high field; NMR sensitivity; spectral resolution; Adenosine-5'-triphosphate (ATP); bioenergetics; chemical exchange flux; human brain; Phosphocreatine (PCr); High energy phosphate metabolism; Magnetization transfer; Inversion recovery

Abbreviations

ATP	Adenosine-5'-triphosphate
ATPase	ATP sysnthase
CK	Creatine Kinase
Cr	Creatine
CSI	Chenical Shift Imaging
Ff	Forward Chemical Exchange Flux
FOV	Field of View
Fr	Reverse Chemical Exchange Flux
FSW	Fourier Series Window
GPC	Glycerophosphocholine
GPE	Glycerophosphoethanolamine
IT	Inversion Transfer
MSST	Multiple Single-site Saturation Transfer
PC	Phosphocholine
PCr	Phosphocreatine

PE	Phosphoethanolamine
Pi	Inorganic Phosphate
Pi^{ex}	Extracellular Inorganic Phosphate
RF	Radiofrequency
SAR	Absorption rate
SNR	Signal to Noise Ratio
ST	Saturation Transfer

1. INTRODUCTION

The pioneer paper of Moon & Richards in 1973 recorded the ^{31}P NMR spectrum of red blood cells. After this breakthrough, the application of ^{31}P NMR to biological systems has become more and more popular. The range of those ^{31}P NMR studies is pretty broad, from the simple observation of anaerobic metabolism to the elegant combination of physiology and spectroscopy. However, the severe overlap of multiplet resonances and relatively low detection sensitivity in the ^{31}P spectra acquired at low fields pose many limitations in *in vivo* applications. These limitations can be potentially overcome at high fields. The goal of this project is to study the advantages of high-field ^{31}P MRS in human brain.

1.1 Thesis Statement

This dissertation includes three projects directed toward studying human brain ^{31}P Magnetic Resonance Spectroscopy (MRS). The first project investigates the improvement of sensitivity and spectral resolution of *in vivo* ^{31}P MRS in human brain at high fields. The second one is focusing on human brain 3D ^{31}P chemical shift imaging. And the third one is studying human brain creatine kinase enzyme activity via ^{31}P magnetization transfer experiments. The three specific topics addressed are as follows:

- *In Vivo* ^{31}P MRS of Human Brain at High/Ultrahigh Fields: A Quantitative Comparison of Signal-to-Noise Ratio and Spectral Resolution between 4 Tesla and 7 Tesla;

- Differentiating High-energy Phosphate Metabolites and pH in Human Gray and White Matters by Using 3D ^{31}P Chemical Shift Imaging of Entire Brain at 7 Tesla;
- Non-invasively Determining Kinetic Network of ATP Metabolism in Human Brain.

2. BACKGROUND AND SIGNIFICANCE

Accessment of the intricate structure and complex function of the human brain was only available by accidental trauma or indirect chemical and biochemical techniques (i.e., *in vitro* approaches) before the development of modem neuroimaging techniques. The gross structural information about the brain can be provided by the use of X-rays and computerized tomography. However, there exists the risk for exposing the patient to ionizing radiation. On the other hand, magnetic resonance imaging (MRI) was described by Lauterbur in 1973 [1], which has the ability to non-invasively image the soft tissue structures of the human brain [2]. Nowadys, highly detailed MR images of the brain can be acquiered in the clinic or research lab on a routine basis.

MRI is primarily an anatomic imaging modality. On the other hand, magnetic resonance spectroscopy (MRS) takes advantage of the magnetic resonance phenomenon to access neurochemistry in a living brain. The research fields involving MRS are expanding rapidly. One big reason for the rapid expansion is that nuclear magnetic resonance (NMR) spectroscopy, the only physical technique routinely used in clinical research, has the ability to assess the *in vitro* or *in vivo* metabolism at the molecular level under both normal and pathological conditions.

2.1 Brief History

The physical principles of nuclear magnetic resonance (NMR) were discovered by Bloch et al. (1946) and Purcell et al. (1946) [3, 4] independently. And the MRS technology has been introduced into clinical research later. NMR played an important role in the nondestructive biochemical analysis of chemical compounds in the 1950's and

1960's. In early seventies, NMR technology was applied to a biologic system. In Moon and Richardsis paper, they used NMR to study suspensions of intact erythrocytes (1973) [5, 6]. Eventually, the advances in nuclear magnetic resonance technology allowed for the *in vivo* assessment of various tissue metabolisms in animals, such as mice and rats. Ackerman et al. studied (1980) the rat brain by using a surface coil. This was the first demonstration that MRS could be applied to the *in vivo* study of brain biochemistry. Later in 1983, the first *in vivo* spectroscopic studies of the human brain were published. The studies were performed on neonates suffering from birth asphyxia and other neurological disorders. And nowadays, MRS has rapidly expanded into a versatile clinical research tool. With this powerful tool, the researchers are able to investigate the cerebral physiology, biochemistry, bioenergetics and pathology.

2.2 Physical Principles of Nuclear Magnetic Resonance

Technologically, MRS is very similar to MRI. And both techniques use the same hardware (computer, magnet, etc.) and are based on the same NMR principle. In this section, we will have a brief overview of the fundamental physical basis of nuclear magnetic resonance.

In all atoms, nuclear particles spin about an atomic axis creating a small magnetic field. Spins of atoms with even numbers of electrons and protons (i.e. $^{4}H_{e}$ with 2 protons and 2 neutrons) have no net magnetic moment. However, atoms with odd number of nuclear particles (i.e., ^{1}H, ^{31}P, or ^{19}F) have a net spin, resulting in a magnetic moment that may be represented as a vector. Such atoms can provide NMR signals. In the absence of

an electromagnetic field these vectors are randomly aligned, thus their vector sum cancels each other out, resulting in a net vector of zero. However, when an external magnetic field (B_0) is applied, a slight majority of the nuclei align in the direction of the magnetic field. A net magnetic vector results in along the direction of B_0. This is defined as longitudinal magnetization and its magnitude is dependent on the number of spins (see Fig 2-1).

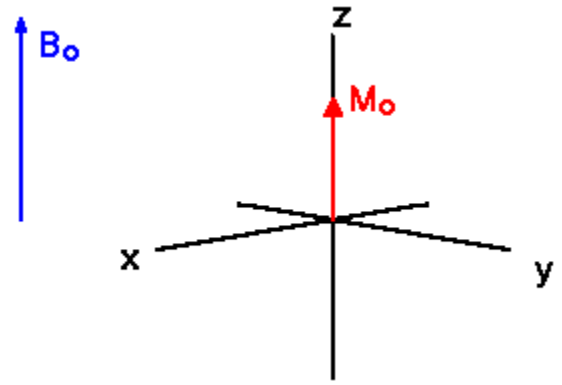

Figure 2-1 Vector sum aligned along B_0 representing the magnitude of longitudinal magnetization.

In the presence of a magnetic field, the aligned nuclei precess around the axis of B_0 in accordance with the law of conservation of angular momentum. The rate of precession (termed the Larmor frequency) is determined by both the gyromabnetic ratio of that particular nuclei and the strength of the magnetic field to which the nucleus is exposed. As the magnitude of B_0 increases, the rate of precession also increases. If a ratio-frequency (RF) field (B_1) is applied in an orthogonal direction to B_0, nuclei precessing at the same frequency as the RF pulse are excited to the higher energy state.

This makes it possible to selectively excite a type of nucleus (i.e. ^{1}H ^{31}P, or ^{19}F) by choosing the proper frequency of the RF pulse.

The RF magnetic field (B_1) shifts the direction of the net magnetic vector away from the axis of B_0. This is termed nutation and the resultant vector represents the transverse magnetization of the nuclei. The angle to which the net vector has been nutated away from B_0 is called the flip angle θ. The magnitude of the transverse magnetization is determined by the degree of θ and the magnitude of the longitudinal magnetization prior to the application of the RF pulse (see Fig 2-2).

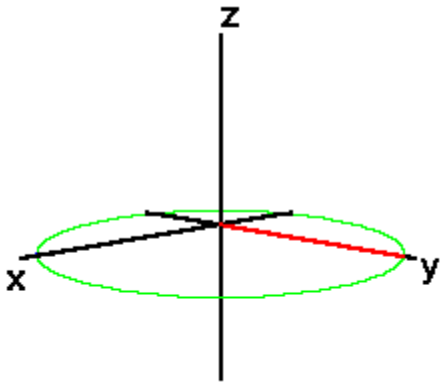

Figure 2-2 Vector sum representation of the magnitude and direction of the resultant transverse magnetization.

The nutated nuclei continue to precess around B_0 and induce an electromotive force, which can be detected by a RF coil. This signal is often termed the free induction decay (FID). When the RF pulse is discontinued the nuclei slowly realign in the direction of B_0 to re-establish longitudinal magnetization. The speed of such realignment depends upon the longitudinal relaxation time defined by T_1.

MRI measures the spatial distribution of magnetic proton nuclei by using gradient coils to produce a linear dependence of the B_0 field on position during the acquisition of NMR signal, thereby establishing a direct relationship between Larmor frequency and spatial location. In this case, a single resonance is usually assumed. On the other hand, MRS takes advantage of subtle differences in the magnetic resonance phenomenon (or chemical shift) to provide chemical information related to the fingerprint of tissue metabolites rather than structural images. MRS generally uses no magnetic field gradient at the time of FID signal detection. For a given nucleus type, any change in the observed frequency is due to small difference in the local magnetic field experienced by each nucleus. This difference in local magnetic field depends on the molecular constituents of a biological sample or *in vivo* tissue based on the difference in the observed chemical shifts [7].

2.3 Localized Magnetic Resonance Spectroscopy

The proton concentration of water in the brain tissue is approximately 100M while that of phosphocreatinine and adenosine triphosphate are only in the range of few mM. Generally speaking, MRS is less sensitive than MRI because the concentrations of

atoms measured by MRS are several orders of magnitude less than the concentration of hydrogen used in MRI [8]. Therefore, the initial limitation to the clinical application of MRS was a lack of ability to provide NMR spectra from specific volumes within the body.

There are, however, two methods that allow spatial localization of the acquired spectra in general use today. One is single/multiple voxel approach and the other is spectroscopic imaging approach. These localization approaches can be combined with other methods with various functions via RF pulse sequence design for obtaining desired *in vivo* MRS.

2.3.1 Spatial Localization via Voxel Approach

There are many spatial localization approaches which allow simultaneous acquisition of *in vivo* MR spectra from several voxels in different locations. These approaches are based on single-voxel methods [9-11] or multiple-voxel methods [12-17]. The most commonly used single-voxel MRS localization techniques are the image-selected *in vivo* spectroscopy (ISIS) method [10], the stimulated echo acquisition mode (STEAM) method [9], and the point resolved spectroscopy method (PRESS) [11], which can achieve spatial localization within the single sampling (shot). The ISIS method requires multiple samplings (shots) for achieving spatial localization. In the following paragraphs, let's look at the PRESS pulse sequence to explore how to achieve a single voxel localized *in vivo* ^{1}H MR spectrum in great depth.

In Figure 2-3, there is a PRESS pulse sequence which achieves a 3D spatial localization in a single shot via the combination of three frequency-selective RF pulses and multiple gradients in three orthogonal directions. The Hahn spin echo sequence is modified by adding the second 180° refocusing RF pulse. Each frequency-selective (shaped) RF pulse [18] is applied in the presence of slice-selective gradient (Gs; the trapezoid shaped gradients in Figure 2-3) for achieving a slab selection in the direction of the gradient applied. The following equations illustrate how to calculate the slab thickness (ΔL):

$$\Delta L_i(cm) = \frac{\Delta \varpi_i}{G_{s,i}} (G_{s,i}\ units: \quad Hz/cm)] \qquad [2-1a]$$

where the gradient orientation is x, y, or z; $\Delta\omega_i$ (Hz) is the bandwidth at the half height of the frequency-selective RF pulse profile, or

$$\Delta L_i(cm) = \frac{\Delta \varpi_i}{\gamma \cdot G_{s,i}} 10^{-2} (G_{s,i} \quad units: \quad Gauss/cm) \qquad [2-1b]$$

the unit of γ is MHz/T which is listed in Table 2-1 [18]. The most commonly used RF pulse shape is based on sinc or Gauss waveform. To cancel the NMR signals from the outside of the selected slab, the crusher gradients (the half-circular shaped gradients in Figure 2-3) are usually applied in three orientations. With the application of crusher gradients, only the NMR signal from the selected voxel can be refocused and detected during the FID acquisition, and the NMR magnetizations from the spins located outside

the voxel are dephased and canceled. The voxel size can be determined by properly choosing the parameters of $\Delta\omega_i$ and $G_{s,i}$ according to Eq. [2-1].

Isotope	Spin	Natural Abundance (%)	Magnetogyric Ratio (γ) (MHz T^{-1})	Frequency Ratio (%)	Relative Receptivity
^{1}H	1/2	99.99	42.57	100.00	1.000
^{31}P	1/2	100	17.25	40.48	6.65×10^{-2}
^{13}C	1/2	1.07	10.71	25.15	1.70×10^{-4}
^{17}O	5/2	0.037	−5.774	13.56	1.11×10^{-5}

Table 2-1 Nuclear spin properties

There is one practical complication of *in vivo* MRS localization, which is so-called chemical shift artifact due to the differences between the chemical shifts (σ) of resonances observed in the same *in vivo* MR spectrum as compared with the RF pulse carry frequency (f_c). The displacement (ΔDi in cm) caused by the chemical shift artifact can occur in all three orientations and can be estimated by the following equation:

$$\Delta D_{j,i}(cm) = \frac{\Delta\delta_i}{G_{s,i}}$$

where $\Delta\sigma_j = \sigma_j - f_c$; and σ_j is the chemical shift of spin j (Hz). The total displacement (ΔD_{jt}) along the diagonal direction in the selected voxel is given by:

$$\Delta D_{j,t}(cm) = \sqrt{\Delta D_{j,x}^2 + \Delta D_{j,y}^2 + \Delta D_{j,z}^2}$$

Maximal $G_{s,i}$ should be used to minimize the chemical shift artifact. However, there are several limitations to increase the $G_{s,i}$, such as the achievable maximal gradient strength of the gradient coil itself and the bandwidth of a shaped pulse and the desired voxel size governed by Eq. [2-1]. In addition, the chemical shift artifact will get worsen at higher field strength (B_0) because $\Delta\sigma_j$ in Hz unit is proportionally increased as a function of B_0, though $\Delta\sigma_j$ in ppm unit is independent on B_0.

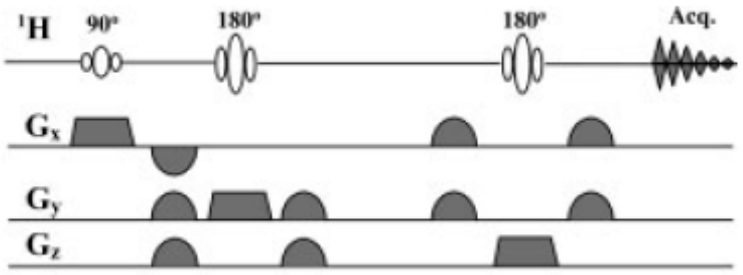

Figure 2-3 RF pulse sequence design and spatial localization. A typical PRESS spin-echo pulse sequence combined with slice selection in three orientations for achieving single-voxel localization in a single scan. The trapezoid shaped gradients are used for slice selection and the half-circular shaped gradients are the crush gradients.

2.3.2 Spatial Localization via Spectroscopic Imaging Approach

There are limitations for the single- or multiple-voxel spatial localization approaches, such as only a few regions of interest can be studied. Spectroscopic imaging (or chemical shift imaging, CSI) techniques can be used to overcome this limitation.

Phase-encoding gradients are the major components introduced in the CSI approach. These gradients are applied between the excitation RF pulse and the FID acquisition [19, 20]. Three orthogonal phase-encoding gradients with multiple increments can be used simultaneously for achieving a three-dimensional (3D) CSI. The k-space parameters in three orthogonal directions (i.e., $k_x = \gamma G_{p,x}\tau_p$, $k_y = \gamma G_{p,y}\tau_p$ and $k_z = \gamma G_{p,z}\tau_p$) are commonly used for describing the spatial localization of CSI, where τ_p is the duration of the phase-encoding gradient; $G_{p,x}$, $G_{p,y}$, and $G_{p,z}$ are the phase-encoding gradient along the x, y, and z direction, respectively. The FID signal at a specific location defined by the x, y, and z coordinates can be calculated by operating the 3D Fourier transform of the raw FID signal acquired in the k-space defined by F(kx, ky, kz, t) where t is the FID acquisition time according to the following equation:

$$F(x,y,z,t) = \int_{-\infty}^{+\infty}\int_{-\infty}^{+\infty}\int_{-\infty}^{+\infty} F(Kx,Ky,Kz,t)\cdot e^{i(xKx+yKy+zKz)}\,dKx\,dKy\,dKz$$

Then, the localized CSI spectrum can be derived by using another 1D Fourier transform that converts the FID signal from the time domain into the frequency domain according to the following formula:

$$s(x,y,z,\omega) = \int_{-\infty}^{+\infty} f(x,y,z,t)\cdot e^{-i\omega t}\,dt$$

The field of view (FOV) of CSI can be determined by:

$$FOV_i = \frac{2\pi}{\Delta K_i} \qquad i = x, y, z$$

where $\Delta K_i = \gamma \tau_p \Delta G_{p,i}$, and $\Delta G_{p,I}$ is the magnitude of the phase-encoding gradient increment. The norminal voxel size in each dimension is given by

$$\Delta V_i = \frac{FOV_i}{N_i}$$

where N_i is the number of phase-encoding steps applied along the orientation defined by i. The CSI method using the conventional Fourier transform (FT) approach yields rectangular-shaped voxels with a point-spread function (PSF) defined by the sinc function. PSF can lead to a certain degree of signal leakage to and from the surrounding voxels and, consequently, the degradation of spatial localization accuracy. This problem is intensified when only limited Ni is allowed in acquiring a CSI of low-concentration metabolites.

Alternate approaches weigh the k-space sampling with the desired filters for achieving an optimal voxel shape with minimal out-of-voxel signal contamination [21-24]. The Fourier series window (FSW) filter is one favorable choice among them. This filter is based on the Fourier coefficients of a predetermined voxel shape following a practical and optimum termination of the series. A voxel spectrum in space can be generated by the summation with respect to the phase-encoding domain and this voxel position can then be shifted arbitrarily in the phase-encoding directions for generating a 3D CSI. For convenience, the voxel spatial coordinate described by the window function (W) in one spatial dimension ($\theta(r)$) is defined with a phase angle (θ_q) between 0 to 2π, then

$$W(\theta(r)-\theta_q)=\sum_{n=0}^{N-1} w_n^q \exp\{in\theta(r)\}$$

here w_n is the Fourier window coefficient. The voxel spectrum can be described by

$$S_w^q(\theta(r)-\theta_q)=\sum_{n=0}^{N-1} s_n(t) w_n^q \exp\{in\theta(r)\}$$

and $S_n(t)$ is the NMR signal in the time domain acquired in the Nth phase-encoding step. Based on the Fourier shift theorem, a localized spectrum from another location can be generated by voxel shifting by adding the term of phase shifting (φ). The shifted window function can be expressed by

$$W(\theta(r)-\theta_q-\Psi)=\sum_{n=0}^{N-1} w_n^q \exp\{in\theta(r)-\Psi\}$$

And the spectrum from the new location is given by

$$S_w^q(\theta(r)-\theta_q-\Psi)=\sum_{n=0}^{N-1} S_n(t) w_n^q \exp\{in\theta(r)-\Psi\}.$$

It has been demonstrated that the FSW approach is characterized with better sensitivity and negligible out-of-voxel contamination compared with the conventional FT approach.

One merit of CSI approach is that there is no chemical shifting artifact problem as seen in single or multiple voxel localization approaches. Therefore, it is particularly

useful for high-field *in vivo* MRS applications in which the chemical shift dispersion is linearly increased as a function of B_0.

2.4 ^{31}P NMR Studies

The first NMR measurements possibly including signals from living brain were ^{31}P spectra [25-27]. They were obtained from an anesthetized mouse inserted into an 18-mm NMR tube and studied in a conventional NMR spectrometer with radio frequency coil that surrounded the entire head; muscle probably contributed much of the signal under these circumstances. Brain spectra with less contaminated signals from other tissues first became possible when surface coils were developed [28].

2.4.1 Visible Metabolites in ^{31}P MRS

The ^{31}P NMR spectra of cells and tissues generally contain at least eight identifiable resonances [29-31]: three arising from the α, β and γ phosphates of ATP (and any other nucleoside triphosphates), a phosphocreatine peak in spectra from brain and muscle; a Pi peak with a pH-dependent chemical shift; poorly resolved phosphodiester peaks; poorly resolved phosphomonoester peaks; and finally a large broad peak that lies beneath the whole spectrum and has been variously attributed to phospholipids and bone [32-34].

With the ultra-high-field magnetic machine available for human use, it is possible to obtain a ^{31}P MRS from human brain with a higher resolution [35]. In Figure 2-4, there is a ^{31}P MRS acquired from human brain primary visual cortex at 7 T. Here, the two

peaks previously assigned to glycerophosphoethanolamine (GPE; 1.00 ppm) and glycerophosphocholine (GPC; 0.45 ppm) are completely resolved from each other at the phosphodiesters (PDE) region. In addition, the peaks assigned to phosphoethanolamine (PE; 4.21 ppm) and phosphocholine (PC; 3.75 ppm) are partially resolved at the phosphomonesters (PME) region. The large broad peak that lies beneath the whole spectrum at low field was gone.

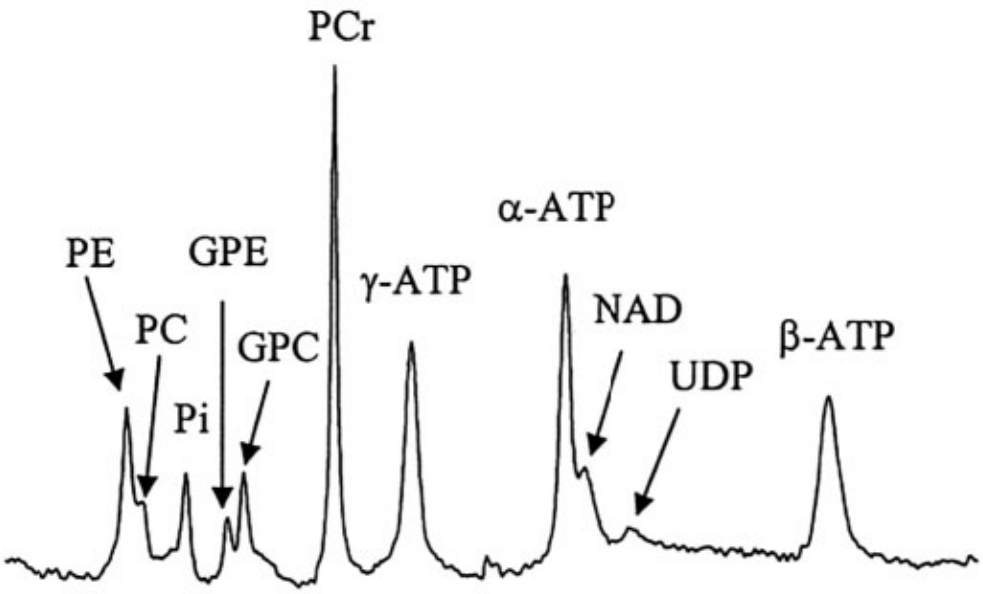

Figure 2-4 ^{31}P MRS acquired from human primary visual cortex at 7 T (TR = 3s and 128 averages).

2.4.2 Measurement of pH

NMR spectroscopy has the special capability to measure the cerebral pH *in vivo*. Invasive methods are available for use with experimental animals, and positron emission tomographic methods are under development for use in humans. However, the accuracy, safety, and relative simplicity of the ^{31}P NMR method ensure that it will be widely employed for both experimental and clinical research. From titration data, the relation of

$$pH = 6.77 + \log[(\Delta P_i - 3.29)/(5.68 - \Delta P_i)] \qquad [2\text{-}2]$$

was obtained, where ΔP_i is the chemical shift difference between the PCr and Pi resonance peaks in the unit of ppm. M_g^{2+} could affect the constants used in the above equation appreciably only in concentrations above 2.5 mM, which is well above estimates of free M_g^{2+} concentration in brain. PCr was a satisfactory internal chemical shift reference down to about pH 6.5, below which titration of PCr introduced a progressively larger error. In addition, PCr is usually depleted in metabolic states which cause severe tissue acidosis. So some external reference is necessary for pH measurements in such states.

Cerebral pH values calculated using the new formula were 7.14±0.04 (SD) and 7.13±0.03, respectively, for paralyzed, mechanically ventilated rabbits and rats under nitrous oxide analgesia [36-38]. These values are toward the alkaline end of the rather wide range reported by studies using destructive analytical methods.

2.4.3 Magnetization Transfer Experiments

By irradiating the nuclei with the same resonant frequency selectively with radio frequency energy, it is possible to 'label' the nuclei. The irradiation briefly changes their magnetization state. If such nuclei are transferred enzymatically from the molecules they were in at the time of irradiation to other molecules at a rate comparable to the lifetime of the changed magnetic state, their presence in the second molecular population may be detectable at its (different) resonant frequency [27, 39, 40]. Under favorable condition, the rate constants of enzyme-catalyzed reaction and the fluxes through it can be calculated from this measurement in living systems [41-43].

It is difficult to do magnetization transfer experiments. However they provide important, unique kinetic information about the function of some enzymes in their natural cellular environment. Beyond the resolvable discrepancies in presently available data lies the further question of how the measurable fluxes behave in different functional states of the brain [44]; results from other systems show that magnetization transfer techniques open a window on some aspects of enzyme regulation *in vivo* [45].

2.5 Significance of High-Field ^{31}P MRS

In vivo ^{31}P magnetic resonance (MR) spectroscopy can be used to assess bioenergetics of human brain noninvasively. Information provided by ^{31}P MR spectroscopy, such as phosphocreatine (PCr) and adenosine triphosphate (ATP) concentrations and their ratio, intracellular pH, and rate constant of creatine kinase (CK) reaction has been found to be useful in studying neurological diseases such as

Alzheimer's disease and Pakinson's disease [26, 46, 47] and investigating functional energetics [35, 48, 49]. However, ^{31}P MR spectroscopy on clinical 1.5 T systems often suffers from low signal-to-noise ratio (SNR), low spatial and temporal resolution, and limited spectral dispersion if proton decoupling is not applied, hampering its widespread applications. Taking advantages of high NMR detection sensitivity and the large chemical shift dispersion offered by ultra-high field strength, these problems might be alleviated [50, 51].

The acquisition of *in vivo* spectroscopic data at higher magnetic field strengths may increase the attainable quantification precision due to increased signal-to-noise ratio (SNR) and chemical shift dispersion. Several groups have shown that the SNR of spectroscopic data is increased at high field strengths (4T) compared to lower fields. Increased SNR may translate to increased metabolite measurement precision or may be traded to reduce the voxel volume from which data is collected while still maintaining adequate SNR for reliable quantification. The reduction of voxel volume is a significant advantage for the study of small (less than 1.5 cm^3) cerebral structures (i.e., caudate, putamen, thalamus), since typical *in vivo* 1.5 T volumes range from 4.5 to 8 cm^3. Other high field advantages, including increased chemical shift dispersion (to resolve overlapping metabolites) and dielectric signal enhancement (leading to increased SNR), can also contribute to increased quantification precision. A recently published article by Pfeuffer et al. describing the quantification of short echo time ^{1}H data in the rat at 9.4T has demonstrated high SNR, resolution, and consequently improved metabolite measurement precision at this field strength [52, 53].

The advantages of performing spectroscopic studies at higher field strengths have been well established for high-resolution NMR studies of proteins, nucleic acids and metabolic studies of cells, excised organs and animal models *in vivo*. However, the advantage of high-field *in vivo* NMR spectroscopy of humans has been questioned due to the technical difficulties associated with increased chemical shift dispersion errors, decreasing T_2, limited RF power, decreased gradient strengths and limitations in the design of homogeneous RF coil. Recently it has been demonstrated that these limitations can be overcome and the advantages of high-field NMR, increased SNR, improved spectral resolution and simplification of *J*-coupled spectra can be achieved. Although single-voxel localized proton spectroscopy of the human brain has been performed at 1.5T, 3T and 4T, there have been few direct comparisons between field strengths in the same subjects using the same methodology [54-56]. With the increasing availability of high-field human MR scanners, it is important to compare high-field brain spectroscopy to low-field systems. In this project, in order to estimate what spectral improvements can be expected when studying humans at field strengths significantly above 4T, we will measure human brain spectra at 7T.

The hypothesis will be tested in this project is that the high-field ^{31}P MRS can be acquired with higher spatial resolution and SNR from human brain permitting better quantification and allowing the assessment of metabolic differences and enzyme activity between the gray and white matters.

The goal of this project includes three specific aims:

- To investigate the improvement of sensitivity and spectral resolution of *in vivo* ^{31}P MRS in human brain at high fields (4T, 7T) and their field dependence;
- To achieve 3D ^{31}P chemical shift imaging covering whole human brain, quantify metabolite concentrations and other physiological parameters provided by *in vivo* ^{31}P MRS, and study the bioenergetic differentiations among different brain compartments;
- To study creatine kinase enzyme activity via ^{31}P magnetization transfer experiments.

3. QUANTITATIVE COMPARISON OF SIGNAL-TO-NOISE RATIO

3.1 *In Vivo* ^{31}P MRS of Human Brain at High/Ultrahigh Fields: A Quantitative Comparison of Signal-to-Noise Ratio and Spectral Resolution between 4 Tesla and 7 Tesla

The primary goal of this study was to establish a rigorous approach for determining and comparing the NMR detection sensitivity of *in vivo* ^{31}P MRS at different field strengths (B_0). This was done by calculating the signal-to-noise ratio (SNR) achieved within a unit sampling time at a given field strength. *In vivo* ^{31}P spectra of human occipital lobe were acquired at 4 and 7 T under similar experimental conditions. They were used to measure the improvement of the human brain ^{31}P MRS when the field strength increases from 4 to 7 T. The relaxation times and line widths of the phosphocreatine (PCr) resonance peak and the RF coil quality factors (Q) were also measured at these two field strengths. Their relative contributions to SNR at a given field strength were analyzed and discussed. The results show that *in vivo* ^{31}P sensitivity was significantly improved at 7 T as compared with 4 T. Moreover, the line-width of the PCr resonance peak showed less than a linear increase with increased B_0, which leads to a significant improvement in ^{31}P spectral resolution. These findings indicate the advantage of high-field strength to improve *in vivo* ^{31}P MRS quality in both sensitivity and spectral resolution. This advantage should improve the reliability and applicability of *in vivo* ^{31}P MRS in studying high-energy phosphate metabolism, phospholipid metabolism and cerebral biogenetics in the human at both normal and diseased states noninvasively. Finally, the approach used in this study for calculating *in vivo* ^{31}P MRS sensitivity provides a general tool in estimating the relative NMR detection sensitivity for any nuclear spin at a given field strength.

3.1.1 Introduction

In vivo ^{31}P MRS allows noninvasive assessments of many fundamental biochemical, physiological and metabolic events occurring inside living brains (e.g., [28, 35, 57, 58]). The prime information provided by *in vivo* ^{31}P MRS includes intracellular pH, intracellular free magnesium concentration ([Mg^{2+}]) and high-energy phosphate (HEP) metabolites such as adenosine triphosphate (ATP), phosphocreatine (PCr) and inorganic phosphate (Pi). These HEP metabolites are tightly linked to brain metabolism and bioenergetics through regulating the biochemical energy production (i.e., ATP synthesis) and consumption (i.e., ATP utilization). Besides the HEP metabolites, other detectable phosphate compounds in the human brain include uridine diphospho sugar (an important precursor for glycogen metabolism) [28, 35, 57, 58], nicotinamide adenine dinucleotide phosphate (NADP) involving oxidative chains, and several important phospholipid compounds that are actively involved in membrane phospholipid metabolism [59]. The steady-state phosphate metabolite signals and other physiological parameters detected by *in vivo* ^{31}P MRS have been used extensively in clinical studies. The abnormality of the phosphate signals has been linked to numerous diseases, such as brain ischemia and seizure [6, 60], epilepsy [58, 61], Alzheimer disease [26] and schizophrenia [62]. Moreover, the use of *in vivo* ^{31}P MRS combined with the magnetization transfer approach can measure the kinetics of biochemical reaction rate and enzyme activity noninvasively [40, 63-65]. These measurements should be vital in studying cerebral bioenergetics related to brain function and brain disorder.

However, the capability of *in vivo* ^{31}P MRS for biomedical applications is generally limited, especially at relatively low fields, due to the following challenges: (a) low intrinsic sensitivity because of its relatively low magnetogyric ratio (γ); (b) low NMR detectable concentrations of phosphate compounds (in the range of few millimolars); (c) overlap of adjacent resonance peaks from different phosphate compounds (e.g., in the chemical shift range near the Pi resonance peak) and (d) relatively low spatial resolution that can be achieved by *in vivo* ^{31}P MRS or spectroscopic imaging. Therefore, the applicability and reliability of *in vivo* ^{31}P MRS approaches rely on one key aspect, that is, NMR detection sensitivity and spectral resolution.

One effective approach for improving the NMR sensitivity of *in vivo* MRS is to increase magnetic field strength (B_0). The field strength for human MRI/MRS research has been increased rapidly from 3-4T to 7-9.4T. The signal-to-noise ratio (SNR) of *in vivo* ^{1}H MRS is significantly increased at high/ultrahigh fields (e.g. [66-68]). It was demonstrated that the both SNR and quality of ^{31}P MRS acquired in the human brain are improved at 2T and 4T compared to 1.5T [69-71]. We have recently qualitatively illustrated that the *in vivo* ^{31}P MRS acquired from the human occipital lobe was further improved at 7T [35]. One interesting and essential question is how much can *in vivo* ^{31}P MRS benefit at 7T compared to 4T for human applications? Addressing this question requires a sophisticated and quantitative approach to precisely determine the SNRs attainable at different field strengths. In general, there are different strategies for quantifying SNR in *in vivo* MRS. One approach is to determine the SNR of a spectrum collected with single acquisition at fully relaxed condition. However, such SNR

measurement may not be very useful because most *in vivo* MR studies are conducted at partially saturated condition by using a much shorter repetition time (TR) in comparison with five times of longitudinal relaxation time (T_1). This allows signal averaging within limited sampling time to gain SNR. Therefore, it is essential to determine the SNR of NMR signal acquired within a unit sampling time. This SNR value is determined not only by the magnetic field strength but also by many other NMR parameters, such as T_1, apparent transverse relaxation time (T_2^*) and RF coil quality factor (Q), which are all field dependent. All of these parameters should be measured and accounted for at different field strengths. However, most SNR comparison studies reported in the literature were conducted using the same NMR acquisition parameters at different field strengths, which did not accounts for the influence of these field-dependent parameters upon the SNR measurement at a given field strength. The conclusions draw from these studies would be subjective to the specific NMR parameters used in the SNR measurements. In this work, we have applied a comprehensive approach to quantitatively determine and compare the *in vivo* ^{31}P NMR sensitivity obtained in the human brain at 4 and 7 T with the same NMR methodology and similar experimental setup. The PCr resonance peak in the *in vivo* ^{31}P MRS was used for the quantification and comparisons.

3.1.2 Theory

Under optimal condition, which means that the pulse flip angle (α) satisfies the Ernst equation of $\cos(\alpha_{opt}) = \exp(-TR/T_1)$ [72], the SNR of NMR resonance peak in a

spectrum acquired with the single-pulse-acquisition pulse sequence in a given unit sampling time can be expressed as equation [3-1] [72, 73],

$$SNR\ (\text{per unit sampling time}) \quad \propto \quad C\gamma^{2.5} B_0^{\beta}\, Q^{1/2} \left(\frac{T_2^{*}}{T_1}\right)^{1/2} (1 - E_2^2)^{1/2}\, G(TR/T_1) \quad [3-1]$$

Where $$G(x) = \left[2\frac{1-e^{-x}}{x(1+e^{-x})}\right]^{1/2}$$

And $$E_2^2 = \exp(-2 \cdot at / T_2^{*}),$$

C is the concentration of the nuclear spin under observation and *at* is the NMR spectrum acquisition time. $x = TR/T_1$; C and γ should be the same at 4T and 7T for the same nuclear spin, and they can be treated as a constant. Since $T_2^{*} = 1/(\pi\Delta\nu_{1/2})$, where $\Delta\nu_{1/2}$ is the linewidth of the resonance peak of interst, Equation [3-1] can be rewritten as Equation [3-2]

$$SNR\ (\text{per unit sampling time}) \quad \propto \quad B_0^{\beta}\, Q^{1/2} \left(\frac{1}{T_1 \cdot \Delta\nu_{1/2}}\right)^{1/2} (1 - E_2^2)^{1/2}\, G(TR/T_1). \quad [3-2]$$

This equation accounts for most field-dependent parameters that have influences in the net SNR, such as T_2^{*} signal loss and partial saturation of NMR signal due to relatively short TR. To precisely quantify and understand the NMR sensitivity as a function of magnetic field strength, one needs to experimentally determine and quantify

all parameters used in Eq. [3-2]. Notice that the definition of SNR as used in this article was based on the description of Eq. [3-2].

We have conducted a comprehensive ^{31}P MRS study to compare the sensitivity and spectral resolution of PCr resonance peak in the human occipital lobe at 4 and 7 T. The results from this study answered the following questions: (a) How much SNR gain can be achieved in the human brain *in vivo* ^{31}P MRS at 7 T as compared with 4 T? (b) How do the measured NMR parameters contribute to the SNR gain at different field strengths?

3.1.3 Methods and Materials

Twelve healthy human adults (8 men and 4 women, 19-50 years old) were recruited for this study; six of them performed the SNR comparison study at 4T and 7T, and the other six performed the study of T_1 measurements at 4T. The experimental procedures were approved by the Institutional Review Board of the University of Minnesota, and written informed consent was obtained from all subjects prior to study.

The experiments were performed at 4T (Oxford 90 cm bore magnet) and 7T (Magnex Scientific 90 cm bore magnet) whole body MR scanners interfaced with the same Varian (Palo Alto, CA) console. Two passively decoupled dual-coil RF probes with the identical head holder and coil geometry were designed and constructed for both 4T and 7T experiments. Each RF probe includes (a) a linear and large butterfly ^{1}H surface coil for shimming and acquiring anatomical images using the T_1-weighted TurboFLASH imaging sequence, and (b) a 5-cm diameter single-loop ^{31}P surface coil, designed for

covering the human occipital lobe, for acquiring *in vivo* ^{31}P spectra. The noise figure of the receiver preamplifier of the spectrometer was 1.1 dB at 4T and 1.3 dB at 7T, resulting in a negligible defference in the preamplifier noise (~2%) for the ^{31}P measurements.

The same subjects were examined at both 4T and 7T with the similar experimental setup. The subject's head position relative to the RF probes was carefully controlled for ensure that the ^{31}P spectra acquired at the two fields were sampled from the same brain region of the subject. The RF power for achieving a nominal 90^{o} flip angle for *in vivo* ^{31}P MRS study was experimentally calibrated, and then the RF power was optimized and scaled down to give an Ernst flip angle according to the Ernst equation using the fixed repetition time (TR = 3 s) and the T_1 value of PCr at a given field strength. The single-pulse-acquisition sequence (α-acquisition, using a 200-μs hard pulse) was applied to acquire *in vivo* ^{31}P spectra from the human occipital lobe. Other spectral parameters were: spectral width = 5000 Hz; spectrum acquisition time (*at*) = 0.1 s.

T_1 was measured at near fully relaxed condition with TR = 16 s ($\approx 4T_1$). Inversion recovery pulse sequence (180^0-TI-α-acquisition, where TI is the inversion recovery time) was used to determine the T_1 values of PCr at 4T [35]. The magnetization inversion of the PCr and other resonance peaks was achieved adiabatically in the entire sensitive volume of the ^{31}P RF surface coil by using a B_1-insensitive 16-ms hyperbolic secant RF pulse [74]. A total of eight measurements with different TI values ranging from 12.5 ms to 32 s were performed to calculate the PCr T_1 values. No additional spatial localization was applied, except that achieved by the surface coil itself to ensure that the major ^{31}P

signal detected by the coil is confined in the human occipital lobe [35]. A simulation program developed by Varian was utilized to fit and calculate T_1 values based on the following equation:

$$M(TI) = \{M(0) - M_0\}\exp(-TI/T_1) + M_0 \qquad [3-3]$$

Where M(TI) is the longitudinal magnetization at time TI, and M(0) and M_0 are the longitudinal magnetizations at TI = 0 and at equilibrium, respectively.

An optimal line broadening that is equal to the line width of the PCr resonance peak (9.0 Hz at 4 T and 13.4 Hz at 7 T) was applied to spectral data processing for SNR enhancement and for improving quantification accuracy. The PCr peak height was used for quantification in the T_1 regression according to Eq. [3-3]. The SNR values were calculated by obtaining the ratio of the PCr peak height to the peak-to-peak spectral noise and multiplying it by 2.5.

3.1.4 Results

Figure 3-1 shows the 2D ^{31}P chemical shift images (CSIs) of a cylindrical bottle phantom (7 cm diameter) filled with high concentration Pi at 4T (Fig. 3-1a) and 7T (Fig. 3-1b), respectively. The CSIs were acquired by using the similar RF surface coils and a nominal 90^o flip angle under fully relaxed condition at the two fields. The Fourier-series window (FSW) technique was applied to obtain the 2D CSIs [75]. The 1D profiles of Pi signal along two orthogonal dimensions are very similar between 4T and 7T, which indicates that the sample regions and NMR signal distributions detected by the surface

coils at the two fields are equivalent. Thus, it was valid to conduct the SNR comparison study between 4T and 7T using the experimental protocol.

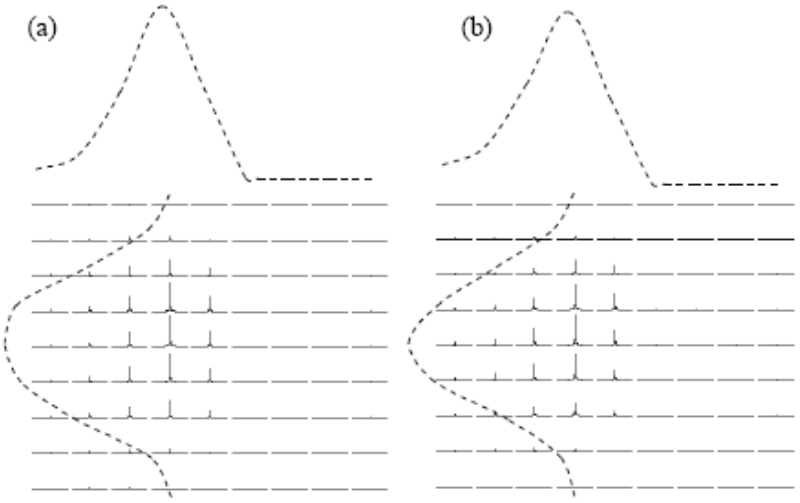

Figure 3-1 2D ^{31}P CSI in the transversal orientation and its 1D profiles in two dimensions acquired at (a) 4T and (b) 7T, respectively, by using a cylindrical bottle phantom filled with high concentration inorganic phosphate. The field of view was 10cm ×10cm, and the phase encoding steps were nine in each dimension.

Figure 3-2 demonstrates the T_1 measurement of PCr resonance peak in the human visual cortex at 4T. The T_1 recovery was fitted by a single exponential curve (see Fig. 3-2b) according to Equation [3-3]. The averaged PCr T_1 value in the human visual cortex at 4T was 4.27±0.27 s (n=6). In contrast, the PCr T_1 value at 7T measured 3.37±0.29 s [35].

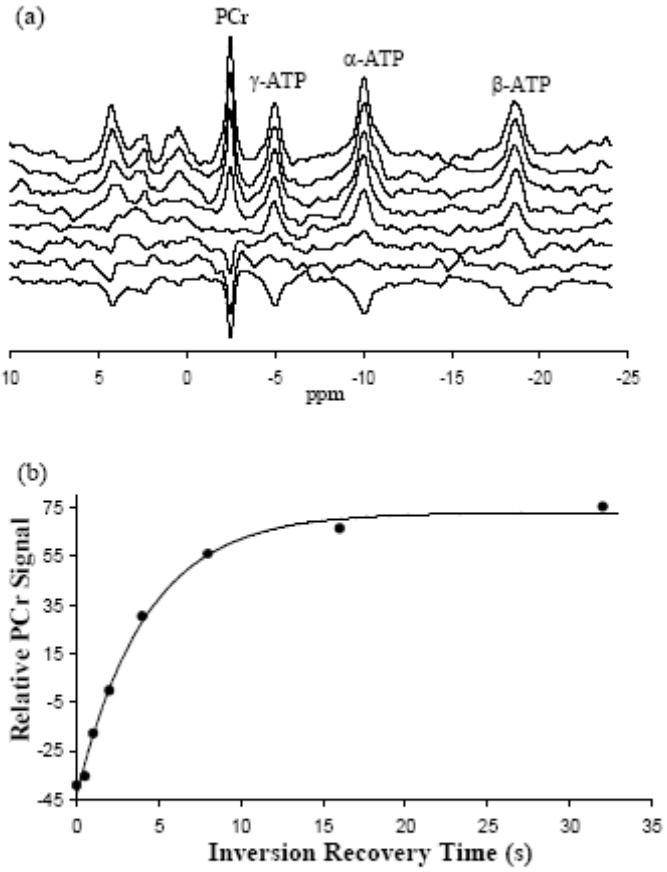

Figure 3-2 ^{31}P T_1 relaxation time measurement for PCr peak in the human visual cortex at 4 T. (a) Inversion recovered *in vivo* ^{31}P spectra acquired from one representative subject. Eight TI values were measured. (b) Exponential fitting of the PCr signal as a function of TI for calculating the PCr T_1 value (= 4.20 s). The averaged T_1 value is 4.27±0.27 s (n=6).

Figure 3-3a shows a sagittal image covering the human primary visual cortex and the position of the ^{31}P surface coil. Figures 3-3b and 3-3c illustrate *in vivo* ^{31}P spectra acquired with 128 signal averages (TR = 3 s) at 4T and 7T, respectively, from the same subject as used in Fig. 3-3a. They show significant improvements of the *in vivo* ^{31}P spectrum in both sensitivity and spectral resolution at 7T.

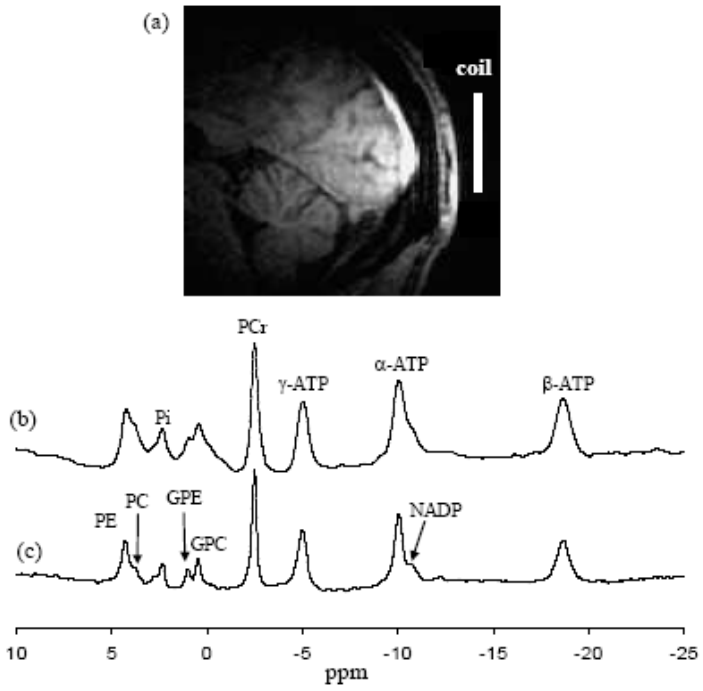

Figure 3-3 (a) Anatomical human brain MRI (in the sagittal orientation). *In vivo* ^{31}P spectra acquired from the human primary visual cortex at (b) 4T and (c) 7T, respectively, using the same experimental setup and NMR acquisition parameters (TR = 3 s and 128 signal averages). PE: phosphoethanolamine; PC: phosphocholine; Pi: inorganic

phosphate; GPE: glycerophosphoethanolamine; GPC: glycerophosphocholine; PCr: phosphocreatine; ATP: adenosine triphosphate; NAD: nicotinamide adenine dinucleotides.

Table 3-1 summarizes the results of the PCr T_1 relaxation times, linewidths ($\Delta\nu_{1/2}$) and SNRs, as well as RF coil quality factors measured at 4T and 7T. Importantly, there is a 56% increase in SNR of PCr resonance peak at 7T as compared to 4T.

B_0	T_1(s) (n=6)	$\Delta\gamma_{1/2}$(Hz) (n=6)	Q	SNR (n=6)
7T	3.37±0.29*	13.4±0.8*	79.5	81.4±7.2*
4T	4.27±0.27	9.0±0.4	130	52.2±8.4
Ratio	0.79	1.49	0.61	1.56

* The measured parameter at 7T is significantly different from 4T ($P<0.05$).

Table 3-1 Summary of relaxation times, linewidths and SNRs of PCr, and RF coil quality factors at 4T and 7T

Figure 3-4 illustrates the relationship between the PCr T_1 value and field strength. Data used in this figure came from both the literature and our results measured in this study and a previous study [35].

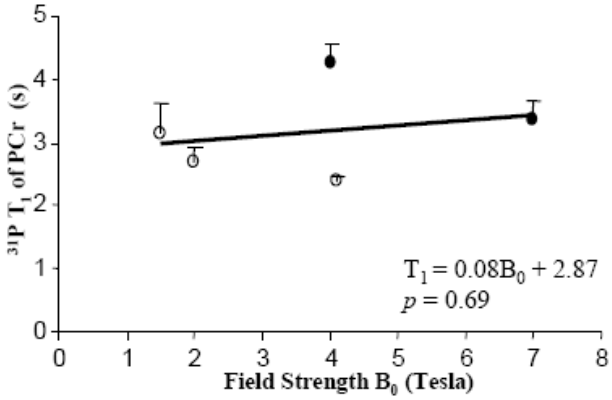

Figure 3-4 Field dependence of PCr T_1 in the human brain. The data were based on the literature (circle), which were summarized in the reference of [35] and the measurements from our laboratory (dot).

3.1.5 Discusion and Conclusions

The $G(TR/T_1)$ term in Eq. [3-2] is close to unity when $TR<T_1$. In this study, TR was 3 s at both 4 and 7 T and T_1 was 4.27 s at 4 T and 3.37 s at 7 T; thus, the $G(TR/T_1)$ term was equal to 0.98 at 4 T and 0.97 at 7 T accordingly (see Table 3-2). Under this condition, the function $G(TR/T_1)$ was very similar and close to 1 at the two fields. In addition, the acquisition time parameter (at) was 0.1 s at both fields, T_2^* was 35 ms at 4 T and 24 ms at 7 T, and the function $(1-E_2^2)^{1/2}$ in Eq. [3-2] was approximately equal to 1.00 at both 4 and 7 T (see Table 3-3). With these facts, we can simplify Eq. [3-2], which further leads to the following approximate equation:

$$SNR\,(\text{per unit sampling time}) \quad \propto \quad B_0^{\beta}\, Q^{1/2} \left(\frac{1}{T_1 \cdot \Delta \nu_{1/2}} \right)^{1/2} \qquad [3-4]$$

Inserting all measured parameters as summarized in Table 3-1 into Equation [3-4] at both 4T and 7T, we deduced β to be 1.4, which is in excellent agreement with the theoretically predicted β value of 1.5 as described in the literature [72, 73, 76].

B_0	TR (s)	T_1 (s)	TR/T_1	$G(TR/T_1)$
7T	3.0	3.37	0.89	0.97
4T	3.0	4.27	0.70	0.98

Table 3-2 Values of function $G(T/T_1)$ at 4T and 7T

B_0	*at* (s)	$\Delta\gamma_{1/2}$ (Hz)	T_2* (ms)	$(1-E_2^2)^{1/2}$
7T	0.1	13.4	24	1.00
4T	0.1	9.0	35	1.00

Table 3-3 Values of function $(1-E_2^2)^{1/2}$ at 4T and 7T

Comparing the T_1 data obtained in this study with those previously reported in the literature (see the summarized results as cited in the reference of [35]), we found that the T_1 relaxation time of PCr in the human brain does not change significantly between 1.5 T to 7T ($P>0.05$; also see Figure 3-4) based on the entire pool of T_1 data. However, the results of PCr T_1 measurements in the human brain obtained in our laboratory reveal that the PCr T_1 significantly decreases at 7T as compared with 4T (dropping 21%, see Table 3-1). This observation indicates that the field dependence of PCr T_1 is presumably determined by two competing relaxation mechanisms, that is, chemical shift anisotropy (CSA) and dipolar interaction, which simultaneously influence the ^{31}P relaxation times [77, 78]. In the case with dominant CSA contribution, the T_1 value should decrease with increasing field strength following the relation: $1/(T_1) \propto B_0^2$, while in the case of dominant dipolar interaction contribution, the T_1 value usually increases with increasing field strength (e.g., *in vivo* ^1H MRI/MRS). The opposite trends between these two relaxation mechanisms could lead to an approximately field independence of PCr T_1 and/or a decrease in PCr T_1 at higher field as observed in our study. This observation was supported by the rat study showing that the T1 values of brain phosphorus metabolites decreased with increasing field strength [77]. The decrease in the T_1 values at higher field strength offers an advantage for *in vivo* ^{31}P MRS as a shorter TR can be employed for allowing more signal averaging within the same sampling time and, ultimately, to increase SNR. According to Equations [3-4] and [3-5] (see the third term on the right side of Equation [3-5]), the decrease in the PCr T_1 at 7T alone could contribute a 13% SNR gain at 7T as compared to 4T.

$$\frac{SNR_{(7T)}}{SNR_{(4T)}} = (\frac{7}{4})^{1.4} \sqrt{\frac{Q_{(7T)}}{Q_{(4T)}}} \cdot \sqrt{\frac{T_{1(4T)}}{T_{1(7T)}}} \cdot \sqrt{\frac{\Delta\nu_{1/2(4T)}}{\Delta\nu_{1/2(7T)}}} \quad [3-5]$$

1.56 2.16 0.78 1.13 0.82

The average linewidth of PCr (without line-broadening) observed in this study was 13.4±0.8 Hz at 7T and 9±0.4 Hz at 4T. As illustrated by the forth term on the right side of Equation [3-5], this linewidth broadening alone can lead to an 18% loss in SNR at 7T compared to 4T. However, the ratio of these two linewidths is 1.49, which is smaller than the ratio (=1.75) of field strengths between 4T and 7T. This observation indicates that the linewidth broadening of PCr resonance peak with increased field strength was not linearly correlated to the field strength and it is smaller than the magnitude of field strength increase. Moreover, the chemical shift dispersion (i.e., in Hz) of *in vivo* ^{31}P MRS increases linearly with field strength. The combination of these two facts (i.e., large increase in chemical shift dispersion and relatively small increase in linewidth broadening) improves the ^{31}P spectral resolution at 7T as demonstrated in Fig. 3-3. This improvement makes it possible to resolve many adjacent phosphate metabolites (e.g., α-ATP versus NADP) and phospholipid compounds involved in phospholipid metabolism (e.g., Glycerophosphocholine vs. glycerophosphoethanolamine and phosphocholine vs. phosphoethanolamine) as shown in Fig. 3-3. Therfore, the advantages of 7T should improve accuracy and reliability for quantifying the phosphorus compounds.

The field dependence of NMR detection sensitivity is significantly distinct among different nuclei. It has been shown that the average SNR increases linearly from 4 to 7 T for the proton imaging of human brain [79]. In contrast, as demonstrated in the rat brain [80], there is an approximate quadruple increase in SNR for *in vivo* ^{17}O MRS from 4.7 to 9.4 T without significant changes of ^{17}O T_1 and T_2 relaxation times of water. For the *in vivo* ^{31}P MRS of human brain, the SNR acquired within a unit sampling time gains 56% at 7 T as compared with 4 T, based on our measurements, when the field strength increases 75% from 4 to 7 T. Besides a shortened T_1 at 7 T being a factor in achieving a significant SNR gain at 7 T, a greater factor that helped achieve such a gain is an increased field strength. The increase in B_0 from 4 to 7 T should provide 116% gain in SNR according to the first term on the right side of Eq. [3-5]. The interplay among the SNR gains contributed by the increased B_0 and shortened T_1 and the SNR losses caused by shortened T_2^* and degraded Q, which alone reduced 22% SNR according the second term on the right side of Eq. [3-5], leads to a net SNR gain of 56% at 7 T as compared with 4 T. If one assumes that the same Q value of the ^{31}P surface coil could be achieved at both 4 and 7 T (i.e., $Q_{(7\ T)}/Q_{(4T)}=1$ in Eq. [3-5]), then the predicted net SNR gain at 7 T will increase from 56% to 99.5% according to Eqs. [3-4] and [3-5]. In fact, it has been demonstrated that the RF coil Q usually could increase when B_0 increases within a wide range of resonant frequency up to 200 MHz [73]. Therefore, it is plausible that the SNR of *in vivo* ^{31}P MRS can further increase with a better than linear relation as a function of B_0.

In conclusion, we have established a rigorous approach to quantitatively determine and compare the NMR detection sensitivity at different field strengths. The β power term as measured by the approach was consistent with the theoretically predicted β value. Eqs. [3-4] and [3-5] should be useful in estimating the field dependence of NMR detection sensitivity beyond 4 and 7 T, and they are also valid for other nuclei. The results from this study clearly indicate the advantages and benefits of *in vivo* ^{31}P MRS at 7 T in terms of improvements in both detection sensitivity and spectral resolution. Such improvements should (a) make high-field *in vivo* ^{31}P MRS capable of precisely determining HEP metabolites, other phosphate compounds actively involved in the phospholipid metabolism and chemical exchange kinetic rates noninvasively (e.g., the measurement of the ATP synthesis rate in the human occipital lobe [65]) and (b) improve the reliability and applicability of *in vivo* ^{31}P MRS in studying HEP metabolism and biogenetics in the human brain, as well as (potentially) in other organs (e.g., heart and skeletal muscle), at both normal physiological and diseased states noninvasively.

3.1.6 Acknowledgements

The authors thank Drs. Peter Andersen, Hao Lei, Nanyin Zhang and Kamil Ugurbil for their insightful discussion, support and technical assistance.

3.2 Signal-to-Noise Ratio under Optimized Condition

In this paper, we used the original SNR equation to derive the optimized relationship between SNR, as well as SAR, and flip angle and Tr/T_1. The results show that 1) when flip angle is less than 60^0 ($Tr/T_1 < 0.607$), both Ernst angle equation and optimized relationship give similar SNRs, and from 10^0 to 60^0, the SNR decreased less than 5%; 2) when flip angle is between 60^0 and 90^0 ($Tr/T_1 > 0.607$), SNR simulated from the optimized relationship is bigger than that from Ernst angle equation; 3) the minimum SAR can be achieved with about 60^0 flip angle.

3.2.1 Introduction

It has been well known that people can use small flip angle and short Tr, which follow the Ernst angle equation [3-6], to achieve high Signal-to-Noise Ratio per unit time (SNR) in *in vivo* MR study. In our work, we used the original SNR Equation [3-7] to derive the optimized relationship between SNR, as well as SAR, and flip angle α and Tr/T_1. In Equation [3-7], G should be maximized in order to maximize the SNR. With the optimized relationship, we did phantom experiments at 9.4 T.

$$\cos(\alpha) = \exp(-T_r / T_1) \qquad [3-6]$$

$$\frac{S}{N} \propto \quad G(Tr / T_1, \alpha)$$

$$G = \frac{[1-\exp(-Tr / T_1)]^2 \sin^2 \alpha}{[1-\cos\alpha \exp(-Tr / T_1)]^2 (Tr / T_1)} \qquad [3-7]$$

3.2.2 Methods

The simulation was done in Matlab. The phantom experiments were performed at a 9.4 Tesla/31-cm bore magnet (Magnex Scientific, Abingdon, U.K.) with Varian INOVA console (Palo Alto, CA). Co-axile line saddle-coil configuration was designed with a 3.5-cm diameter each loop. The phantom was a 0.8-cm diameter glass ball, which was set in the middle of the coil. In order to test the uniform of B_1 field in the phantom, we did experiments with array pulse width, and then, used different pulse width to achieve different flip angle. Finally, we did the experiments with array pulse width, Tr, and nt simultaneously. In these experiments, pulse width, Tr, and nt follow the optimized relationship from the simulated results.

3.2.3 Results

Figure 3-5 shows a set of spectrum with different pulse width to test the uniform of B_1 field. Figure 3-6 shows the simulated results, SNR verses optimized flip angle (red line) and Ernst angle (green line), and SAR verses optimized flip angle (blue line). Figure 3-7 shows the experimental data with their standard deviations and the theoretical prediction curve.

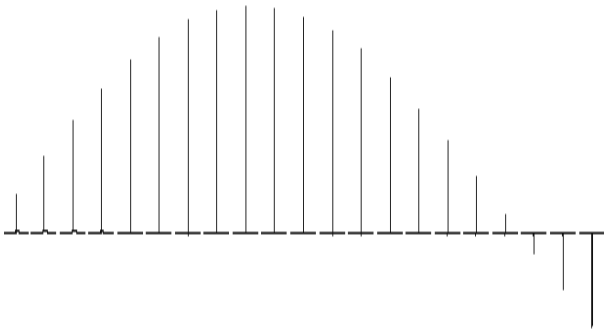

Figure 3-5 A set of spectrum with different pulse width to test the uniform of B_1 field.

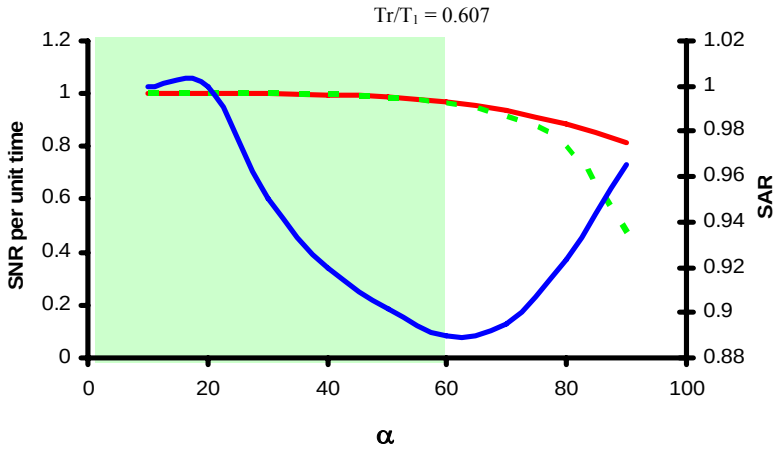

Figure 3-6 Simulation results. SNR verses optimized flip angle (red line) and Ernst angle (green line), and SAR verses optimized flip angle (blue line).

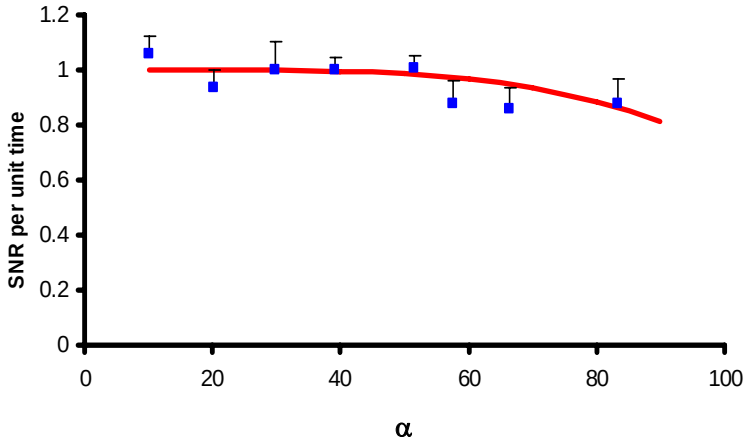

Figure 3-7 Experimental data with their standard deviations and the theoretical prediction curve.

3.2.4 Discussion and Conclusion

Figure 3-5 shows the B_1 field is uniform in the phantom, which justifies that we can use pulse width to control the flip angle. In Equation [3-7], the simulation result is Gmax=1/2, which occurs as α and $Tr/T_1 \rightarrow 0$. This limit in fact dose exist in the strict mathematical sense. However we must remember that Tr cannot really be reduced beyond a value in the range of T_2^* if useful spectral information is to be obtained. Fortunately the maximum in G is very broad: representative values are given in Table 3-4. Note that even for $Tr = T_1$ the sensitivity has been reduced by only ~ 10%. Figure 3-6 shows that 1) in the case that flip angle $\alpha < 60^0$ ($Tr/T1 < 0.607$), both Ernst angle and optimized relationship give the same results, and pushing too small flip angel only can increase SNR with a small degree of less than 5%; 2) in the case that flip angle $\alpha > 60^0$ ($Tr/T_1 > 0.607$), we should use the optimized relationship to achieve higher SNR; 3) in the case that SAR is crucial, Figure 3-6 provides the information how to optimizing the SAR, as well as SNR. Figure 3-7 shows that the experimental results are consistent with the theoretical prediction. We will do *in vivo* study in the near future to confirm the theoretical prediction further.

angle	Tr/T_1	G
10	0.015	0.4998
20	0.06	0.4997
30	0.142	0.4991
40	0.261	0.4971
50	0.416	0.4925
60	0.607	0.4833
70	0.821	0.4674
80	1.04	0.4425
90	1.259	0.4073

Table 3-4 Optimum values of flip angle and reduced repetition time for the FID Experiment.

3.2.5 Acknowledgements

This work was partially supported by NIH grants NS38070, NS39043, NS41262, EB00329, EB00513, P41 RR08079, WM Keck Foundation, and MIND Institute.

4. WHOLE BRAIN 3D ^{31}P CSI

4.1 Introduction

In vivo ^{31}P MRS can be used to assess bioenergetics of human brain non-invasively, and it is useful for studying brain function and neurological diseases. Large gains in both NMR sensitivity and spectral resolution at 7 Tesla significantly improve the quality of *in vivo* ^{31}P MRS in the human brain for providing rich information including phosphocreatine (PCr), adenosine triphosphate (ATP) and inorganic phosphate (Pi), intracellular pH, and forward rate constant of the creatine kinase (CK) reaction, as well as the ATP synthesis rate [35, 65]. It is well known that the cerebral metabolic rates (e.g., glucose and oxygen utilizations) and blood flow are significantly higher in the gray matter than that in the white matter. It has been demonstrated that the CK activity in the human gray matter is also higher than white matter indicating a high phosphate metabolism in the gray matter in the human brain [81]. In this study, we systematically analyzed the *in vivo* 3D ^{31}P chemical shift imaging (CSI) data acquired from the entire human brain at 7 Tesla for quantifying ATP, PCr and other phosphate metabolites, pH and magnesium (Mg^{2+}) between the gray and white matters. Significant differences in most measured parameters were found in this study.

4.2 Spectroscopic Imaging Using Fourier Series Window (FSW)

CSI already is an established tool for studying *in vivo* biochemistry and metabolic pathways in fundamental biomedical research. CSI is also emerging as a valuable diagnostic approach. NMR spectroscopy has been successfully applied to finding the seizure foci in temporal lobe epilepsy, to studying brain metabolic alterations in patients

with AIDS, or to detecting at a very early stage tumor response to chemotherapy. Preliminary studies have also shown that CSI might be valuable for investigating non-invasively abnormal cardiac energy metabolism in various pathologies.

Since biological subjects are heterogeneous, it is necessary to restrict the spectroscopic signals to a well-defined volume or region of interest in the intact body. Toward accomplishing this goal, various localization techniques have been developed. Among various techniques developed for localized *in vivo* spectroscopy, CSI or spectroscopic imaging is an attractive technique, since it is capable of producing images reflecting the spatial distribution of various chemicals of interest. There have been many recent efforts to use CSI to produce metabolite images. A standard CSI experiment required the resolution of spatial and spectroscopic information; therefore, unlike a conventional imaging sequence, spatial encoding in CSI is achieved by phase encoding only. The acquired data consist of an array of points spanning a discrete hybrid space of spatial frequency and time. A multidimensional inverse Fourier transformation of the raw data yields the CSI which gives the spatial distribution of the spectra. Because of the necessity of using phase encoding, CSI in more than one spatial dimension can be very time consuming. Furthermore, since the metabolite signals to be detected are extremely small, it is impractical and even detrimental to fully cover high K space in CSI experiments. In practice, only a small portion in low K space could be sampled. For example, a typical two-dimensional CSI study can have a matrix of 16×16 or 32×32. This limited sampling, of course, results in poor spatial resolution of CSI. In particular, the

CSI obtained by Fourier transforming the limited number of phase-encoded data is plagued by the infamous ringing artifact which causes long-range signal contamination.

Spatial localization with the spectroscopic imaging technique is normally implemented with the Fourier-transform approach, yielding rectangular voxels. An alternate solution is to weight the k-space acquisition with the desired filter using the FSW method [75, 82, 83]. The filter is based on the Fourier coefficients of a predetermined voxel shape following a practical and optimum termination of the series. A single voxel is generated by summation with respect to the phase-encode domain and this voxel can then be shifted arbitrarily in the phase-encode directions.

The implicit assumption here is that the noisy high-K-space data will allow us to define the high-signal areas better so that the signal contamination from them can be reduced while the metabolite signals are mostly captured by the less noisy low-K-space data. Thus, the fundamental principle is to ignore the high-spatial-frequency components of the metabolites which cannot be detected with adequate SNR in a reasonable time. Obviously, a straightforward FT of the data obtained with this scheme would generate noisy chemical-shift images. A new reconstruction technique is also devised to generate smooth images.

Specifically, voxel described by the window function of the spatial coordinate in one dimension is defined with a specific phase angle, θ_q,

$$W(\theta(\mathrm{r}) - \theta_q) = \sum_{n=0}^{N-1} w_n^q \exp\{in\theta(\mathrm{r})\} \qquad [4\text{-}1]$$

The spectrum for this voxel constructed by the weighted spectrum using the Fourier window coefficient w_n in Eq. [4-1] can be described by

$$S_w^q(\theta(\mathrm{r}) - \theta_q) = \sum_{n=0}^{N-1} s_n(t) w_n^q \exp\{in\theta(\mathrm{r})\} \qquad [4\text{-}2]$$

where s_n(t) is the NMR signal in time domain. Base on the Fourier shift theorem, localized spectra from other locations can be generated by voxel shifting by adding the term of phase shifting (ψ). The shifted window function can be expressed by

$$W(\theta(\mathrm{r}) - \theta_q - \psi) = \sum_{n=0}^{N-1} w_n^q \exp\{in(\theta(\mathrm{r}) - \psi)\} \qquad [4\text{-}3]$$

And the spectrum of new location is generated as

$$S_w^q(\theta(\mathrm{r}) - \theta_q - \psi) = \sum_{n=0}^{N-1} s_n(t) w_n^q \exp\{in(\theta(\mathrm{r}) - \psi)\} \qquad [4\text{-}4]$$

The early development studies at our research center had shown excellent spatial localization with the circular FSW voxel approach with negligible out-of-voxel contamination [75]. Generally, the data acquisitions in the FSW method are heavily weighted in the central k-space lines with high NMR signals according to the Fourier coefficients. This together with the lack of high k-space points in the circular voxel shape (which are required for the rectangular voxels) provides significant gains in sensitivity per unit acquisition time at the expense of slightly broader voxel size defined by full width at half-maximum compared to the conventional Fourier-transform approach [84]. We have extensively implemented and validated 1D, 2D and 3D FSW methods

(circular, cylindrical and spherical voxel shapes) for acquiring ^{31}P MRS images in the human brains. Our results reveal that the FSW method provides a useful tool for ^{31}P MRS imaging.

4.3 Methods

3D ^{31}P CSI data were acquired on a 90-cm bore 7 T Magnex magnet with a Varian INOVA console. A ^{1}H/^{31}P double-tuned TEM volume coil using quadrature driving was designed and constructed for MR applications at 7 Tesla. Three dimensional ^{31}P CSI was acquired using a Fourier series window imaging technique [23] with spectral bandwidth of 5000 Hz, 45^{o} Ernst angle for optimal spin excitation, FOV of 20×20×22 cm^{3}, matrix size of 15×15×13, TR = 0.5 s, cylindrical voxel shape, 10.9 ml voxel size and the total acquisition time of 51 minutes. Two grouped ^{31}P spectra were used for quantification and they were the summation of 8-10 ^{31}P spectra from the multiple voxels either dominated by the gray matter or white matter brain tissue. Spectral processing was carried out using the software package MRUI, and the AMARES method of MRUI was used for quantification. Due to the closed chemical shifts between phosphoethanolamine (PE) and phosphocholine (PC), these two resonance peaks were treated as a single resonance peak and was assigned to PME. However, both glycerophosphoethanolamine (GPE) and glycerophosphocholine (GPC) were treated as a single resonance peak. Intracellular pH was calculated from the chemical shift difference between the PCr and the Pi resonances. The magnesium concentration was calculated from the chemical shift difference between the α-ATP and β-ATP resonance peaks and other constants [85].

Paired t-test was used for statistical analysis and a $p<0.05$ was considered statistically significant. The results were presented by mean ± std.

4.4 Results and Discussion

Figure 4-1 shows the paired results of pH values measured in the gray and white matter, respectively, from seven subjects. Each subject has a relatively low pH (or more acidic) in the white matter compared to that in the gray matter, though the difference was small. The pH value was 6.980 ± 0.013 and 7.014 ± 0.013 in the white and gray matter, respectively, with a pH difference of 0.034 ± 0.019. The pH difference is statistically significant (P = 0.003). Figure 4-2 summarizes the comparison results of the PCr and γ-ATP concentrations ratios between the gray and white matters. It indicates that there is no statistical difference in the ATP concentrations between the gray and white matter (P = 0.14). In contrast, the PCr concentration in the gray matter is statistically higher than that in the white matter ($P = 3.4\times10^{-5}$). This result is consistent with the fact of high bioenergetics in the gray matter. Table 4-1 summarizes the results of PCr and ATP concentration ratio and other phosphate metabolite as well as Mg^{2+} concentration ratio. Based on this preliminary study, the concentrations of PME, GPE and Mg^{2+} don't have statistical differences between the gray and white matters. Nevertheless, the GPC concentration in the white matter is significantly higher (31%) than that in the gray matter. This difference may be linked to the membrane phospholipid metabolism between two different brain tissue compartments. One potential impact of GPC is on the schizophrenia patient, which shows a decreased GPC content in the prefrontal region.

$$pH = 6.77 + \log[(\Delta Pi - 3.29) / (5.68 - \Delta Pi)]$$

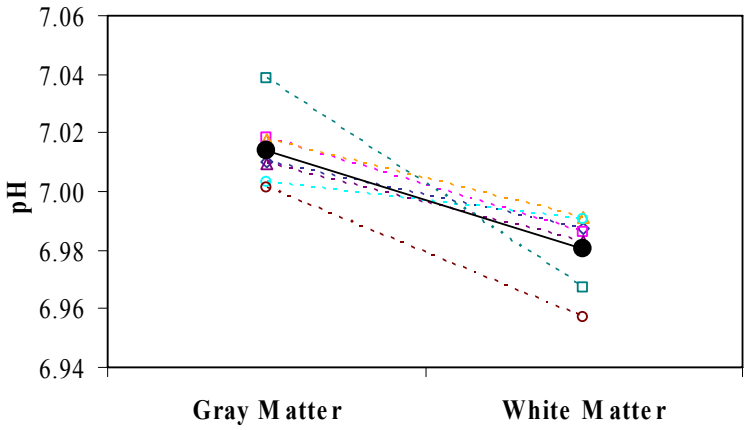

$$pH_{GM} > pH_{WM} \quad with\ P \leq 0.0034\ (n=7)$$

Figure 4-1 pH values in gray and white matter dominated voxels in human brain obtained form 7 subjects at 7T.

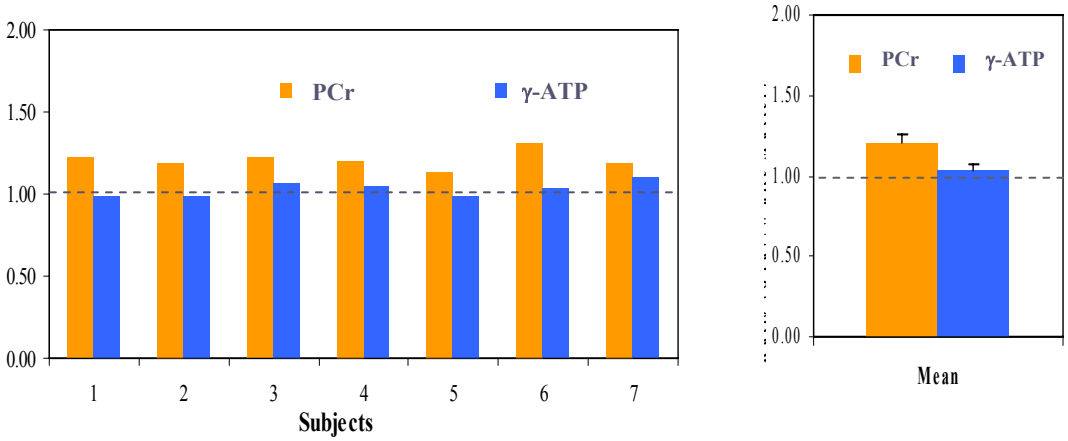

$$PCr_{GM} > PCr_{WM} \quad with\ P \leq 3.4\times10^{-5}$$

$$\gamma\text{-}ATP_{GM} \approx \gamma\text{-}ATP_{WM} \quad with\ P \approx 0.14$$

Figure 4-2 PCr and ATP metabolites ratio in gray and white matter dominated voxels in human brain obtained from 7 subjects at 7T.

	Mg^{2+}	GPC	PME	GPE	PCr	ATP
Ratio(GM/WM)	1.19±0.33	0.69±0.18	1.02±0.42	1.03±0.34	1.21±0.05	1.03±0.05
p_value	0.15	0.001	0.86	0.81	0.00034	0.14

Table 4-1 Summary of phosphate metabolites and Mg^{2+} concentration ratio in gray and white matter dominated voxels in human brain.

The differences measured in this study present low-limit values because of the significant contaminations of the white matter tissue in the grouped gray matter compartment used in our analysis. It is expected that the use of more precise tissue segmentations between the gray and white matters based on T_1-weighted images should increase the differences.

4.5 Conclusions

Excellent ^{31}P NMR sensitivity and improved spectral resolution achieved at 7 Tesla are capable of determining small differences of the measurable parameters between the gray matter and white matter reliably. This study suggests that ultra-high field strength is significantly advantageous for performing *in vivo* ^{31}P spectroscopy on human brain with better quantification, thus, it provides a great opportunity for noninvasive study of phosphate bioenergetics related to brain function and neuropathology.

4.6 Acknowledgements

NIH grants NS38070, NS39043, NS41262, EB00329, EB00513 and P41 RR08079, the W.M. Keck Foundation, and the MIND institute.

Presented by Xiaohong Zhu in ISMRM 2004.

5. KINETIC NETWORK OF ATP METABOLISM IN HUMAN BRAIN (I)

ATP metabolism is controlled mainly by ATP synthase (ATPase) and creatine kinase (CK) reactions that regulate cerebral ATP production, transportation, and utilization. These coupled reactions constitute a chemical exchange metabolic network of PCr↔ATP↔Pi characterized by two forward and two reverse reaction fluxes, which can be studied noninvasively by *in vivo* ^{31}P MRS combined with magnetization transfer (MT). However, it is still debated whether current MT approaches can precisely determine all of these fluxes. We developed and tested a modified *in vivo* ^{31}P MT approach based on a multiple single-site saturation (MSS) technique to study the entire PCr↔ATP↔Pi network in human occipital lobe at 7T. Our results reveal that 1) the MSS MT approach can explicitly determine all four reaction fluxes with a minimal number of ^{31}P spectra; 2) the three-spin exchange model accurately determines reverse reaction fluxes, resulting in equal forward and reverse fluxes for both CK and ATPase reactions; and 3) the ATP synthesis rate (8.8 ± 1.9 μmol/g/min, N = 11) measured in the human brain reflects cerebral oxidative phosphorylation. The MSS MT approach should provide an important modality for noninvasively studying the essential roles of ATP metabolism in brain bioenergetics, function, and diseases.

5.1 Introduction

The primary functions of brain cells are excitation and conduction, which are reflected by constant electrophysiological activity in the brain. The cerebral bioenergetics that support sustained electrophysiological activity are ultimately driven by a variety of biochemical processes that maintain the normal function and structural integrity of the

brain [86]. Of these processes, the most fundamental for supporting various cellular activities is adenosine triphosphate (ATP) metabolism in living cells [87]. The majority of ATP is formed from adenosine diphosphate (ADP) and inorganic phosphate (Pi) in the mitochondria through oxidative phosphorylation catalyzed by the ATP synthase (ATPase) enzyme, as illustrated by Fig. 5-1a [88, 89]. The highly demanding biochemical processes involving ATP production and utilization in the brain cause rapid chemical cycling among ATP, ADP, and Pi (see Fig. 5-1a). These processes are also accompanied by another important chemical reaction involving phosphocreatine (PCr) and creatine kinase (CK). PCr acts as an ATP reservoir and carrier, and transfers energy from the mitochondria to sites of ATP utilization in the cytosol through reversible CK reactions, ultimately maintaining a stable cellular ATP level [89, 90]. These two chemical exchange reactions (i.e., PCr↔ATP and Pi↔ATP) play central roles in regulating ATP metabolism and maintaining normal ATP functionality, both of which are crucial for cerebral bioenergetics and brain function in the healthy brain as well as in neurodegenerative diseases. Moreover, the ATPase and CK reactions are tightly coupled together, leading to a complex three-^{31}P-spin chemical exchange kinetic network (i.e., PCr↔ATP↔Pi) as depicted in Fig. 5-1b. Thus, it is essential to develop a noninvasive, reliable technique that is capable of assessing the entire kinetic network of PCr↔ATP↔Pi and associated ATP metabolic fluxes in situ, particularly in the human brain.

Measuring all kinetic parameters involved in the PCr↔ATP↔Pi network requires extensive information, including three steady-state phosphate metabolite concentrations (i.e., [ATP], [PCr], and [Pi]) and four pseudo-firstorder chemical reaction rate constants

(forward and reverse rate constants for the CK reaction and the ATPase reaction, as defined in Fig. 5-1b). The products of the rate constants and their related phosphate concentrations can provide four ATP metabolic fluxes along both forward and reverse reaction directions in the PCr↔ATP↔Pi kinetic network (see Fig. 5-1b). The sole approach that is capable of noninvasively studying these chemical exchange kinetics in situ is *in vivo* ^{31}P MRS combined with the magnetization transfer (MT) method [63]. Several *in vivo* ^{31}P MT methods have been developed, such as conventional two spin magnetization saturation transfer (CST), inversion recovery transfer (IT), and two-dimensional chemical exchange spectroscopy (2D-EXSY) [40, 64, 91, 92]. These methods have been applied to physiological studies of ATP metabolism in a variety of organs, including the heart and brain [35, 40, 65, 91, 93-100]. Of these methods, the CST method is most commonly used in biomedical research, perhaps because of its methodological simplicity and high efficiency. This method is particularly useful for measuring forward rate constants and fluxes in the chemical exchange system of PCr↔ATP↔Pi when a frequency-selective radiofrequency (RF) saturation pulse train is applied to fully saturate the γ-ATP spin. In this case the three-spin (i.e., PCr↔ATP↔Pi) chemical exchange system can be treated as two independent two-spin chemical exchange systems (i.e., PCr↔ATP and ATP↔Pi), and consequently the forward rate constants and fluxes for both the CK and ATPase reactions can be determined explicitly. These forward metabolic fluxes reflect the ATP synthesis (or production) rates catalyzed by ATPase and CK. However, measurements of the reverse CK flux (F_r^{CK}: ATP↔PCr) using CST (i.e., by saturating PCr) resulted in an inequality between the forward and

reverse CK fluxes [101-103], which contradicts the fact that the CK fluxes in and out of the PCr pool must be equal if the CK reaction is in chemical equilibrium. To date, there are several ways to interpret these contradictory results. Two possible explanations are that 1) a small portion of intracellular PCr or ATP metabolites (or both) may be NMR-invisible or do not fully participate in the CK reaction, and 2) they may locate in different cellular compartments with distinct kinetics [104, 105]. However, these possibilities have not been rigorously demonstrated and are difficult to definitively verify in situ. Another alternative interpretation is that ATP could be involved in other chemical exchange reactions besides the CK reaction. One obvious example is the ATP hydrolysis reaction [106]. Consequently, neglecting ATP hydrolysis may lead to an error in estimating the reverse CK flux. Therefore, it is necessary to consider PCr↔ATP↔Pi as a three-spin chemical exchange system in order to accurately determine all kinetic parameters, in particularly the reverse rate constants and fluxes [106-108]. For instance, Ugurbil [107] developed a method referred to as multiplesite saturation transfer (MST) to account for all three phosphate spins in determining the chemical exchange fluxes. It was demonstrated that the equality between the forward and reverse CK fluxes could be obtained in the perfused rat heart only when the two coupled chemical reactions were treated as a three-spin exchange system [106-108]. However, these improved MT methods using the three-spin exchange model have not been applied to the brain in situ, presumably because of the technical complexity involved in measuring the apparent T_1 of γ-ATP based on an inversion recovery (IR) experiment in which both the PCr and Pi spins are saturated simultaneously using a multiple-site saturation pulse train [106-108].

The major objectives of this work were to 1) propose an alternative, simple *in vivo* ^{31}P MT approach for explicitly determining all four rate constants in the PCr↔ATP↔Pi kinetic network, and four associated ATP metabolic fluxes with minimal required *in vivo* ^{31}P spectra; and 2) test this ^{31}P MT approach in the human occipital lobe at 7T. In this paper we will describe how to experimentally determine the forward and reverse fluxes for both the CK and ATPase reactions in the human brain using the proposed ^{31}P MT approach. Moreover, we will demonstrate the validity of the proposed MT approach, and examine the different methodological aspects of the technique. Finally, the merits of the proposed ^{31}P MT approach will be discussed and compared with other existing MT approaches.

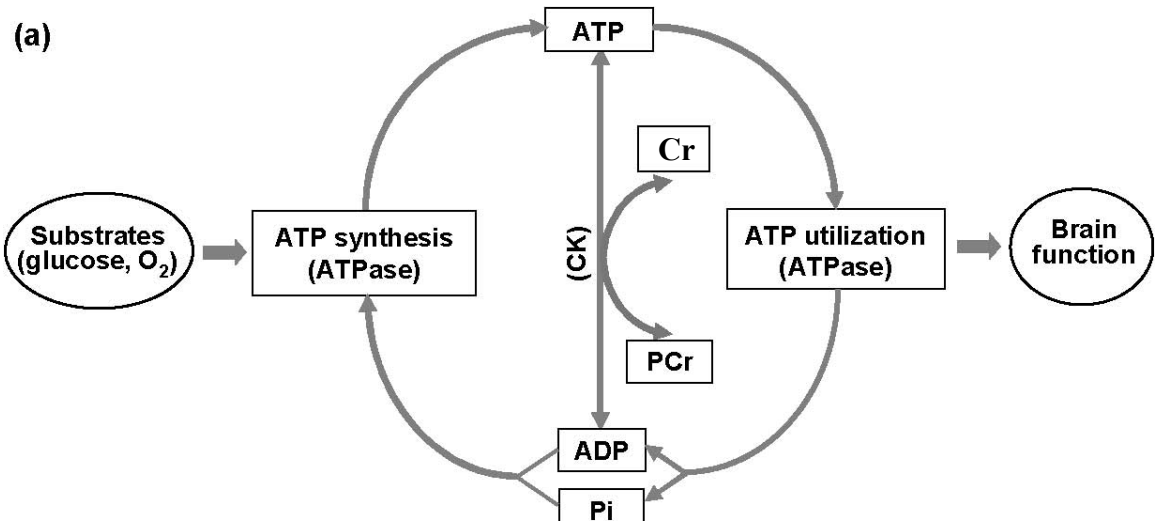

(b)

Figure 5-1 (a) Schematic diagram of the brain metabolic network involving the glucose, oxygen and high-energy phosphate metabolisms. These metabolic pathways are tightly coupled for controlling chemical energy generation (i.e., ATP production) and consumption (i.e., ATP utilization) and for supporting brain function. (b) The entire kinetic network for describing the chemical exchange system of PCr↔ATP↔Pi using the three-spin (PCr, γ-ATP and Pi) exchange model.

5.2 Theory

For the proposed *in vivo* ^{31}P MT approach for determining all kinetic parameters in the PCr↔ATP↔Pi network, a multiple single-site saturation (MSS) method is used and three Bloch equations are solved based on the three-spin chemical exchange model. To simplify the mathematical derivation, the symbols a, b, and c are used to represent PCr, ATP, and Pi, respectively. The Bloch equations that describe the magnetizations of a, b, and c, and their changes as a function of time are given by [63]:

$$\underset{a}{PCr} \underset{k-1}{\overset{k1}{\Leftrightarrow}} \gamma - \underset{b}{ATP} \underset{k2}{\overset{k-2}{\Leftrightarrow}} \underset{c}{Pi}$$

$$\frac{dMa}{dt} = -\frac{(Ma - Ma^0)}{T_{1a}} - k_1 M_a + k_{-1} M_b \qquad [5-1a]$$

$$\frac{dMb}{dt} = -\frac{(Mb - Mb^0)}{T_{1b}} - k_{-1} M_b - k_2 M_b + k_1 M_a + k_{-2} M_c \qquad [5-1b]$$

$$\frac{dMc}{dt} = -\frac{(Mc - Mc^0)}{T_{1c}} - k_{-2} M_c + k_2 M_b \qquad [5-1c]$$

Where Ma, Mb and Mc are the magnetizations of PCr, γ-ATP and Pi; Ma^0, Mb^0 and Mc^0 are magnetizations at Boltzmann thermal equilibrium; k_1 and k_{-2} are the pseudo first-order forward rate constants involving the ATP production via CK reaction and ATPase reaction, respectively; k_{-1} and k_2 are the pseudo first-order reverse rate constants involving the ATP utilization via CK reaction and ATPase reaction, respectively; T_{1a}, T_{1b} and T_{1c} are the intrinsic spin-lattice relaxation times for PCr, γ -ATP and Pi, which depend on the magnetic field trength (B_0). Four rate constants in the PCr↔ATP↔Pi kinetic network and four associated ATP metabolic fluxes can be determined by the following three-step experiment:

5.2.1 Step 1: Progressive Saturation of γ-ATP to Determine Intrinsic Spin-Lattice Relaxation Times for PCr and Pi, Forward Rate Constants, and Fluxes

The first step of the ^{31}P MT experiments is to apply a frequency-selective radiofrequency (RF) pulse train to completely saturate the γ -ATP resonance peak with varied saturation time (t). (This is the progressive saturation experiment commonly used in CST approaches). For this case, the three-spin chemical exchange system of

PCr↔ATP↔Pi can be treated as two independent two-spin chemical exchange systems (i.e., PCr↔ATP and ATP↔Pi). Solving Eqs. [5-1a] and [5-1c] with the boundary condition of $M_b = 0$ results in Eqs. [5-2a] and [5-2b] [109],

$$M_a(t) = M_a^0[(\frac{k_1}{\alpha_a})e^{-\alpha_a t} + (\frac{1}{\alpha_a T_{1a}})] \qquad [5-2a]$$

$$M_c(t) = M_c^0[(\frac{k_{-2}}{\alpha_c})e^{-\alpha_c t} + (\frac{1}{\alpha_c T_{1c}})] \qquad [5-2b]$$

$$\alpha_a = \frac{1}{T_{1a}^{app}} = (k_1 + \frac{1}{T_{1a}})$$

$$\alpha_c = \frac{1}{T_{1c}^{app}} = (k_{-2} + \frac{1}{T_{1c}})$$

Therefore, the parameters of the apparent spin-lattice relaxation rates (a_a and a_c) and intrinsic spin-lattice relaxation times (T_{1a} and T_{1c}) at a given B_0 can be determined first by regressions of Eqs. [5-2a] and [5-2b] as a function of t. The forward rate constants (k_1 and k_{-2}) can then be calculated by their relations with the apparent spin-lattice relaxation rate and intrinsic spin-lattice relaxation time, as defined above.

When a steady-state condition is approached with complete saturation of γ -ATP (i.e., dMa/dt = 0 and dMc/dt = 0), Eqs. [5-2a] and [5-2b] can be further simplified to the following formulae:

$$k_1 = \frac{\Delta M_a}{M_a^0}\alpha_a = \frac{\Delta M_a}{M_a^{*b}}T_{1a}^{-1} \qquad [5-2c]$$

$$k_{-2} = \frac{\Delta M_c}{M_c^0}\alpha_c = \frac{\Delta M_c}{M_c^{*b}}T_{1c}^{-1} \qquad [5-2d]$$

Where M_a^{*b} and M_c^{*b} are the steady-state magnetizations of **a** and **c**, when **b** is fully saturated; and

$$\Delta M_a = M_a^0 - M_a^{*b}$$
$$\Delta M_c = M_c^0 - M_c^{*b}$$

Therefore, the forward chemical exchange rate constants of k_1 and k_{-2} also can be calculated by using Eqs. [5-2c] and [5-2d]. For this case, only two steady-state spectra acquired in the presence and absence of saturating b are needed to determine both k_1 and k_{-2} if T_{1a} and T_{1c} have already been determined at a given B_0 via the progressive saturation experiment (i.e., the step 1 experiment).

Finally, the forward fluxes for the CK (F_f^{CK}) and ATPase (F_f^{ATPase}) reactions can be determined by the following equations:

$$F_f^{CK} = k_1[PCr] \text{ and } F_f^{ATPase} = k_{-2}[Pi] \qquad [5\text{-}2e]$$

5.2.2 Step 2: Steady-state Saturation of Pi to Determine the CK Reverse Rate Constant and Flux

The second step of the proposed *in vivo* ^{31}P MSS MT experiments is to apply a frequency-selective RF pulse train for completely saturating the Pi resonance peak with a sufficiently long saturation time, resulting in steady-state magnetizations of a and b. For this case, Mc = 0, dMa/dt = 0, dMb/dt = 0 and Eqs. [5-1a] and [5-1b] yield

$$k_{-1} = \alpha_a \left(\frac{M_a^{*c}}{M_a^0} - \frac{T_{1a}^{-1}}{\alpha_a}\right)\frac{M_a^0}{M_b^{*c}} \qquad [5-3a]$$

$$k_1 = \alpha_b \left(\frac{M_b^{*c}}{M_b^0} - \frac{T_{1b}^{-1}}{\alpha_b}\right)\frac{M_b^0}{M_a^{*c}} \qquad [5-3b]$$

with

$$\alpha_b = \frac{1}{T_{1b}^{app}} = (k_2 + k_{-1} + T_{1b}^{-1})$$

Where Ma^{*C} and Mb^{*C} are the steady-state magnetizations of a and b, respectively, when c is fully saturated. Only Eq. [5-3a] is needed in the MSS MT approach to determine the CK reverse rate constant (k_{-1}) by using the measured magnetizations (i.e., M_a^0, $M^*{}_a^c$ and $M^*{}_b^c$) and other relaxation parameters (i.e., α_a and T_{1a}), which are determined by the step 1 experiment. The reverse flux of the CK reaction (F_r^{CK}) can be calculated by

$$F_r^{CK} = k_{-1}[ATP] \qquad [5\text{-}3c]$$

5.2.3 Step 3: Steady-state Saturation of PCr to Determine the ATPase Reverse Rate Constant and Flux

The third step of the proposed *in vivo* ^{31}P MSS MT experiments is to apply a frequency-selective RF pulse train to completely saturate the PCr resonance peak with a sufficiently long saturation time, resulting in steady-state magnetizations of **b** and **c**. For this case,

$$Ma = 0,\ dMb/dt = 0,\ dMc/dt = 0$$

And the solution of Eqs. [5-1b] and [5-1c] yields

$$k_2 = \alpha_c \left(\frac{M_c^{*a}}{M_c^0} - \frac{T_{1c}^{-1}}{\alpha_c}\right)\frac{M_c^0}{M_b^{*a}} \qquad [5-4a]$$

$$k_{-2} = \alpha_b \left(\frac{M_b^{*a}}{M_b^0} - \frac{T_{1b}^{-1}}{\alpha_b}\right)\frac{M_b^0}{M_c^{*a}} \qquad [5-4b]$$

Where Mb^{*a} and Mc^{*a} are the steady-state magnetizations of b and c when a is fully saturated. Only Eq. [5-4a] is needed in the MSS MT approach to determine the ATPase reverse rate constant (k_2) by using the measured magnetizations (i.e., M_c^0, $M^*{}_c^a$ and $M^*{}_b^a$) and other relaxation parameters (i.e., α_c and T_{1c}), which are determined by the step 1 experiment. The reverse flux of the ATPase reaction (F_r^{ATPase}) can be calculated by

$$F_r^{ATPase} = k_2[ATP] \qquad [5\text{-}4c]$$

Therefore, by combining these three measurement steps, one can measure all parameters that determine the entire kinetic network of PCr↔ATP↔Pi, as well as all associated ATP metabolic fluxes for both forward and reverse reaction directions as schematically summarized in Fig. 5-1.

Although Eqs. [5-3b] and 5-[4b] are not required in the proposed MSS MT approach, they can be solved to calculate the apparent spin-lattice relaxation rate of γ -ATP (i.e., α_b) by using the values of k_1 and k_{-2} as obtained in the step 1 experiment. Then the apparent spin-lattice relaxation time of γ -ATP (T_{1b}^{app}) can be calculated by the relation of $T_{1b}^{app} = 1/\alpha_b$. This calculation is performed to determine the T_{1b}^{app} value in the human brain. This value is then compared with other values determined independently

using the IR experiment when both the PCr and Pi resonance peaks are saturated.

5.3 Methods and Materials

5.3.1 Human Subjects and MR Hardware

A total of 40 healthy human subjects (15 males and 25 females, 24±3 years old) were recruited for this study. They were divided into four subgroups for the following *in vivo* ^{31}P MT experiments: 1) progressive saturation experiments by saturating γ -ATP as described in step 1 (N = 11); 2) steady-state saturation experiments (N = 7) as described in steps 2 and 3, and progressive saturation experiments (N = 9) by saturating PCr and Pi, respectively; 3) IR experiments with simultaneous RF saturation on the Pi and PCr resonance peaks to measure the apparent spin-lattice relaxation time and rate of γ -ATP (N = 7); and 4) experiments to determine the offset RF saturation effect (N = 6). The total MR measurement time for each experimental session was less than 2.5 hr. All subjects gave informed written consent and the study procedure was approved by the Institutional Review Board of the University of Minnesota.

The MR experiments were conducted on a 7T 90-cm bore magnet (Magnex Scientific, Abingdon, UK) interfaced with a Varian INOVA console (Palo Alto, CA, USA). A passively decoupled dual RF coil probe was used. This probe consisted of a linear butterfly ^{1}H surface coil for anatomical imaging and B_0 shimming, and a 5-cm-diameter single-loop ^{31}P surface coil tuned at 119.6 MHz to acquire *in vivo* ^{31}P spectra.

The FASTMAP autoshimming algorithm [110] was used to perform shimming within a 3 × 3 × 3 cm^3 volume located inside the occipital lobe to minimize B_0 inhomogeneity and improve spectral quality.

5.3.2 *In vivo* ^{31}P Experiments

The pulse sequence used for the *in vivo* ^{31}P MT experiments was described previously [35, 65]. Briefly, an RF pulse train constructed by multiple hyperbolic secant pulses (pulse width = 50 ms, frequency-selective bandwidth = 150 Hz) with varied RF pulse amplitudes (according to a B_1-insensitive selective train to obliterate signal (BISTRO) scheme [111]) was used to selectively saturate only one resonance peak (γ - ATP, PCr or Pi). The saturation time for performing the progressive saturation experiments (0.0–10 s) was controlled by varying the cycling number of the BISTRO pulse train. For the steady-state saturation experiments, a saturation time of 7.64 s was adequate for achieving frequency-selective saturation of one desired phosphate spin, while the other two chemically coupled phosphate spins attained steady-state magnetizations. A 200-μs hard RF pulse was used to excite the phosphate spins and its flip angle was adjusted to achieve maximal NMR signal from the human occipital lobe [35, 65].

In vivo ^{31}P spectra were acquired using the following acquisition parameters: 5000 Hz spectral width, 1024 complex data points, and 32 or 64 signal averages. The criterion to justify the number of averages for a particular experiment was based on the

magnitude of the phosphate NMR signal and the MT effect. For instance, since the RF saturation of γ -ATP can lead to a large reduction in the PCr resonance peak, fewer signal averages are needed. There was one exception in which a total of 128 signal averages were used to acquire an *in vivo* ^{31}P brain spectrum for the purpose of illustration. All *in vivo* ^{31}P spectra were acquired with a long TR (≥16 s) to minimize the complication of T_1 saturation effects. The duty cycle rate of the RF saturation pulse train was less than 63%, and the specific absorption rate (SAR) was below the FDA limit.

To measure the apparent spin-lattice relaxation time of γ -ATP (i.e., T_{1b}^{app}), the pulse sequence described above was further modified. First, the RF saturation pulse with a single saturation frequency band was replaced by a hyperbolic secant RF pulse (pulse width = 62 ms) with two identical saturation frequency bands (158 Hz width for each band) separated by 580 Hz between the band centers, which equals the chemical shift difference (in Hz) between the PCr and Pi resonance peaks at 7T. This modified BISTRO saturation pulse train was used to simultaneously and continuously saturate PCr and Pi. Second, a 10-ms adiabatic inversion pulse with a 4000-Hz inversion bandwidth was applied to invert the γ -ATP and other phosphate resonance peaks. This pulse was inserted during the simultaneous saturation of PCr and Pi with a varied IR time.

The offset RF saturation effect due to the imperfection of the saturation frequency profile of the BISTRO pulse train was experimentally determined for each saturation time using the resonance peak from a chemically non-exchangeable phosphate metabolite. The ratios of two magnetizations obtained in the absence and/or presence of the BISTRO

pulse train at a selected saturation frequency provided the correction factors for this saturation frequency at each saturation time. These correction factors were applied to the saturated *in vivo* ^{31}P spectra obtained in this work. In addition, the results obtained without correcting the offset RF saturation effect are reported for the purpose of comparison.

5.3.3 Data Processing of *in vivo* ^{31}P Spectra

The integrals of the PCr, ATP, and Pi resonance peaks were quantified by spectral fitting using the AMARES algorithm provided by the MRUI software package. The baseline correction and line-broadening were not required by this algorithm based on the time-domain fitting method. Only the prior knowledge of the number of resonance peaks to be fitted, estimated resonance peak chemical shifts, and their line widths and phases were used in the spectral fitting.

The absolute concentrations of ATP, PCr, and Pi were not directly measured in this study. Under normal physiological conditions, the ATP concentration is relatively constant compared to [PCr] and [Pi] because of the tight ATP metabolic regulation. Therefore, we took the [ATP] value of 3 mM from the literature. We used this ATP concentration to calculate [PCr] and [Pi] by using the resonance peak integral ratios of PCr/ATP and Pi/ATP, which were measured by the fully relaxed *in vivo* ^{31}P spectra acquired in this study. These phosphate metabolite concentrations were used to calculate the ATP metabolic fluxes according to Eqs. [5-2e], [5-3c], and [5-4c].

For the experiments using progressive saturation of the γ -ATP resonance, we determined the apparent and intrinsic spin-lattice relaxation times of PCr and Pi, as well as the forward chemical exchange rate constants, by fitting the experimental data to a single exponential decay according to Eqs. [5-2a] and [5-2b], using the least-square regression algorithm. The apparent spin-lattice relaxation time of γ -ATP measured via the IR experiment in the presence of simultaneous saturation of both the PCr and Pi resonance peaks was deduced by exponential fitting of the γ -ATP peak integral as a function of IR time. The chemical shift of the PCr resonance peak was assigned to 0.0 ppm. The data and results are reported as the mean ± standard deviation (SD). Statistical analysis was based on the unpaired two-tailed t-test.

5.4 Results

5.4.1 *In Vivo* ^{31}P Spectra, Phosphate Metabolite Concentrations, and MT Results

Figure 5-2 demonstrates typical *in vivo* ^{31}P spectra obtained from a representative subject in the absence (Fig. 5-2a) and presence of complete saturation of Pi (Fig. 5-2b), PCr (Fig. 5-2c), and γ -ATP (Fig. 5-2d). It illustrates that single-site saturation on one phosphate spin can lead to significant magnetization reductions in the other two coupled phosphate spins through the three-spin chemical exchange system of PCr ↔ ATP ↔ Pi. For an instance, the saturation of γ -ATP resulted in a significant signal reduction for both PCr and Pi, as shown in Fig. 5-2d. The collected ^{31}P spectra were quantified via spectral curve fitting to determine the integrals of all detected phosphate resonance peaks. A

spectral curve-fitting result is illustrated in Fig. 5-3, indicating an excellent spectral fitting quality with negligible residues. In the acquired *in vivo* ^{31}P spectra, the resonance peak at 4.83 ppm is attributed to intracellular Pi (assigned as Pi), and the small and partially overlapped resonance peak at 5.26 ppm is presumably attributed to extracellular Pi (assigned as Pi^{ex}) [112]. These two resonance peaks are resolved at 7T, as shown in Figs. 5-2 and 5-3.

The average integral ratios obtained from the fully relaxed ^{31}P spectra in the absence of RF saturation were PCr/ γ -ATP =1.33 ± 0.14, γ -ATP/Pi = 3.34 ± 0.56, and γ -ATP/Pi^{total} = 2.44 ± 0.38 (N = 16; Pi^{total} = Pi + Pi^{ex}). If the ATP concentration in the human brain was assumed to be 3 mM (see Ref. [71] and references therein), other phosphate metabolite concentrations were calculated as [PCr] = 3.99 ± 0.42 mM, [Pi] = 0.90 ± 0.16 mM and [Pi^{total}] = 1.23 ± 0.20 mM (N = 16), respectively, based on the integral ratios (proportional to concentration ratios) that were experimentally measured in this work. These absolute concentrations are in agreement with values reported in the literature [71, 85, 113].

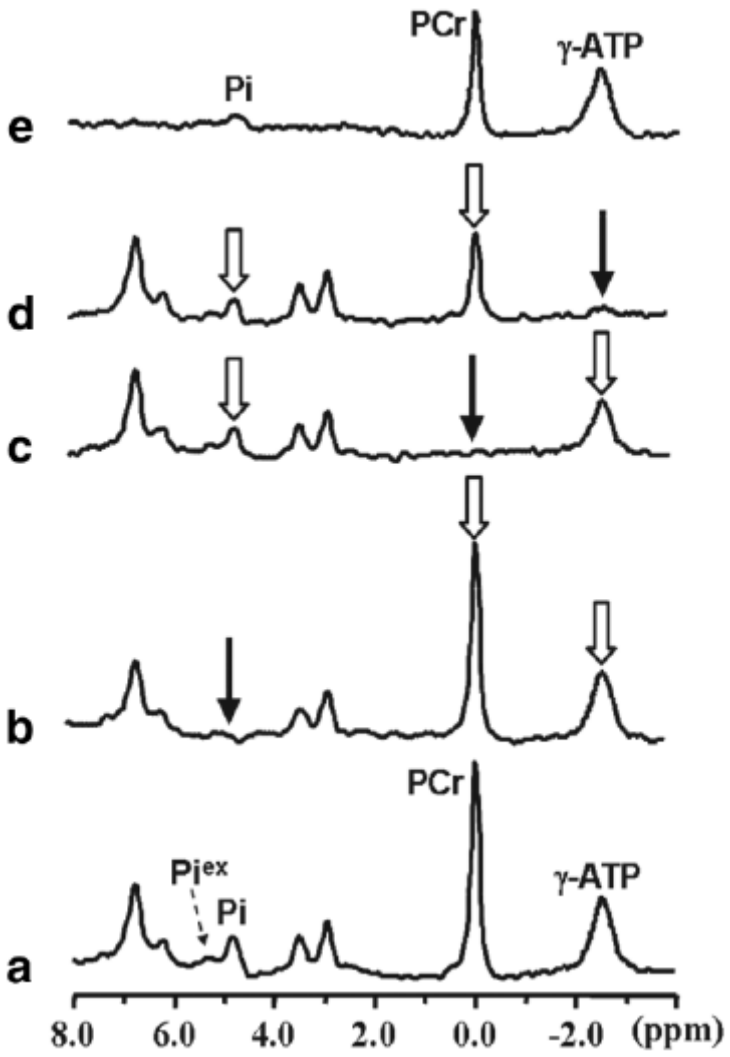

Figure 5-2 *In vivo* ^{31}P spectra acquired from a representative subject in the absence (a) and presence of complete saturation on the resonance of P_i (b), PCr (c) and γ-ATP (d), respectively. (e) Difference spectrum between (a) and (d). Saturation time was 7.6 s. The narrow arrows indicate the saturation sites and the wide arrows indicate the signal reductions due to the magnetization transfer.

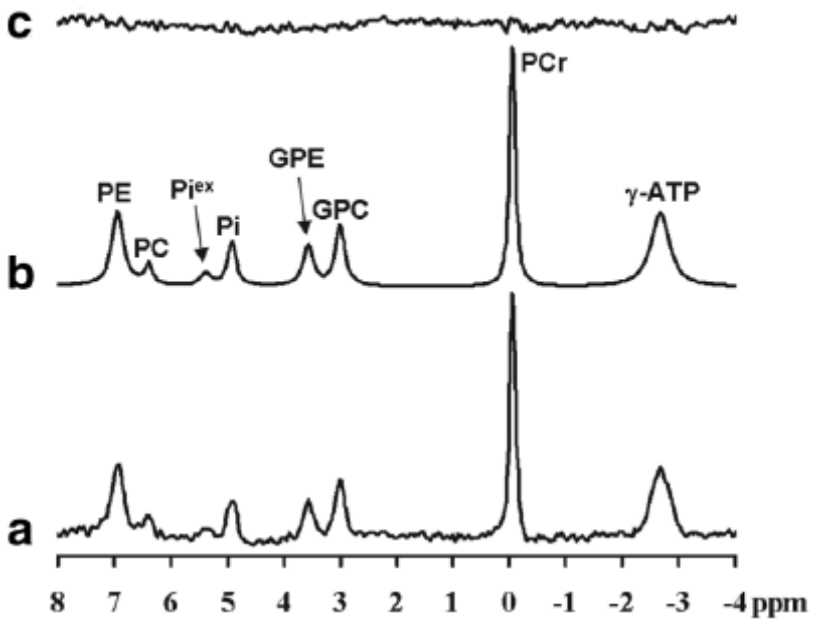

Figure 5-3 (a) A typical *in vivo* ^{31}P spectrum obtained from the visual cortex of a representative subject (128 scans, 16-s repetition time and 1-Hz line broadening) and (b) its fitted spectrum. (c) The residue spectrum by the subtraction between the original and fitted spectra. PE: phosphoethanolamine; PC: phosphocholine; Pi^{ex}: extracellular inorganic phosphate; Pi: intracellular inorganic phosphate; GPE: glycerophosphoethanolamine; GPC: glycerophosphocholine; PCr: phosphocreatine; ATP: adenosine triphosphate.

5.4.2 Evidence That Pi Has Distinct Roles in Chemical Exchange Reactions Between Extra- and Intracellular Compartments

Although it is generally accepted that pH differs between extra- and intracellular

compartments [114, 115], and two distinct NMR peaks of Pi have been detected in the neonatal pig brain [112], no resolved Pi resonance peak coming from the extracellular compartment in the human brain has been clearly demonstrated by *in vivo* ^{31}P MRS. In this study the high magnetic field and improved spectral resolution (the half-height linewidth of PCr without linebroadening was ≤11 Hz) at 7T made it possible to resolve the two adjacent Pi resonance peaks (see Figs. 5-2 and 5-3) in the human occipital lobe. The chemical shift difference between the Pi and PCr resonance peaks was used for pH calculation [115], resulting in pH = 7.02 ± 0.01 (N = 16) determined by the intracellular Pi peak at 4.83 ppm, and pH = 7.40 ± 0.04 (N = 16) determined by the extracellular Pi peak at 5.26 ppm. The measured extracellular pH value is identical to the human blood pH value (≈ 7.4).

Figure 5-2e shows the difference spectrum between the control spectrum (Fig. 5-2a) and the γ -ATP saturated spectrum (Fig. 5-2d). It indicates that the saturation of γ – ATP results in a significant magnetization reduction of intracellular Pi without a detectable change in the extracellular Pi signal. This experimental observation suggests that the exchange rate between the extra- and intracellular Pi compartments may be relatively slow, and that extracellular Pi may not significantly contribute to the ATPase reaction. Therefore, only intracellular Pi is essential for determining the ATP metabolic fluxes associated with the PCr ↔ ATP ↔ Pi exchange system. On the other hand, the NMR signal of extracellular Pi has to be separated and excluded from the intracellular Pi NMR signal for absolute [Pi] quantification in order to precisely calculate the metabolic

forward flux of the ATPase reaction according to Eq. [5-2e]. Otherwise the calculated Ff ATPase value can be overestimated. Thus, in this study only the intracellular Pi concentration ([Pi] = 0.9 mM) was used to calculate Ff^{ATPase}.

5.4.3 Unidirectional Forward Exchange Rate Constants and Fluxes Determined by Saturating γ -ATP

Figure 5-4 shows the dependence of the averaged and normalized resonance peak integrals of PCr and Pi on the γ-ATP saturation time (N = 11) during the progressive saturation experiment (i.e., the step 1 experiment), as well as their least-square regression curves according to Eqs. [5-2a] and [5-2b]. The spin-lattice relaxation times, T_1^{app} and T_1^{int}, of PCr and the forward exchange rate constant from PCr to ATP (i.e., k_1) were determined to be 1.97 ± 0.20 s, 4.89 ± 0.54 s, and 0.30 ± 0.04 s^{-1}, respectively. The spin-lattice relaxation times, T_1^{app} and T_1^{int}, of Pi and the forward exchange rate constant from Pi to ATP (i.e., k_{-2}) were determined to be 2.24 ± 0.32 s, 3.77 ± 0.53 s, and 0.18 ± 0.05 s^{-1}, respectively. The measured forward rate constants were consistent with other reports [65, 100, 102]. The measured values of k_1 and k_{-2}, [PCr], and [Pi], which were determined by the metabolite concentration ratios and [ATP] = 3 mM taken from the literature, were used to calculate the forward exchange fluxes according to Eq. [5-2e]. The calculation yielded F_f^{CK} = 1.19 mM/s and F_f^{ATPase} = 0.16 mM/s. These fluxes were converted to F_f^{CK} = 65.1 ± 7.2 μmol/g/min and F_f^{ATPase} = 8.8 ± 1.9 μmol/g/min (N = 11) with the more popular metabolic rate unit of μmol/g/min by using the brain tissue density of 1.1 g/ml.

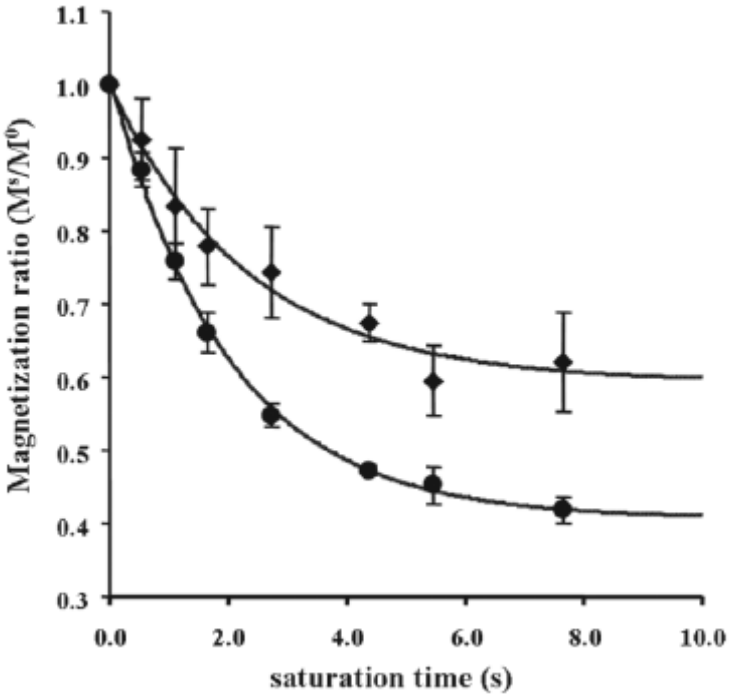

Figure 5-4 Plot of the resonance peak integrals of PCr (full cycles) and Pi (full diamonds) as a function of γ-ATP saturation time (presented by the normalized ratio M^s/M^0 averaged from seven subjects), and their least-square regression curves according to Eqs. [5-2a] and [5-2b], respectively. The apparent and intrinsic spin-lattice relaxation times of PCr and Pi, the forward rate constants of k_1 and k_{-2} can be determined by the regressions.

5.4.4 Reverse Exchange Rate Constants and Fluxes Determined by Saturating PCr and Pi, Respectively

Both steady-state (N = 7) and progressive saturation (N = 9) experiments (saturating PCr or Pi) were performed and the data from both experiments were used for calculations. Figure 5-5 shows the dependence of the averaged and normalized γ -ATP peak integrals on the PCr and Pi saturation time, respectively. Based on the three-spin exchange model and the MSS MT approach, one can determine the values of reverse chemical exchange rate constants and fluxes with the single-site and steady-state saturation approach by either completely saturating Pi (step 2) to calculate k_{-1} according to Eq. [5-3a], or saturating PCr (step 3) to calculate k_2 according to Eq. [5-4a]. The steady-state magnetization ratios between the fully saturated and control conditions (as summarized in Table 5-1), as well as the apparent and intrinsic T_1 values of both PCr and Pi determined by the step 1 experiment were used in the calculations according to Eqs. [5-3a] and [5-4a]. The measured k_{-1} and k_2 were 0.42 ± 0.05 s^{-1} and 0.05 ± 0.01 s^{-1} (N = 16; see Table 5-1). These rate constants were applied to calculate the reverse flux of the CK reaction (Fr^{CK} = 68.7 ± 5.4 μmol/g/min) according to Eq. [5-3c], and the reverse flux of the ATPase reaction ((Fr^{ATPase} = 8.2 ± 2.1 μmol/g/min) according to Eq. [5-4c].

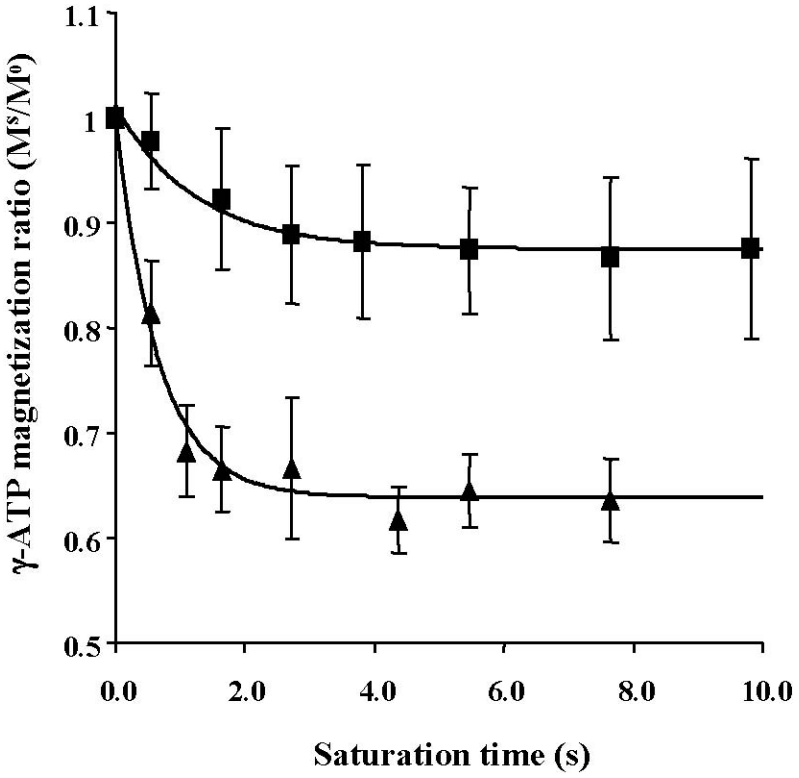

Figure 5-5 Dependence of the normalized γ-ATP resonance peak integral on the PCr saturation time (full triangles) and the Pi saturation time (full squares) averaged from nine subjects, and their least-square regression curves using the similar equations as Eqs. [5-2a] and [5-2b] based on the two-spin exchange model.

5.4.5 Independent Measurements and Comparison of Apparent γ -ATP T_1 Values

We used two independent approaches in this study to determine the apparent spin-lattice relaxation time of γ -ATP (i.e., T_{1b}^{app}) at 7T. The first approach was to solve Eqs. [5-3b] and [5-4b], resulting in $T_{1b}^{app} = 0.71 \pm 0.07$ s (see Theory and Table 5-1). The

second approach is based on the IR measurement. Figure 5-6 shows the time course of γ –ATP magnetization recovery as a function of IR time when both PCr and Pi were saturated simultaneously. An exponential fitting of the time course yielded T_{1b}^{app} = 0.66 ± 0.12 s (see Methods and Materials and Table 5-1). The difference between these two independently measured T_{1b}^{app} values was within standard deviation. The results of this comparison between two independent measurements indirectly support the validity of the MSS MT approach in regards to the methodology.

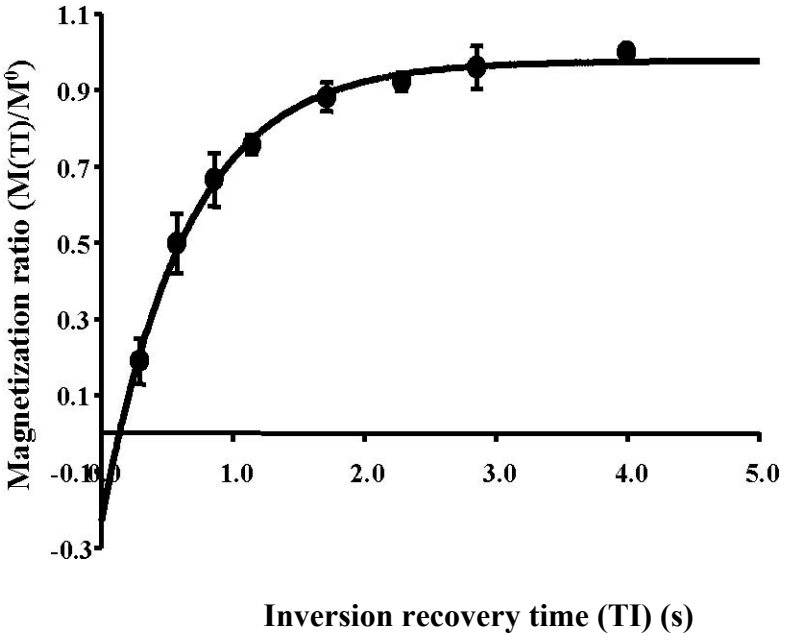

Figure 5-6 Recovery time course of the γ-ATP magnetization as a function of inversion recovery time when PCr and P_i were saturated simultaneously (averaged from seven subjects).

Table 5-1 summarizes the mean values and SDs of the M^{*s}/M^0 ratios, T_1 relaxation times, and the forward and reverse rate constants and fluxes for the CK and ATPase reactions, as measured by the *in vivo* ^{31}P MSS MT approach in the human occipital lobe at 7T. The results derived with or without correcting for the offset RF saturation effect are all included in Table 5-1.

5.5 Discussion

5.5.1 Comparison of CK and ATPase Forward and Reverse Fluxes in Human Brain

In this study we experimentally determined four chemical exchange fluxes involving the three-spin chemical exchange system of PCr↔ ATP ↔ Pi in the human occipital lobe by using the MSS MT approach. An unpaired, two tailed t-test between the forward and reverse chemical exchange fluxes gave P = 0.38 for the CK reaction (i.e., F_f^{CK} vs. F_r^{CK}) and P = 0.46 for the ATPase reaction (i.e., F_f^{ATPase} vs. F_r^{ATPase}). These statistical comparisons indicate that there was no statistical difference between the measured forward and reverse chemical exchange fluxes for either the CK reaction or the ATPase reaction. The ratios between the forward and reverse fluxes for the CK reaction ($F_f^{CK} / F_r^{CK} = 0.95 \pm 0.12$) and the ATPase reaction ($F_f^{ATPase} / F_r^{ATPase} = 1.08 \pm 0.21$) were close to unity. In general, the CK fluxes reflect the nonoxidative phosphorylation, whereas the ATPase fluxes reflect oxidative phosphorylation. Both of these phosphorylation pathways can contribute to the total ATP production flux (i.e., F_f^{total} =

$F_f^{CK} + F_f^{ATPase} = 73.9$ μmol/g/min) and the total ATP utilization flux (i.e., $F_r^{total} = F_r^{CK} + F_r^{ATPase} = 76.9$ μmol/g/min). The ratio between F_f^{total} and F_r^{total} was again close to unity (= 0.96), indicating that the measured total ATP production flux equals the total ATP utilization flux. These results reveal that the fluxes measured in this study satisfy the chemical equilibrium conditions for the CK and ATPase reactions in the human brain. They support the notion that the MSS MT approach can explicitly determine four rate constants in the PCr↔ ATP ↔ Pi kinetic network and their associated ATP metabolic fluxes.

The observed unity relations among individual reaction fluxes, or the total reaction fluxes in this study, provide evidence that both the CK reaction and the ATPase reaction are near the chemical equilibrium condition in the normal human brain.

5.5.2 Comparison of Measured Oxidative ATP Production Flux and Estimated Oxidative Phosphorylation Rate in Human Brain

Under normal physiological conditions, a tight coupling between cerebral oxidative phosphorylation and oxygen metabolism occurs, mainly inside the mitochondria [86]. The cerebral metabolic rate of oxygen utilization ($CMRO_2$) in the human occipital lobe was previously measured (=1.71 μmol/g/min) by positron emission tomography (PET) [116]. The ATP synthesis rate through oxidative phosphorylation can be estimated by multiplying $CMRO_2$ and the $P:O_2$ ratio. Classically, 3 moles of ATP molecule can be generated from 1 mole of NADH and 1/2 mole of oxygen molecule,

resulting in a $P:O_2$ ratio of 6. However, most experimental measurements have shown that the $P:O_2$ ratio is approximately 5 [117]. Taking $P:O_2$ ratio = 5, the cerebral ATP synthesis rate through oxidative phosphorylation estimated from the PET result of $CMRO_2$ measurement is 8.6 μmol/g/min in the human occipital lobe. This estimated rate is in excellent agreement with the cerebral ATP synthesis flux of F_f^{ATPase} = 8.8 μmol/g/min as directly measured in this study. This comparison indicates that the Pi → ATP synthesis rate measured by the *in vivo* ^{31}P MT approach equals the net oxidative ATP phosphorylation rate in the human brain. It is well known that oxidative phosphorylation is extremely efficient for producing a large amount of ATP from the substrates of glucose and oxygen supplied through blood flow circulation. In comparison with other measurable physiological parameters (e.g., cerebral blood flow, cerebral metabolic rate of glucose, and $CMRO_2$), the oxidative ATP synthesis and utilization fluxes as determined in this study should provide a more direct and quantitative measure reflecting the true brain bioenergetic state and changes associated with brain function and physiological and/or pathological perturbations [87]. Therefore, direct and noninvasive measurements of cerebral oxidative ATP synthesis rate should be useful for elucidating the function and bioenergetics of the brain.

5.5.3 Comparison of Two- and Three-Spin Exchange Models for ST Measurements

The *in vivo* ^{31}P MRS MT approach was developed as early as the 1970s, and was mainly used to measure the CK flux *in vivo* (e.g., Ref. [104]). The forward and reverse flux ratios of the CK reaction (i.e., F_f^{CK} / F_r^{CK}) have been reported by a number of

studies. The CST approach was commonly used in early studies, in which the contribution of the ATPase reaction of ATP ↔ Pi was mostly neglected to simplify the determination of the reverse CK rate constant (i.e., the two-spin chemical exchange model of PCr ↔ ATP). This simplification has been speculated to be the leading cause of the non-unity results in the measured CK flux ratio of F_f^{CK}/F_r^{CK} in both hearts and brains [91, 93, 98, 101-103, 106]. However, this notion has been rigorously tested and confirmed only in perfused rat hearts [92, 106-108]. In this study we were able to compare various parameters, including apparent and intrinsic T_1 values, reverse chemical exchange rate constants, and reverse chemical exchange fluxes, deduced from the three-spin exchange model with those deduced from the two-spin exchange model using the same *in vivo* ^{31}P MRS data as shown in Fig. 5-5. We investigated the influence of the spin-exchange model on the calculated parameter values. The comparison results are summarized in Table 5-1.

First, there are large discrepancies among the measured apparent and intrinsic T_1 values of γ-ATP using two different models. For instance, the value of γ -ATP T_1^{app} (i.e., T_{1b}^{app} = 1.43 ± 0.32 s) that was determined with the two spin exchange model was much higher than that (T_{1b}^{app} = 0.71 ± 0.07 s) determined by the three-spin exchange model. In contrast, the value of γ -ATP T_1^{int} (0.94 ± 0.27 s) determined by the two-spin exchange model was significantly lower than that determined by the three-spin exchange model (1.35 ± 0.17 s). Second, the calculated reverse rate constants (k_{-1} = 0.59 ± 0.06 s^{-1}, and k_2 = 0.11 ± 0.03 s^{-1}) based on the two-spin exchange model were overestimated in

comparison with the values obtained with the three-spin exchange model (k_{-1} = 0.42 ± 0.05 s^{-1} and k_2 = 0.05 ± 0.01 s^{-1}). The degree of the overestimations in the calculated reverse rate constant was substantially higher for the ATPase reaction (>100%) than for the CK reaction (40%). The overestimation in the reverse rate constants of k_{-1} and k_2 led to an inequality between the forward and reverse fluxes for both the CK reaction (F_f^{CK} / F_r^{CK}= 0.67 ± 0.13) and the ATPase reaction (F_f^{ATPase} / F_r^{ATPase} = 0.49 ± 0.15). In contrast, the unity flux ratios were obtained only with the three-spin exchange model. Spencer et al. [108] proposed a formula that theoretically predicted that the two-spin chemical exchange model could lead to an underestimation in the measured reverse CK rate constant. We developed a similar but simpler formula based on the three-spin exchange model, as follows:

$$k_{-1} = \frac{\Delta M_b}{T_{1b} M_b^{*a}} + \frac{\Delta M_c}{T_{1c} M_b^{*a}} \qquad [5-5]$$

Here the PCr resonance peak is completely saturated, and both γ-ATP and Pi magnetizations have reached a steady state. The form of the first term on the right side of Eq. [5-5] is similar to that used by the conventional two-spin exchange model for calculating k_{-1}. However, both T_{1b} and T_{1c} in Eq. [5-5] should present the true T_1 values defined by the three-spin exchange model. It is clear that k_{-1} could be underestimated using the two-spin exchange model if the T_{1b} value deduced from the two-spin exchange model is close to or the same as that deduced from the three-spin exchange model, because the neglected second term on the right side of Eq. [5-5] is always larger than

zero. Nevertheless, our data acquired from the human brain at 7T indicate an overestimation of 40% in the calculated k_{-1} value using the two-spin exchange model. To solve this discrepancy, we estimated the relative contributions of the two terms in Eq. [5-5] to the calculated k_{-1} value by using the steady-state magnetization and T_1 results determined by the three-spin exchange model (see Table 5-1) and the concentration ratio of [ATP]/[Pi] = 3.34. We found that k_{-1} was dominated by the first term (0.417 s^{-1}) as compared to the second term (0.026 s^{-1}, only a 6% contribution) at 7T. The two-spin exchange model itself is unable to give a true intrinsic T_{1b} value as required by Eq. [5-5]. The T_{1b} value (0.94 s) determined by the two-spin exchange model was underestimated by 44% as compared to the true T_{1b} value (1.35 s) determined by the three-spin exchange model (see Table 5-1). This underestimation of T_{1b} in Eq. [5-5] caused by the two-spin exchange model resulted in a ~ 40% overestimation of k_{-1} in this study conducted at 7T. This analysis indicates that the T_{1b} measurement is the major source of a significant error in the determination of k_{-1} and the reverse flux of the CK reaction using the two-spin exchange model. The magnitude of T_{1b} error in the two-spin exchange model is expected to be dependent on the magnetic field strength.

The overall comparison results clearly indicate that one must treat the chemical exchange system of PCr↔ ATP ↔ Pi as a three-spin exchange system in order to accurately determine the reverse rate constants and fluxes for both the CK and ATPase reactions.

5.5.4 Methodology Comparison of the MSS and Other MT Approaches

One interesting methodological distinction between the MSS MT approach based on the three-spin exchange model and the CST method based on the two-spin exchange model lies in the experimental measurements. In the MSS MT approach, the reverse rate constant or flux of the CK reaction was determined via the saturation of the indirectly coupled Pi spin (see Fig. 5-1b). In contrast, it was determined via the saturation of the directly coupled PCr spin in the CST method. This is also true for the ATPase reaction. The frequency-selective saturation of the PCr or Pi resonance peak could lead to a significant MT effect (or signal reduction) not only in the directly coupled phosphate metabolite (i.e., γ-ATP), but also in the indirectly coupled metabolite Pi (~21%) or PCr (~6%). Here the γ -ATP spin acts as a bridge to connect the PCr and Pi magnetizations through the chemical exchange kinetic network of PCr↔ ATP ↔ Pi. These facts again indicate that all unidirectional forward and reverse CK and ATPase reactions (a total of four) have to be considered in the Bloch equations (i.e., the three-spin chemical exchange model) as applied in this study.

Although an important strategy for testing the MSS MT approach in this study was to examine whether the measured forward and reverse CK and ATPase fluxes satisfied the chemical equilibrium conditions, the MSS MT approach itself does not require the constraint of a chemical equilibrium assumption. Thus, the MSS MT approach would provide a general and useful tool for explicitly studying the kinetic network of PCr↔ ATP ↔ Pi and associated ATP metabolic fluxes *in vivo* under near or

nonequilibrium conditions if the rate constants and fluxes are relatively stable during the MSS MT measurement. For instance, during the transition time after the initiation of pathological perturbation (e.g., acute ischemia), the concentrations of PCr and Pi or ATP would change, leading to a non-equilibrium biological system. The extent and direction of the imbalance between the forward and reverse fluxes would influence the trend of the metabolite concentration changes, and could determine the new steady-state concentrations when the biological system reached a new chemical equilibrium condition. Such ability should be crucial for quantitatively understanding the kinetics of the PCr ↔ ATP ↔ Pi exchange system and its impact on cerebral bioenergetics associated with brain function and diseases.

Several MT approaches based on the three-spin exchange model have been reported and applied to study the PCr↔ ATP ↔ Pi chemical exchange system in perfused rat hearts [106-108]. In addition to acquiring a number of saturated *in vivo* ^{31}P spectra, these approaches also need to determine the apparent γ-ATP T_1 value (i.e., T_{1b}^{app}) using the IR measurements with varied IR times when the PCr and Pi resonance peaks are simultaneously and continuously saturated (e.g., see Fig. 5-6), which require a lengthy measurement time. Moreover, T_{1b}^{app} is determined by the intrinsic γ -ATP T_1 (T_{1b}) and two reverse rate constants (k_2 and k_{-1}) as defined in the Theory section, and it is sensitive to the physiological or pathological changes that can affect either k_2 or k_{-1}, or both. Therefore, it is necessary to measure T_{1b}^{app} under each condition of the study. These MT approaches have not been successfully applied to determine the reverse CK and

ATPase rate constants and fluxes in the brain.

In contrast, the MSS MT approach (in principle) only has to acquire three steady-state and single-site (i.e., PCr, γ-ATP, and Pi, respectively) saturated ^{31}P spectra plus one control spectrum. The kinetic parameters can be measured by these four spectra and two intrinsic T_1 relaxation times of PCr and Pi (T_{1a} and T_{1c}), which were measured at 7T in this study using the progressive saturation approach. It has been demonstrated that the intrinsic T_1 relaxation time is usually independent of physiological changes [95]. Therefore, the measured T_{1a} and T_{1c} can be treated as constant at a given magnetic field strength to calculate both the forward and reverse rate constants for the CK or ATPase reaction, as proposed in the MSS MT approach. These methodological advantages enable the MSS approach to acquire a minimal number (four) of *in vivo* ^{31}P spectra (equivalent to a short measurement time) to determine multiple parameters, including four kinetic rate constants and three phosphate metabolite contents or their concentration ratios. In this study we assumed the absolute ATP concentration of normal human brain to be ~3 mM, which was consistent with most literature reports, and used this concentration to calculate the absolute concentrations of PCr and Pi. However, it should be possible to achieve absolute quantification of the ATP concentration in the brain using an external reference with a calibrated phantom solution. Therefore, we could experimentally determine all four metabolic fluxes that define the entire kinetic network of PCr↔ ATP ↔ Pi, as illustrated by Fig. 5-1. These advantages make the MSS MT approach more efficient and straightforward, especially for measuring the reverse rate constants and

fluxes of the CK and ATPase reactions and assessing the entire metabolic network of PCr↔ ATP ↔ Pi *in vivo*.

5.5.5 Further Simplification of the MT Approach to Study the PCr↔ ATP ↔ Pi Chemical Exchange System *In Vivo*: Supportive Evidence

One interesting conclusion from this study is that *in vivo* measurements of the PCr↔ ATP ↔ Pi kinetic network and metabolic fluxes in the brain may be simpler to obtain than was previously thought, for the following reasons:

The extracellular Pi does not directly participate in the ATPase reaction, which occurs in the intracellular compartment. Therefore, the PCr↔ ATP ↔ Pi chemical exchange system can be treated as a single intracellularcompartment system, and only the intracellular Pi concentration is needed to quantify the forward ATPase flux (Ff^{ATPase}) as reported in this study. Otherwise, Ff^{ATPase} may be slightly overestimated if the extracellular Pi NMR signal is not completely excluded in the calculation according to Eq. [5-2e] [65].

The results from this study show that the forward and reverse fluxes measured by the MSS MT approach satisfied the chemical equilibrium condition for both the CK and ATPase reactions. They reveal that the previous concerns about the possible NMR invisibility of high-energy phosphate (HEP) metabolites, and potential complications from different subcellular HEP compartment contributions and/or energy transfer among these compartments [89, 104, 105] may not be crucial factors in determining the CK and

ATPase reverse fluxes in the human brain by using the MSS MT approach. In other words, our results suggest that all three relevant phosphate metabolites of PCr, γ-ATP, and Pi in the human brain are detectable by *in vivo* ^{31}P MRS, and they can be treated as a single cellular pool to determine the kinetic network of the PCr↔ ATP ↔ Pi exchange system using the *in vivo* ^{31}P MSS MT approach. However, these metabolites can physically locate in different subcellular compartments (e.g., the cytosol and mitochondria). Eliminating these concerns and complications would significantly simplify the *in vivo* ^{31}P MRS approach for studying the kinetic network of cerebral ATP metabolism.

One common technical difficulty faced by *in vivo* ^{31}P MT approaches is the so-called offset RF saturation effect due to the imperfection of the frequency profile given by an RF saturation pulse (or pulse train). In principle, two control spectra in the presence of the same RF saturation are required to correct for the offset RF saturation effect and quantify the true MT effects on the two coupled PCr and Pi spins, for instance, when γ-ATP is fully saturated in the steady-state condition. When these control spectra are acquired, the RF saturation pulse will be applied at the opposite side of the coupled spin (e.g., PCr), but with the same chemical shift difference related to the γ-ATP spin. Therefore, a total of six control spectra and three saturated spectra are needed to obtain accurate measurements of the PCr↔ ATP ↔ Pi kinetic network using the MSS MT approach. This requirement can significantly increase the total measurement time and reduce the measurement efficiency. In this study we applied the BISTRO saturation

scheme with an improved saturation profile [111]. We compared the results obtained by 1) using a single control spectrum acquired in the absence of RF saturation and without the offset saturation correction, and 2) correcting the offset saturation effects for all spectra used in the calculation (see Materials and Methods). The comparison results are summarized in Table 5-1. The differences of the results from two methods are within 1 SD for all measured parameters. Therefore, the offset RF saturation effect by the BISTRO saturation scheme is negligible, and only one control spectrum acquired in the absence of the RF saturation is required for the MSS MT measurement. Overall, only one control and three fully saturated ^{31}P spectra are needed to determine all forward and reverse rate constants and fluxes of the PCr↔ ATP ↔ Pi chemical exchange system in the brain. In addition to these kinetic parameters, the apparent spin-lattice relaxation time of γ-ATP can also be derived from the four spectra, as discussed above.

	MT Experiment			
	Sat (PCr)[c]	Sat (P_i)[c]	Sat (γ-ATP)	Sat (PCr and Pi)
Subject number	$N = 16$	$N = 16$	$N = 11$	$N = 7$
M^{*o}/M^0 *of PCr*	—	0.94 (0.91[d]) ± 0.04	0.41 (0.39) ± 0.02	—
M^{*o}/M^0 *of γ-ATP*	0.64 (0.60) ± 0.02	0.88 (0.88) ± 0.04	—	0.55 ± 0.03
M^{*o}/M^0 *of Pi*	0.79 (0.76) ± 0.05	—	0.65 (0.64) ± 0.04	—
Rate constant (s^{-1})	$k_2 = k_r^{ATP\rightarrow Pi} = 0.05\ (0.05) \pm 0.01$[a] $k_{-1} = k_r^{ATP\rightarrow PCr} = 0.59\ (0.62) \pm 0.06$[b]	$k_{-1} = k_r^{ATP\rightarrow PCr} = 0.42\ (0.47) \pm 0.05$[a] $k_2 = k_r^{ATP\rightarrow Pi} = 0.11\ (0.11) \pm 0.03$[b]	$k_1 = k_f^{PCr\rightarrow ATP} = 0.30\ (0.33) \pm 0.04$[a] $k_{-2} = k_f^{Pi\rightarrow ATP} = 0.18\ (0.18) \pm 0.05$[a]	
$T_1(s)$	$T_1^{app}(\gamma\text{-}ATP) = 0.71\ (0.68) \pm 0.07$[a]	$T_1^{int}\ (\gamma\text{-}ATP) = 1.35\ (1.32) \pm 0.17$[a]	$T_1^{app}\ (PCr) = 1.97\ (1.85) \pm 0.20$[a] $T_1^{int}\ (PCr) = 4.89\ (4.86) \pm 0.54$[a]	$T_1^{app}\ (\gamma\text{-}ATP) = 0.66 \pm 0.12$
$T_1(s)$	$T_1^{app}\ (\gamma\text{-}ATP) = 0.61\ (0.64) \pm 0.15$[b] $T_1^{int}\ (\gamma\text{-}ATP) = 0.94\ (1.05) \pm 0.27$[b]	$T_1^{app}\ (\gamma\text{-}ATP) = 1.24\ (1.24) \pm 0.25$[b] $T_1^{int}\ (\gamma\text{-}ATP) = 1.43\ (1.44) \pm 0.32$[b]	$T_1^{app}\ (Pi) = 2.24\ (2.24) \pm 0.32$[a] $T_1^{int}\ (Pi) = 3.77\ (3.77) \pm 0.53$[a]	
Flux ratio	$\frac{F_f^{CK}}{F_r^{CK}} = 0.95\ (0.93) \pm 0.12$[a] $\frac{F_f^{CK}}{F_r^{CK}} = 0.67\ (0.71) \pm 0.13$[b]	$\frac{F_f^{ATP_{ase}}}{F_r^{ATP_{ase}}} = 1.08\ (1.08) \pm 0.21$[a] $\frac{F_f^{ATP_{ase}}}{F_r^{ATP_{ase}}} = 0.49\ (0.49) \pm 0.15$[b]		

Table 5-1 Results of magnetization saturation transfer measurements in human brain

a Obtained using the MSS MT approach based on the three-spin exchange model.

b Obtained using the conventional saturation transfer approach based on the two-spin exchange model. The results were averaged from nine subjects' data as shown in Fig. 5-5.

c From the experiments conducted using the same subjects.

d All data shown in parentheses were obtained using the control ^{31}P spectra without the correction of the offset saturation effect.

The PCr↔ ATP ↔ Pi chemical exchange reactions in a biological organ are likely in chemical equilibrium (or near equilibrium) for most biomedical applications (e.g., the resting human brain, as investigated in this study). As long as the equilibrium (or near equilibrium) condition is satisfied, one can further simplify the *in vivo* ^{31}P MT measurement procedure using the following equal-flux relations:

$$k_{-1} = k_1[PCr]/[ATP]$$
$$k_2 = k_{-2}[Pi]/[ATP] \qquad [5-6]$$

In principle, only two *in vivo* ^{31}P spectra (one control and one with full saturation of γ-ATP) are required to determine all forward rate constants and fluxes according to Eqs. [5-2c]–[5-2e], and to then calculate the reverse rate constants of k_{-1} and k_2 according to Eq. [5-6]. Thus, it is possible to rapidly determine these kinetic parameters under different physiological and/or pathological conditions using the *in vivo* ^{31}P MT approach.

To achieve maximal ^{31}P NMR detection sensitivity for testing and validating the proposed MSS MT approach, we defined the spatial localization of *in vivo* ^{31}P spectra from the human occipital lobe by the local sensitivity (or B_1) profile of the ^{31}P surface coil. The high sensitivity was crucial for reliably detecting the small Pi resonance peak and its change, particularly during the progressive saturation experiments. Our previous study demonstrated that the *in vivo* ^{31}P MRS signal detected by the same ^{31}P RF coil configuration was mainly attributable to brain tissue from the human occipital lobe, with negligible contamination from the surrounding extracranial skeletal muscles [35]. The average integral ratio of PCr/γ-ATP = 1.33 + 0.14 obtained from the fully-relaxed control ^{31}P spectra in this study is in agreement with the previously reported ratio of approximately 1.2 measured from the human occipital lobe with a 3D chemical shift imaging (CSI) approach. This ratio is much lower than that of extracranial skeletal muscle (≈ 3) [71]. Therefore, the HEP metabolites and kinetic parameters determined by *in vivo* ^{31}P MRS in this study were contributed mainly by brain tissue in the human occipital lobe.

Finally, the simplified MSS MT approach with minimal required steady-state saturated ^{31}P spectra can be implemented with 3D CSI. This allows one to spatially map the spatial heterogeneous distribution of ATP metabolism in the brain, especially at high fields, because of a significant gain in NMR detection sensitivity and improved spectral resolution.

5.6 Conclusions

An *in vivo* ^{31}P MT approach based on multiple single-site saturation measurements was developed to noninvasively determine all rate constants in the PCr↔ ATP ↔ Pi kinetic network and four associated ATP metabolic fluxes in the human brain. The quantification used in this approach is based on solving multiple Bloch equations that account for all three exchangeable phosphate metabolites (or spins). Our results indicate that one must treat the PCr ↔ ATP ↔ Pi chemical exchange reactions as a three-spin exchange system to accurately determine the reverse rate constants and reverse fluxes for both the CK and ATPase reactions. The ratios of forward and reverse fluxes measured in the human occipital lobe using the MSS MT approach satisfied the chemical equilibrium condition. The MSS MT approach only requires one control and three saturated ^{31}P spectra to determine all kinetic parameters involved in the PCr↔ ATP ↔ Pi kinetic network. This noninvasive approach should provide an important neuroimaging modality for quantitatively studying the fundamental ATP metabolism and its impact on cerebral bioenergetics associated with brain function and brain activation.

In addition, our results reveal that the forward ATPase flux determined by the *in vivo* ^{31}P MT approach equals the oxidative phosphorylation rate. At normal physiological conditions, the ATP synthesis rate is tightly coupled to the oxygen metabolism rate in the brain. However, such coupling may break down in pathological conditions. For instance, damage to the mitochondrial DNA in neurons has been implicated in both Parkinson's disease and Alzheimer's disease. Also, some of the mitochondrial DNA mutations found

in Alzheimer's disease patients have been associated with defects in oxidative phosphorylation in mitochondria [118]. Thus, the *in vivo* ^{31}P MT approach may play an important role in studying a variety of neurodegenerative diseases associated with mitochondrial abnormalities and metabolic syndrome.

5.7 Acknowlegdements

The authors gratefully acknowledge Dr. Peter Andersen for technical assistance, and Dr. Kamil Ugurbil for insightful discussion and support.

Published by Fei Du, Xiaohong Zhu, Hongyan Qiao, Xiaoliang Zhang, and Wei Chen in journal of Magnetic Resonance in Medicine 2007.

6. KINETIC NETWORK OF ATP METABOLISM IN HUMAN BRAIN (II)

^{31}P MRS combined with magnetization saturation transfer (ST) or inversion transfer (IT) approaches are widely used for *in vivo* studies of creatine kinase (CK) and ATPase reactions. However, both ST and IT approaches are mainly based on the approximation of two-site chemical exchange model and the validity of this approximation for brain application is still elusive. In the present study, we used the three-site chemical exchange model and full matrix relaxation analysis approach to process IT experimental data and furthermore compared the IT results with that measured by the multiple single-site saturation (MSS) transfer method. Several conclusions are drawn from this study. Firstly, although each magnetization inversion recovery curve of PCr, γ-ATP or Pi contains the information of chemical exchanges, the sensitivity of curve regression for measuring kinetic parameters is substantially different. The simulations of curve fitting sensitivity provide optimal strategies for improving the measurement reliability using the IT approach. Secondly, for the IT experiments the two-site chemical exchange model provides a fair approximation to determine the kinetic parameters for the CK reaction, but the ATPase reaction must be treated by the three-site chemical exchange model. Thirdly, the subcellular compartments might not be a concern for determining the chemical exchange kinetics among PCr, ATP and Pi for both ST and IT experiments. Lastly, the MSS transfer approach is more efficient and robust for measuring high energy phosphate metabolism compared to the IT method. The present study should be crucial for establishing an optimal *in vivo* ^{31}P MRS method for studying brain bioenergetics at various physiological or pathological conditions and clarifies some conflicted results in the literatures.

6.1 Introduction

The chemical reactions among high energy phosphates: adenosine-5'-triphosphate (ATP) and inorganic phosphate (Pi); as well as between ATP and phosphocreatine (PCr) are essential to brain function. ATP is mainly produced through oxidative phosphorylation [88], i.e. the forward chemical reaction of ADP+Pi→ATP, which can be found in every cell of every organ for supporting a variety of cellular activity. However, it is perhaps "hardest at work" inside of brain because although brain only accounts to 2% weight of whole body, it consumes approximately 20% of the total oxygen for constant and high demand of energy. The majority of ATP utilization in the brain, which achieves through ATP hydrolysis to Pi, i.e., the reverse chemical reaction of ATP→ADP+Pi, is to restore transmembrane iron gradients therefore keeping electrophysiological activity and cell signaling in the brain. At mean time, ATP metabolism is tightly linked to PCr metabolism by the reversible creatine kinase (CK) reactions governed by the chemical reaction among PCr and ATP (PCr↔ATP) [86]. CK has been suggested to play a key role in the energy transfer from the sites of ATP generation (inside of mitochondria) to the sites of utilization (inside of cytosol) by a "PCr-Cr (creatine)-CK shuttle" as an energy carrier and transporter thereby maintaining a constant ATP level in the living cell. Therefore, these coupled chemical exchange reactions (PCr↔ATP↔Pi) are critical for regulating ATP metabolism and tightly correlate to the energy generation, utilization and transportation. One particularly interesting question is how to accurately determine the chemical kinetics of these fundamental chemical reactions *in vivo*. The solution to this

question should be essential for understanding high-energy phosphate metabolism and bioenergetics associated with brain function and dysfunction.

^{31}Phosphorus magnetic resonance spectroscopy (^{31}P MRS) offers the unique capability to measure kinetic parameters using magnetization transfer approach, especially as a noninvasive tool for *in vivo* studies besides commonly measuring the concentrations of phosphorylated compounds, free magnesium and intracellular pH [89, 119]. In principle, the above mentioned chemical exchange reactions constitute a three-site chemically coupled spin system (i.e. PCr↔γ-ATP↔Pi), and in principle can be determined by ^{31}P magnetization transfer measurement. Several ^{31}P magnetization transfer methods have been proposed, among them saturation transfer (ST) [91, 120] and inversion transfer (IT) [109] are intensively used particularly for the CK reaction studies. However, in the majority of previous studies, ST or IT approach was based on the two-site chemical exchange model in which the CK reaction was simply treated as a two-site chemical exchange system (i.e. PCr↔ATP) and the ATPase reaction (i.e. ATP↔Pi) was neglected because of the low sensitivity of Pi especially at the low-field MRI scanner. This simple two-site model approximation has raised some concerns regarding the accuracy for measuring the unidirectional forward (PCr→ATP) and reserve (PCr←ATP) chemical exchange fluxes (F_f and F_r) because it led to some conflicted results: equality [109] versus inequality of F_f and F_r for CK reaction [98]. These conflicting results disobey the fundamental nature law: the fluxes of CK reaction in and out of PCr pool must be equal under the steady-state equilibrium condition. One of the debates is that CK

reaction should be treated as a three-site chemical exchange system. Subcellular compartments are also proposed to interpret erroneous estimations of the CK fluxes. Although ATP and PCr chemically exist in the different cellular compartments, the NMR signals are overlapped. It has been suggested that some ATP or PCr might not fully participate in the CK reaction or it has significant different kinetics [104, 105]. Significant efforts have been attributed to address these issues, which however are still not resolved [39].

Recently we have developed an improved magnetization ST method named as the multiple single-site saturation (MSS) transfer approach based on the three-site chemical exchange model (PCr↔ATP↔Pi) for measuring all the chemical exchange rate constants and fluxes among PCr, ATP and Pi [121]. Our results based on the measurement of the occipital lob of human brain have illustrated that chemical reactions of PCr↔ATP↔Pi must be treated as a three-site chemical exchange system for ST experiments to accurately determine the reverse rate constants and fluxes for the CK and ATPase reactions; and the measured forward and reverse fluxes are satisfied the chemical equilibrium condition for both CK and ATPase chemical reactions [121]. In contrast, if the chemical reaction of CK or ATPase was treated as the two-site chemical exchange system, the measured forward and reverse fluxes were not equal for both CK and ATPase reactions if the same experimental data were used.

However, there are still some arguments about the MSS transfer approach. The key argument is that the ST experiment might be insensitive to subcellular compartmental

reactions especially for the steady-state saturation transfer measurement [98]. Another argument is that MSS transfer measurement is based on the global chemical exchange model, which is too simple to detect the kinetic parameters among PCr and ATP in the subcellular compartments. Generally the dynamic chemical exchange rate constants and fluxes of CK and ATPase reaction also can be deduced using IT approach. Therefore, the purpose of the present study is to address the following questions:

1. Whether the simple global three-site chemical exchange model (PCr↔ATP↔Pi) is suitable for describing and determining the chemical exchange network among PCr, ATP and Pi in the brain using the IT approach compared to the MSS approach?

2. Whether CK reaction can be treated as a two-site chemical exchange model for IT experiments? In other words, whether inequality of forward and reverse fluxes of CK reaction deduced by the IT approach in the literatures is caused by the approximation of two-site chemical exchange model?

3. For the MSS transfer and IT approaches, which of them is more robust and efficient to accurately measure chemical exchange fluxes of CK and ATPase reactions in the brain?

To answer these questions, we have performed *in vivo* ^{31}P magnetization IT experiments in the human brain at 7T by taken significant benefit of increased sensitivity and spectral resolution. The two-site and three-site chemical exchange model were

applied to determine the kinetic parameters of chemical reactions of CK and ATPase. We compared the IT measurement results with that deduced by the MSS transfer method. The effect of ATPase reaction on the CK reaction processed by IT approach with the two-site chemical exchange model was also tested and discussed.

6.2 Theory

We have previously demonstrated that extracellular Pi doesn't involve the chemical exchange between Pi and ATP, only does intracellular Pi (defined as Pi herein) [121]. Although PCr, ATP and Pi chemically exist in the subcellular compartments [122, 123], the global three-site chemical exchange model was applied. For the simplicity of mathematic derivation, PCr, ATP and Pi are noted as a, b and c, respectively. The Bloch equations of a, b, c accounting for chemical exchange effects are given as the following [120]:

$$\underset{a}{PCr} \underset{K-1}{\overset{K1}{\Longleftrightarrow}} \gamma - \underset{b}{ATP} \underset{K2}{\overset{K-2}{\Longleftrightarrow}} \underset{c}{Pi}$$

$$\frac{dMa}{dt} = -\frac{(Ma - Ma^0)}{T_{1a}} - k_1 M_a + k_{-1} M_b \qquad [6-1a]$$

$$\frac{dMb}{dt} = -\frac{(Mb - Mb^0)}{T_{1b}} - k_{-1} M_b - k_2 M_b + k_1 M_a + k_{-2} M_c \qquad [6-1b]$$

$$\frac{dMc}{dt} = -\frac{(Mc - Mc^0)}{T_{1c}} - k_{-2} M_c + k_2 M_b \qquad [6-1c]$$

The equation solutions for the ST approach had been deduced before [121]. If

both chemical reactions of CK and ATPase are at equilibrium, then,

$$\begin{aligned} k_1[PCr] &= k_{-1}[ATP] \\ k_2[ATP] &= k_{-2}[Pi] \end{aligned} \qquad [6\text{-}2]$$

The Bloch equations for the IT approach can be written in a matrix form [40] and yields the following differential equation matrix (where t is the inversion recovery time):

$$\frac{\partial \vec{M}(t)}{\partial t} = A[\vec{M}(t) - \vec{M}^0] \qquad [6-3a]$$

$$A = \begin{Bmatrix} -(T_{1a}^{-1} + k_1) & k_{-1} & 0 \\ k_1 & -(T_{1b}^{-1} + k_{-1} + k_2) & k_{-2} \\ 0 & k_2 & -(T_{1c}^{-1} + k_{-2}) \end{Bmatrix} \qquad [6-3b]$$

$$\begin{aligned} \alpha_a &= k_1 + \frac{1}{T_{1a}} \\ \alpha_b &= k_{-1} + k_2 + \frac{1}{T_{1b}} \\ \alpha_c &= k_{-2} + \frac{1}{T_{1c}} \end{aligned} \qquad [6-3c]$$

α_a, α_b and α_c are the apparent longitudinal relaxation rates of PCr, γ-ATP and Pi, respectively. $\vec{M}$ is a magnetization vector, in which three components are equal to the longitudinal magnetizations of PCr, γ-ATP and Pi, respectively. $\vec{M}^0 = \vec{M}(t = \infty)$ is the longitudinal magnetization vector at thermal equilibrium. T_1 and k are the intrinsic longitudinal relaxation times and pseudo first-order chemical exchange rate constants. The solution of Equation [6-3a] is:

$$\vec{M}(t) = (I - e^{tA})\vec{M}^{0} + e^{tA}\vec{M}(0) \qquad [6\text{-}3d]$$

In Equation [6-3d], I is a 3×3 unity matrix and $\vec{M}(0)$ is magnetization vector at the initial condition at t=0 in Equation [6-3a]. It is difficult to expand Equation [6-3d] as simple expressions to describe the magnetization recovery of each component depending on the inversion recovery time because the index of exponent is a matrix, nevertheless it can be numerically simulated by mathematic regression approaches [124, 125]. In principle, Equation [6-3d] is a general solution to the IT approach, for instance, even in the case of simultaneously inverting all three chemically coupled spins. All seven kinetic parameters including three intrinsic longitudinal relaxation times and four pseudo first-order chemical exchange rate constants could be deduced from the magnetization inversion recovery time courses of three components by curve fitting of Equation [6-3d].

In the present study, only magnetization of PCr or γ-ATP was selectively inverted and investigated. Equation [6-3d] also can be applied to the two-site chemical exchange system. For example, it can be used for CK reaction when ATPase reaction is ignored with $k_{\pm 2}$=0. However, for two-site chemical exchange system, the time-dependent behaviors of magnetizations during the recovery can be described by the complete solutions of the Bloch equations as the following [109]:

$$M^i(t) = M^i(\infty) + c_1 \exp(\lambda_+ t) + c_2 \exp(\lambda_- t) \qquad [6\text{-}4a]$$

$$M^u(t) = M^u(\infty) + c_3 \exp(\lambda_+ t) + c_4 \exp(\lambda_- t) \qquad [6\text{-}4b]$$

$$\lambda\pm = 1/2 \cdot \{-(1/t_1^i + 1/t_1^u) \pm [(1/t_1^i + 1/t_1^u)^2 + 4k^{i\to u}k^{u\to i}]^{1/2}\} \qquad [6\text{-}4c]$$

$$c_2 = \{(1/k^{u\to i})[M^i(0) - M^i(\infty)] \times (\lambda_+ + 1/t_1^i) + [M^u(\infty) - M^u(0)]\} / [(\lambda_+ - \lambda_-)(1/k^{u\to i})] \qquad [6\text{-}4d]$$

$$c_1 = M^i(0) - M^i(\infty) - c_2 \qquad [6\text{-}4e]$$

$$c_3 = c_1(\lambda_+ + 1/t_1^i)/k^{u\to i} \qquad [6\text{-}4f]$$

$$c_4 = c_2(\lambda_- + 1/t_1^i)/k^{u\to i} \qquad [6\text{-}4g]$$

where, M_i and M_u are the inverted and undisturbed magnetizations, respectively. $1/t_1{}^i$ and $1/t_1{}^u$ are the apparent longitudinal relaxation rates of the inverted and non-inverted nuclei. For the CK reaction, the time-dependent behaviors of the PCr and γ-ATP signals during an IT experiment are therefore dependent on the four kinetic constants ($1/t_1{}^{\gamma\text{-ATP}}$, $1/t_1{}^{PCr}$, $k^{ATP\to PCr}$ as well as $k^{PCr\to ATP}$). Here, $1/t_1{}^{\gamma\text{-ATP}}$ and $1/t_1{}^{PCr}$ are the apparent longitudinal relaxation rates of γ-ATP and PCr, respectively, and defined by the following equations:

$$1/t_1^{\gamma-ATP} = 1/T_1^{\gamma-ATP} + k^{ATP\to PCr} \qquad [6\text{-}4h]$$

$$1/t_1^{PCr} = 1/T_1^{PCr} + k^{PCR\to ATP} \qquad [6\text{-}4i]$$

The similar strategy can be applied to ATPase reaction between spins of γ-ATP and Pi. Principally one selective inversion recovery experiment can be deduced all kinetic parameters through bi-exponential fitting of Equations [6-4a] and [6-4b]. We used Equations [6-4a] and [6-4b] to process the CK or ATPase reaction as a two-site chemical exchange model and compares the results with that deduced from the three-site chemical exchange model using Equation [6-3d].

6.3 Experiments

Six healthy subjects (3 men and 3 women, 26±5 years old) were recruited for the study. All subjects provided well-informed written-consent, which was approved by the Institutional Review Board at the University of Minnesota. The experiments were performed at a 90-cm bore 7T magnet (Magnex Scientific, Abingdon, UK) with a Varian INOVA console (Varian, Palo Alto, CA). A decoupled dual-coil configuration was used. The linear butterfly-shape ^{1}H surface-coil was applied for anatomical imaging and shimming, which was performed on 3×3×3 cm^3 voxel inside the human occipital lob using FAST-MAP techniques [110]. Another 5-cm-diameter single-loop ^{31}P surface coil to cover the human occipital lob only was used to acquire *in vivo* ^{31}P spectroscopy. No additional special localization strategies were used except that achieved by the surface coil itself. It has been demonstrated that the contribution of surrounding muscle to the brain ^{31}P signal was less than 10% [65].

In vivo ^{31}P spectra were acquired with the 200 μs hard pulse for spin excitation and an adiabatic hyperbolic Sech pulse (50 ms pulse width, 180-Hz inversion bandwidth) for selective inversion of PCr or γ-ATP resonance. Spoiling gradients (4 ms) were immediately applied in three dimensions after the inversion adiabatic pulse for suppressing all the transverse magnetization. For all ^{31}P spectra, a long (16 s) delay between the end of FID acquisition to the inversion adiabatic pulse was used to keep spins full relaxation. Other acquisition parameters were: 5000 Hz spectral width, 1024 FID data points and 32 scans for signal averaging. Eight inversion recovery time points

were selected and varied from 40 ms to 12 s, resulting in a total sampling time of ~ 1 hour. The resonance peak integrals of PCr, γ-ATP and Pi were quantified by using the curve fitting based on the AMARES method in the MRUI software package [126]. All the magnetizations of PCr, γ-ATP and Pi including the recovered magnetization differences predicted by the three-site and two-site chemical exchange models were reported as the normalized values (relative to PCr magnetization at thermal equilibrium condition except the cases with special notation).

The software for simulations and curve fitting with least-square regression algorithm for chemical exchange studies was developed in our laboratory using MATLAB language (The MathWorks, Inc., Natick, MA).

The results are presented by mean±standard deviation from 6 subjects.

6.4 Results

6.4.1 ^{31}P MRS with Selective Inversion of PCr and γ-ATP, Respectively

Figure 6-1 illustrates the *in vivo* human brain ^{31}P spectra acquired in the presence of selective inversion of (a) PCr and (b) γ-ATP, respectively, with varied inversion recovery times. The magnetizations of chemically coupled spins are presented in Table 6-1, in which the magnetizations at t = 0, i.e., the initial magnetizations in Equations [6-3d], [6-4a] and [6-4b] were obtained from linear aggression of first three data points (see Table 6-1) in the IT measurements [102]. All the data in Table 6-1 plus previously

measured magnetizations at thermal equilibrium (1.00, 0.75, and 0.23 for PCr, γ-ATP and Pi, respectively) [121] were used for curve fitting and simulation of magnetization recovery dependence on each kinetic parameter of interest.

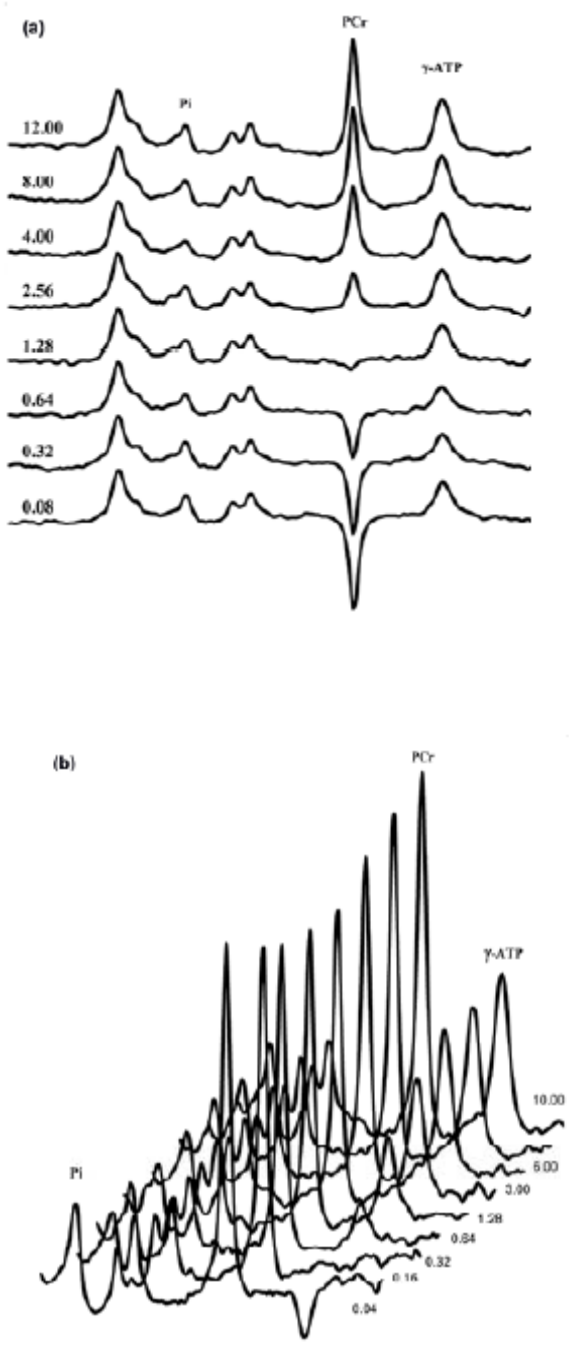

Figure 6-1 *In vivo* ^{31}P spectra in the presence of selective inversion of (a) PCr (a) or (b) γ-ATP with varied inversion recovery times (s) acquired from a representative volunteer.

Inversion of PCr				Inversion of γ-ATP			
t (s)	**PCr**	**γ-ATP**	**Pi**	**t (s)**	**PCr**	**γ-ATP**	**Pi**
*0	-0.95	0.53	0.23	*0	0.92	-0.24	0.23
0.08	-0.912±0.032	0.491±0.023	0.234±0.081	0.04	0.905±0.063	-0.207±0.009	0.228±0.092
0.32	-0.634±0.029	0.473±0.058	0.214±0.092	0.16	0.867±0.041	-0.027±0.010	0.225±0.061
0.64	-0.413±0.006	0.452±0.061	0.222±0.098	0.32	0.825±0.052	0.132±0.057	0.217±0.052
1.28	-0.115±0.010	0.484±0.040	0.214±0.073	0.64	0.807±0.051	0.382±0.030	0.214±0.043
2.56	0.316±0.033	0.562±0.045	0.205±0.066	1.28	0.802±0.008	0.506±0.020	0.206±0.094
4.00	0.662±0.028	0.623±0.034	0.197±0.066	3.00	0.845±0.022	0.628±0.043	0.211±0.085
8.00	0.944±0.071	0.684±0.038	0.222±0.086	6.00	0.942±0.022	0.718±0.051	0.225±0.078
12.00	1.000	0.712±0.037	0.230±0.062	10.00	1.000	0.745±0.010	0.232±0.090

Table 6-1 Normalized magnetizations of chemically coupled spins at the various inversion-recovery times (t) after PCr or γ-ATP was selectively inverted.

Note:

(1) data were presented as mean±SD from 6 healthy subjects

(2) * data were obtained from linear aggression of the first three data points with the short recovery times and indicated that γ-ATP was partially inverted when PCr was selectively inverted and the similar behavior existed for PCr when γ-ATP was selectively inverted.

6.4.2 Simulation of Curve Fit Sensitivity of Kinetic Parameters for IT Experiments with the Three-site Chemical Exchange Model

As mentioned before, Equation [6-3d] predicts the time-dependent behaviors of magnetizations of three chemically coupled spins (PCr, γ-ATP and Pi) after PCr or γ-ATP is selectively inverted. The sensitivity of each kinetic parameter to the curve fitting was simulated according to Equation [6-3d] while other kinetic parameters were fixed to the values taken from the previous MSS transfer measurement results (see Table 6-2). The simulation results are partially presented in Figs. 6-2a and 6-2b, in which the open circles illustrate the averaged experimental data from 6 subjects (see Table 6-1). Therefore, the circles in Figs. 6-2a and 6-2b also indicate the deviations of the experimental data with that predicted by the theoretical IT simulation results in which some parameters were taken from the previous MSS transfer measurement results (see the dotted lines in Fig. 6-2). For the sake of simplicity, error bars of the experimental IT data were ignored in all plots.

Figure 6-2 shows the simulation results of the influences of the variation in k_1 (Fig. 6-2a) and k_{-2} (Fig. 6-2b) on the inversion recovery time courses of PCr, Pi and γ-ATP magnetizations. Moreover, the variations of T_1^{PCr}, $T_1^{\gamma\text{-ATP}}$ or k_{-1} have the similar influences as that of k_1 variation (Fig. 6-2a); and the variations of T_1^{Pi} and k_2 have the similar influences as that of k_{-2} variation (Fig. 6-2b) (data not shown herein).

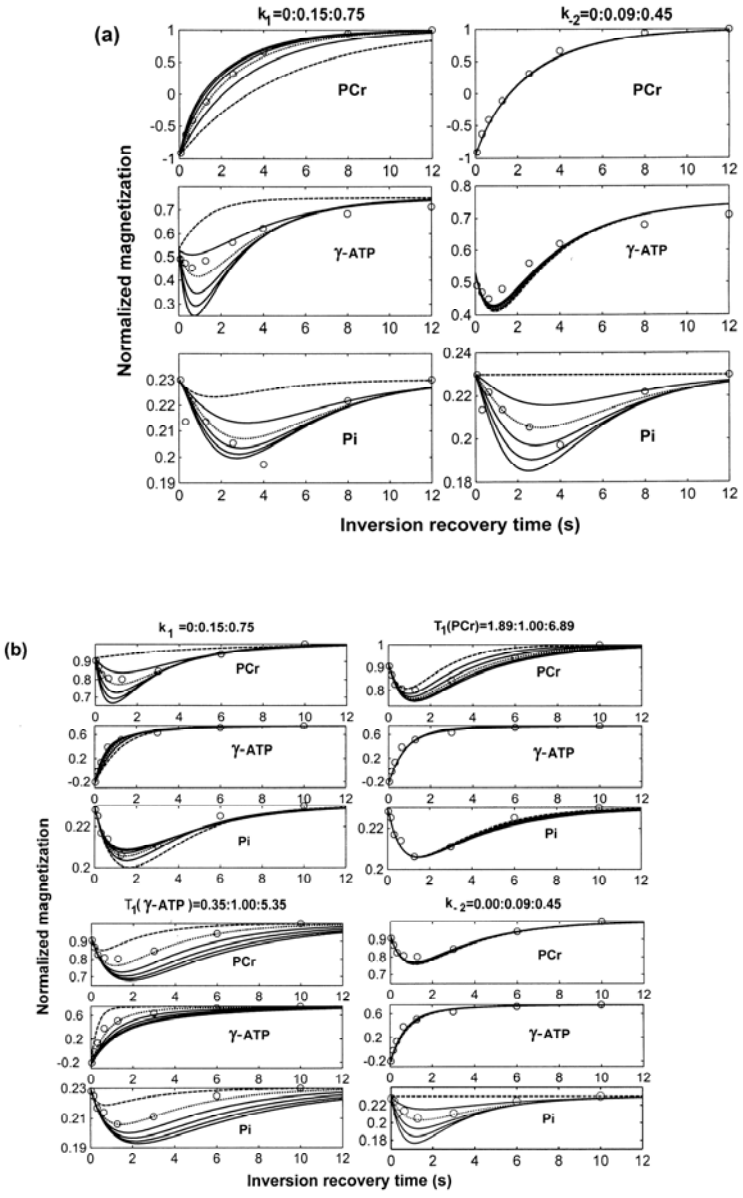

Figure 6-2 Curve fitting sensitivity simulations for the PCr (a) or γ-ATP (b) selective inversion experiments according to Equation [6-3d]. The circles illustrate the averaged experiment data. Kinetic parameters to be simulated were demonstrated on the top of a-paired columns indicated the magnetization recovery of PCr, γ-ATP and Pi, respectively, with the formation of x:y:z. Here x, y and z were the beginning value, step and the end

value, respectively. For the simulations of k_1 and k_{-2}, chemical equilibrium conditions were assumed (i.e. $k_1 \times [PCr] = k_{-1} \times [ATP]$ and $k_2 \times [ATP] = k_{-2} \times [Pi]$). The dashed and dotted lines indicate simulations with the beginning values and with all the values of kinetic parameters as same as that deduced by the MSS transfer approach, respectively.

(a): when PCr was selectively inverted								
Method		Kinetic parameters						
		CK				ATPase		
		T_1^{PCr} (s)	k_1 (s^{-1})	k_{-1} (s^{-1})	$T_1^{\gamma\text{-}ATP}$ (s)	k_{-2} (s^{-1})	k_2 (s^{-1})	T_1^{Pi} (s)
three-site	MSS*	4.89 ±0.54	0.30 ±0.04	0.42 ±0.05	1.35 ±0.17	0.18 ±0.05	0.05 ±0.01	3.77 ±0.53
	IT^{5p}	4.68±1.23	0.26 ±0.08		1.20 ±0.30	0.45 ±0.13		5.76 ±0.23
	IT^{4p}		0.31 ±0.08	0.33 ±0.27		0.51 ±0.25	0.25 ±0.11	
	$IT^{CK\text{-}3p}$	4.38±1.27	0.29 ±0.06		1.23 ±0.22			
	$IT^{ATPase\text{-}2p}$					0.21±0.03		4.48±0.35
two-site	$IT^{CK\text{-}4p}$	3.61±0.77	0.27±0.06	0.59±0.05	1.25±0.32			
	$IT^{CK\text{-}3p}$	4.44±1.27	0.28±0.09		1.01±0.20			
(b): when γ-ATP was selectively inverted								
three-site	IT^{5p}	4.77±0.80	0.33 ±0.05		1.16±0.13	0.34 ±0.08		4.52±0.70
	IT^{4p}		0.55±0.12	0.56±0.21		0.79±0.18	0.17±0.10	
	$IT^{CK\text{-}3p}$	4.90±0.90	0.32 ±0.05		1.10±0.20			
	$IT^{ATPase\text{-}2p}$					0.19± 0.04		2.24±0.44
two-site	$IT^{CK\text{-}4p}$	6.40±0.58	0.58±0.17	0.55±0.18	0.94±0.05			
	$IT^{CK\text{-}3p}$	4.33±1.18	0.33±0.07		1.15±0.29			

Table 6-2 Kinetic parameters determined by the curve fittings using the three-site and two-site chemical exchange models, respectively.

Note:

(1) * The values of kinetic parameters were obtained by the MSS transfer method.

(2) ^{np} (n=2 …5) indicates the numbers of independent kinetic parameters used

for the curve fitting.

(3) For the curve fitting, chemical equilibrium conditions were assumed except of $IT^{CK\text{-}4p}$ and IT^{4p}.

(4) In the three-site chemical exchange model, except of fitted parameters, the other kinetic parameters were fixed and came from MSS transfer results.

(5) Three magnetization recovery time courses were fitted for IT^{5p} and IT^{4p}. Two-curve fitting of magnetization recovery of PCr and γ-ATP were performed for $IT^{CK\text{-}3p}$ and $IT^{CK\text{-}4p}$. And one curve fitting of Pi magnetization were performed for $IT^{ATPase\text{-}2p}$.

6.4.3 Magnetization Recovery Behaviors and Differences Predicted by the Three-site and Two-site Chemical Exchange Model

In this section, we simulated the magnetization recovery behaviors and differences at a given recovery time when chemical reactions of CK and ATPase were treated as the three-site chemical exchange model compared to the two-site chemical exchange model using the known kinetic parameters deduced from MSS transfer experiments. The purpose of this comparison is to test: whether CK reaction can be treated as a two-site chemical exchange model; and whether the unequal chemical exchange fluxes of CK reaction deduced by the two-site chemical exchange model in the previous literatures is due to the neglecting of ATPase reaction.

For the CK reaction, the magnetization recovery behaviors of PCr and γ-ATP were simulated using the three-site and two-site model, respectively, when the PCr resonance was selectively inverted (Fig. 6-3a) or the γ-ATP resonance was inverted (Fig. 6-4a). And the differences of the predicted magnetizations between these two models are also displayed in the figure panels. The simulation results applied to the ATPase reaction are illustrated by Fig. 6-3b (when PCr was selectively inverted) and Fig. 6-4b (when γ-ATP was selectively inverted). Figure 6-5 shows the influences of some kinetic parameters on the magnetization recovery differences between the simulated results treated as the three-site versus two-site chemical exchange model.

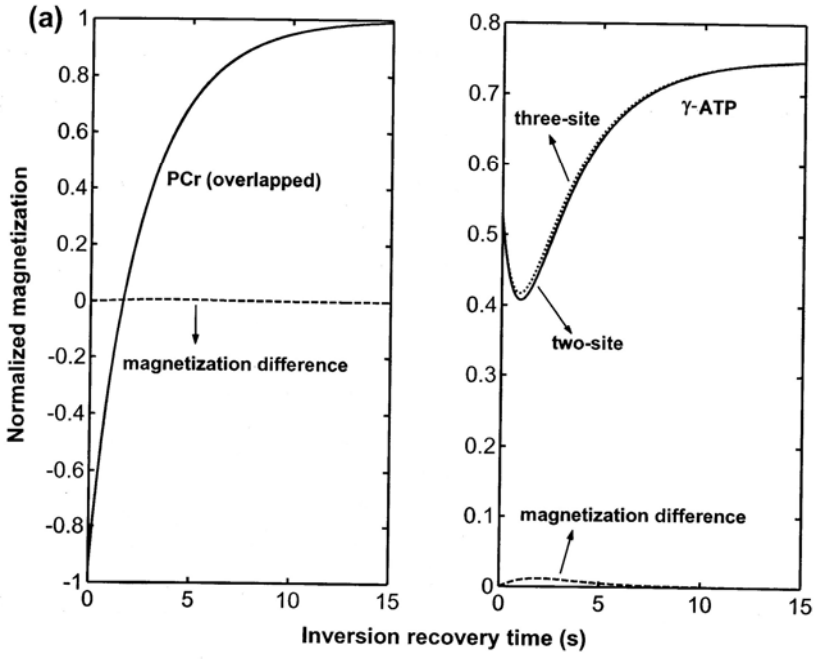

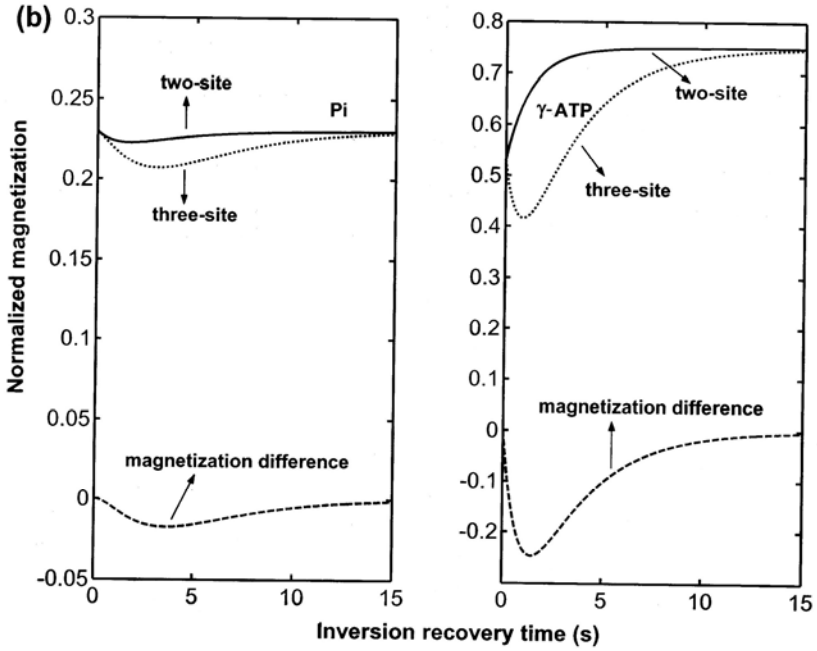

Figure 6-3 Magnetization recovery behaviors and differences predicted by the three-site and two-site chemical exchange model for PCr selectively inverted. Plots (a) and (b) are for CK and ATPase reaction, respectively. The solid and dotted lines were obtained by the two-site and three-site chemical exchange model, respectively. The dashed lines illustrate the magnetization recovery differences between chemical reactions were treated by the three-site and two-site chemical exchange model. The similar strategies have been applied in Figure 6-4.

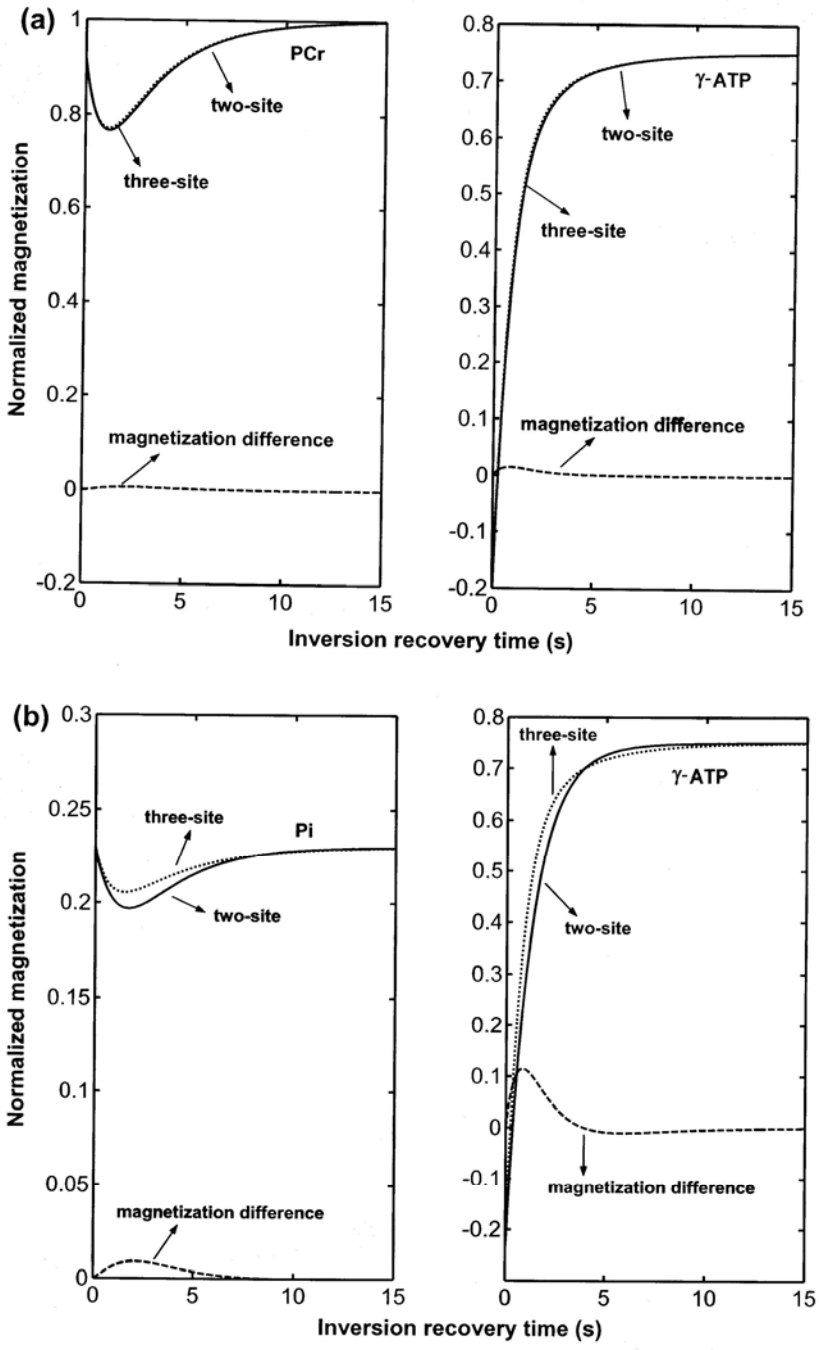

Figure 6-4 Magnetization recovery behaviors and differences predicted by the three-site and two-site chemical exchange model for γ-ATP selectively inverted. Plots (a) and (b)

are for CK and ATPase reaction, respectively.

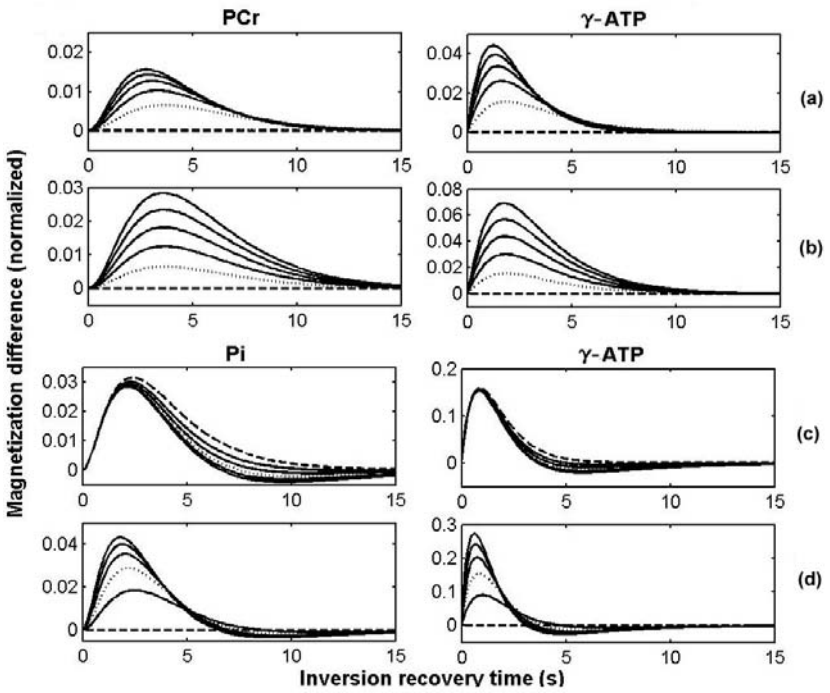

Figure 6-5 Effects of some kinetic parameters on the magnetization recovery differences between chemical reactions were treated by the three-site and two-site chemical exchange model. The panels of (a) (k_{-2}=0: 0.18: 0.90 s^{-1}) and (b) ([Pi] =0: 0.23: 1.15) are for the CK reaction with PCr selective inverted. The panels of (c) (T_1^{PCr}=1.89: 1.00: 6.89 s) and (d) (k_1=0: 0.15: 0.75 s^{-1}) are for ATPase reaction with γ-ATP selective inverted. The magnetization recovery differences were normalized to each component's magnetization at thermal equilibrium, respectively. The dashed and dotted lines have the same meanings as that in Fig. 6-2.

6.4.4 Kinetic Parameters Deduced by the Curve Fitting Using the Three-site or Two-site Chemical Exchange Model, Respectively.

The typical curve fitting result using the three-site chemical exchange model is presented in Fig. 6-6. Table 6-2 summarizes the kinetic parameters obtained through curve fitting with the different constraints.

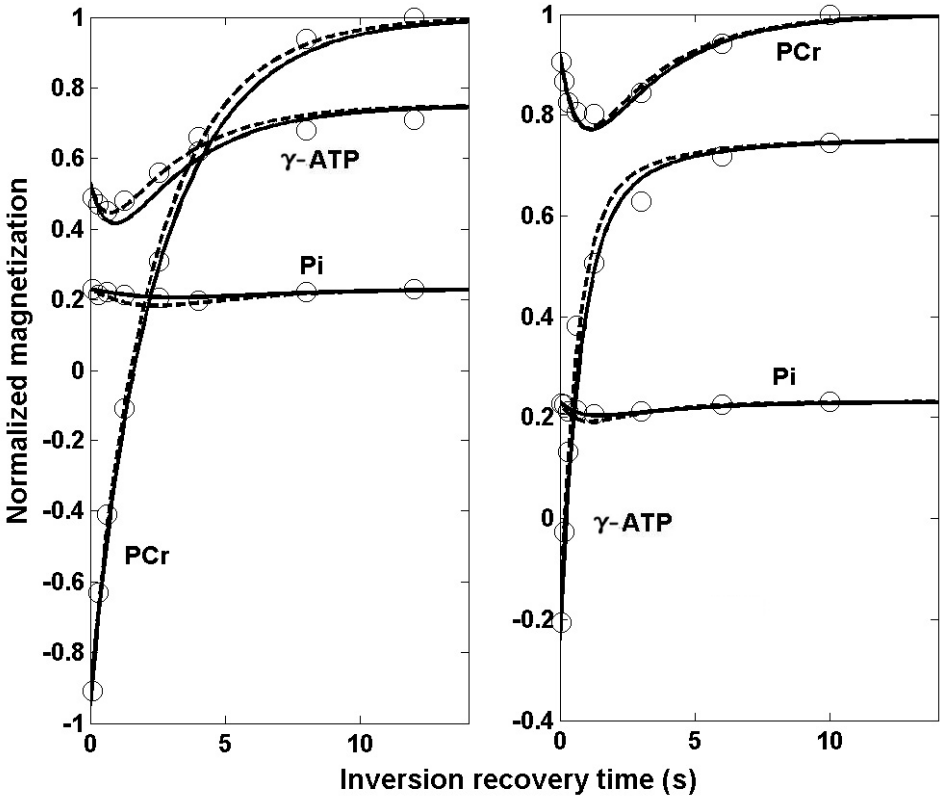

Figure 6-6 Curve fitting results using the three-site chemical exchange model (left: inversion of PCr; right: inversion of γ-ATP). Chemical balance conditions were assumed

for both CK and ATPase reactions, thus, only five free kinetic parameters were fitted. The straight lines were obtained from the values deduced by the MSS transfer approach and the dashed lines were the best fitting results. The circles present the averaged experiment data.

6.5 Discussion

6.5.1 The Curve Regression Sensitivity of ^{31}P Magnetization IT Approach

The magnetization ratios of PCr, γ-ATP and Pi have been measured in the previous MSS transfer studies as 1: 0.75: 0.23 at thermal equilibrium conditions [121]. Current measurements (see Table 6-1) are good agreement with the previous work. When PCr or γ-ATP is selectively inverted, the magnetizations of the other two coupled spins are modulated by the inversion recovery time. It is clearly reflected by the ^{31}P MRS measurements and theoretical simulations. So the IT measurements further suggest that PCr, γ-ATP and Pi constitute a three-site chemically coupled spin system as same as indicated by the MSS transfer approach [121]. In Figure 6-2a, for the curve fitting sensitivity simulations of k_1, forward chemical exchange rate constant of CK reaction, the dashed line of PCr reflects the isolated magnetization's recovery without chemical exchange (k_1=0). With the increase of chemical exchange rate of CK reaction, the magnetization recovery of PCr becomes faster accompanied with a dip of magnetizations of γ-ATP and Pi. It demonstrates that the chemical exchange rates of CK how to affect

the magnetization recovery behaviors. Obviously each line of magnetizations of PCr, γ-ATP and Pi contains the information of chemical exchange of CK and ATPase, but the sensitivity of curve fitting to each kinetic parameter is substantially different as illustrated in Figure 6-2. For PCr selective inversion experiments, the curves of PCr, γ-ATP and Pi are much more sensitive to the variance of dynamical parameters of CK reaction (intrinsic T_1s of PCr and γ-ATP as well as $k_{\pm 1}$), while the curves of PCr and γ-ATP are not sensitive to $k_{\pm 2}$ of ATPase reaction and T_1^{Pi}, which are mainly determined by the time course of Pi. For the γ-ATP inversion experiments (see Figure 6-2b), the curve of γ-ATP is only sensitive to the variance of $T_1^{\gamma\text{-ATP}}$ and not sensitive to any other dynamical parameters. Therefore, the sensitivity simulation of each parameter to the curve fitting gives the important information how to select appropriate constraints for deducing these seven kinetic parameters with the higher reliability. Figures 6-2a and 6-2b also demonstrate that IT measurements (indicated by the circles) have a good agreement with theoretical prediction (indicated by the dotted lines) using dynamic values deduced by the MSS transfer approach.

6.5.2 Whether CK Reaction Can Be Treated as a Two-site Chemical Exchange Model for IT Experiments? How About ATPase Reaction?

The above mentioned questions are tightly correlated to the questions [6-1] and [6-2] in the section of **Introduction** and are critical for accurately measuring the high energy phosphates metabolism. *In vivo* ^{31}P MRS combined with ST or IT strategies are

the fundamental and intensively used tools for the high energy phosphates metabolism studies, in which the chemical exchange reactions among PCr, ATP and Pi were rarely treated as a three-site chemical exchange system. ATPase reaction was commonly ignored for CK reaction studies. Our previous MSS transfer experiments demonstrated that CK and ATPase reactions had to be treated as a three-site chemical exchange system (PCr↔ATP↔Pi) for ST experiments in order to accurately determine both forward and reverse chemical exchange fluxes of CK and ATPase reactions[121].

In contrast, Figure 6-3a and Figure 6-4a indicate that magnetization recovery differences of PCr and γ-ATP for CK reaction predicted by the two-site and three-site chemical exchange model could be ignored despite of selectively inverting PCr or γ-ATP, so that CK reaction can be treated as a two-site chemical exchange system for IT experiments. The reason presumably, is that the ATPase reaction pool is much small ($F_{ATPase} \approx F_{CK}/5$) [121]. It is also evidenced by the dashed line in the plots (a) and (b) of Figure 6-5. Under conditions of $k_{\pm 2}=0$ or [Pi]=0, CK reaction is exactly a two-site chemical exchange system, therefore no any magnetization recovery differences of PCr and γ-ATP between CK reaction processed by the two-site (Equations 6-4a and 6-4b) and three-site chemical exchange model (Equation [6-3d]). With the increased chemical exchange flux of ATPase reaction resulted from the chemical exchange rate constant (indicated by Figure 6-5a) or Pi's concentration (indicated by Figure 6-5b), magnetization recovery differences of CK reaction predicted by the two-site and three-site chemical exchange model becomes larger so that ATPase reaction may have to be taken account

for accurately measuring chemical exchange fluxes of CK reaction. In contrast, ATPase reaction in the human brain has to be treated as a three-site chemical exchange system for the IT experiments because all the parameters of CK have the significant effect on the magnetization recovery behaviors of Pi and γ-ATP when ATPase reaction was treated as a two-site chemical exchange system (see Figures 6-3b, 6-4b and 6-5c as well as 6-5d) compared to three-site chemical exchange system. This conclusion is clearly reflected by the current simulations. For instance, under PCr was selectively inverted if ATPase was treated as a two-site chemical exchange system with ignoring CK reaction, the magnetization recovery of γ-ATP would follow the solid line in the Figure 6-3b. While the IT measurements (see circles in the Figure 6-2a and Figure 6-6) shown that there was a dip following γ-ATP magnetization recovery time curse, which was exactly predicted by the three-site chemical exchange model. Therefore, the current simulations clarify two elusive questions: whether CK reaction and ATPase can be treated as a two-site chemical exchange reaction for IT experiments; and whether inequality of forward and reverse fluxes of CK reaction deduced by the IT approach in the literatures is resulted from the approximation of two-site chemical exchange model.

6.5.3 Kinetic Parameters Deduced by IT Experiments Using the Three-site or Two-site Chemical Exchange Model, Respectively.

Using the three-site chemical exchange model and five independent kinetic parameters with the chemical equilibrium assumption to fit three magnetizations time

courses (indicated as IT^{5p} in Table 6-2), the kinetic parameters for CK reaction are good agreement with that deduced by the MSS transfer approach for PCr or γ-ATP selective inversion experiments. Using this strategy, however, the intrinsic T_1^{Pi} or k_{-2} of ATPase reaction has larger deviations relative to MSS transfer results. Considering that the kinetic parameters (T_1^{Pi} and $k_{\pm 2}$) in ATPase reaction only depend on the curve of Pi magnetization and ATPase reaction has to be treated as a three-site chemical exchange system, in the present study, one curve fitting of Pi magnetization changes as a function of inversion-recovery time was performed using the three-site chemical exchange model to determine two independent parameters of T_1^{Pi} and k_{-2} (the others were fixed and taken from MSS transfer results). With the above constraints, the results of k_{-2} (indicated as $IT^{ATPase-2p}$ in Table 6-2) are much close to the values achieved by the MSS transfer approach. But T_1^{Pi} still has larger deviations compared to the results of MSS transfer method. We have compared two-site and three-site chemical exchange models for CK reaction and found that CK reaction could be treated as a two-site chemical exchange model with a negligible error in the healthy human brain. Therefore, two-curve fitting (i.e., the time courses of magnetizations of PCr and γ-ATP) using the two-site chemical exchange model for CK reaction was performed and the results were summarized in Table 6-2. With the chemical equilibrium assumption and three-parameter fitting (indicated as IT^{CK-3p} in Table 6-2), the results agree well with that of the MSS transfer approach. It also has a good agreement with that deduced by the three-site chemical exchange model with two-curve fitting strategy (indicated as IT^{CK-3p} for the three-site chemical exchange model in Table 6-2, the parameters of ATPase were fixed and came

from MSS transfer approach). So these results further prove that CK reaction can be treated as a two-site chemical exchange system. While, using four-parameters fitting and two-site chemical exchange model (indicated as $IT^{CK\text{-}4p}$ in Table 6-2), the results show large deviations resulting in unequal forward and reverse chemical fluxes. For PCr inversion experiment, Ff is smaller than Fr with Ff//Fr=0.61±0.13 (paired two-tail T-test, $p=3\times10^{-6}$). However Ff is larger than Fr when γ-ATP was inverted with Ff/Fr=1.44±0.16 (paired two-tail T-test, $p=5\times10^{-5}$). The discrepancies indicate again that the reliability of IT method decreases with the increased number of to be fitted variables. So IT method is more challenge especially for the limited data points of inversion recovery time course and larger noise level of ^{31}P MRS.

6.5.4 Comparisons between IT and MSS Transfer Approach for Measuring *in vivo* Chemical Reactions of CK and ATPase

The cure fitting results (see Table 6-2) and simulations of each kinetic parameter to the curve fitting sensitivity (illustrated by dotted lines and circles in Figures 6-2a and 6-2b) also reveal that the kinetic parameters obtained from IT measurements by the appropriate strategy are consistent with that from MSS transfer measurements for CK reaction. The chemical exchange reactions among PCr, ATP and Pi can be described by the ST and IT approach using the three-site global chemical exchange model. Compared to the MSS transfer approach, however, the methodology of IT is much more complicated. Principally, one experiment with selective inversion of PCr or γ-ATP, three

curves of magnetization recovery time courses could be acquired. And the dynamic range of inverted spin is larger (from $-M_0$ to M_0) relative to that of ST experiments with maximum magnetization deduction of around 60% [121]. Each curve of IT measurements includes all the chemical exchange information and it depends on the seven kinetic parameters for the three-site chemical exchange system. However, practically, the available information from the dynamic magnetization recovery time courses is limited and the cure fitting sensitivity is quite different. In practice it is difficult to explore these seven parameters with the higher reliability even using three-curve fitting and additional constraints. For example, IT approach without prior knowledge is difficult to give reliable results of kinetic parameters about ATPase reaction in the brain as illustrated before. It is because that the curves of magnetizations of PCr and γ-ATP are not sensitive to the kinetic parameters of ATPase reaction although these two curves of PCr and γ-ATP have the relative larger dynamic ranges and higher NMR sensitivity. The kinetic parameters of ATPase reaction only depend on the curve of magnetization of Pi. While, the dynamic range of Pi magnetization changes is small (~ 13%) with the larger measurement errors due to the low NMR sensitivity, therefore it unavoidably leads to large curve fitting errors for ATPase reaction. Even for the CK reaction which can be treated as a two-site chemical exchange system for the IT experiments. Three-parameter curve fitting gave the reasonable results, while bi-exponential curve fitting with four kinetic parameters (two intrinsic T_1s of PCr and γ-ATP as well as $k_{\pm 1}$) resulted in the conflicting results: inequality of chemical exchange fluxes, which also have been observed by the others [98]. This is why the IT method is not popularly applied in *in vivo* studies compared with

the ST approach. The MSS transfer approach dramatically simplifies the measurements of the complicated chemical exchange system; and avoids error accumulations from curve fitting or MRS measurements [121]. First, the forward chemical exchange rates of CK and ATPase reactions can be simultaneously obtained via the steady-state saturation of γ-ATP. At this condition, the three-site chemical exchange system can be treated as two independent two-site chemical exchange reactions as PCr↔ATP and ATP↔Pi, respectively. Each time course of magnetizations of PCr and Pi only depends on the two independent parameters (intrinsic spin-lattice relaxation time and the forward chemical exchange rate constant). The curve fitting reliability is high because of single-exponential curve fitting with the two independent parameters and higher dynamic range of magnetizations of PCr and Pi. At the steady state, the magnetizations of PCr and Pi decreased ~60% and ~40%, respectively, at 7T according to our previous measurements [121]. Second, when the magnetization of Pi is fully saturated and the magnetizations of other two chemically coupled spins arrive to the steady-state, the Equation [6-5a] can be deduced from Equation [6-1a]. Similarly the Equation [6-5b] can be deduced from Equation [6-1c] when PCr is completed saturated. Here, all the parameters have the same means as mentioned as before except that Ms* is the steady-state magnetizations with Pi or PCr is fully saturated. The detailed mathematic derivation has been reported before [121]. Therefore, the reverse chemical exchange rate constants (k_{-1} and k_{-2}) can be determined from Equations [6-5a] and [6-5b] through saturating Pi and PCr, respectively [121]. It still only depends on the two parameters (Ms*) because the other parameters in Equations [6-5a] and [6-5b] have been obtained from saturating γ-ATP. Although in

Equation [6-5a] the dynamic ranges of magnetizations of PCr and γ-ATP are small (~ 10% at 7T [121]) but MRS sensitivities of PCr and γ-ATP are relatively high. The MRS sensitivity of Pi in Equation [6-5b] is low while the dynamic changes of γ-ATP and Pi are larger. The magnetizations of γ-ATP and Pi decreased ~ 40% and ~ 20%, respectively, when PCr was full saturated at 7T [121]. Thirdly, it has been approved that the intrinsic spin-lattice relaxation time is a constant and doesn't change with pathological or physiological conditions at a given magnetic field [95]. Therefore, with prior knowledge of the intrinsic spin-lattice relaxation times of PCr and Pi, the MSS transfer approach could be further simplified: three spectra with separately saturating three chemically coupled spins and one control can be deduced all the kinetic parameters including four chemical exchange rates. In contrast, even if the same strategy is applied for the IT approach, it still could not give the reliable results of the forward and reverse chemical exchange rates of CK and ATPase reactions using three-site chemical exchange model with the known T_1s of PCr, γ-ATP and Pi (illustrated as IT^{4p} in Table 6-2).

$$k_{-1} = \alpha_a \left(\frac{M_a^{*c}}{M_a^0} - \frac{T_{1a}^{-1}}{\alpha_a}\right)\frac{M_a^0}{M_b^{*c}} \qquad [6-5a]$$

$$k_{-2} = \alpha_b \left(\frac{M_b^{*a}}{M_b^0} - \frac{T_{1b}^{-1}}{\alpha_b}\right)\frac{M_b^0}{M_c^{*a}} \qquad [6-5b]$$

6.5.5 The Possible Impact of Subcellular Compartments on the ^{31}P Magnetization ST or IT Approach Based on the Global Three-site Chemical Exchange Model

The CK enzymes play a key role in the energy metabolism [123]. And the majority of CK enzymes in the brain is found in two cytosolic isoforms ('muscle-type' CK, M-CK and brain-type CK, B-CK) and two mitochondria isoforms (ubiquitous Mia-CK and sarcomeric Mib-CK), which together constitute an intricate cellular energy buffering and transport system connecting intracellular site of high energy phosphate consumption (cytosol) with sites of energy production (mitochondria) [122]. Mi-CK is believed to tightly couple to oxidative phosphorylation and convert ATP to PCr as the energy storage. It may also regulate the concentrations of ADP as well as Cr for providing constant resource for ATP generation. PCr in the mitochondrion, as a net product of oxidative phosphorylation, diffuses to the cytosolic CK reaction pool. The similar compartmental reaction between ATP and Pi exists in the mitochondrion and cytosol for ATP generation and utilization, respectively. While the current knowledge of biochemistry are far beyond understanding this complicated mechanism of energy metabolism. The concentration distributions and kinetic chemical reaction rates among PCr, ATP and Pi in the subcellar compartments are still unknown in the brain [127]. Obviously the concentrations measured by ^{31}P MRS come from the whole tissue covered by NMR detection coil and explanations of NMR data always depend on the chemical exchange model. Our current IT experiment and previous MSS transfer approach indicate the chemical exchange reactions among PCr, ATP and Pi could be described by the global three-site chemical exchange model. The current study indicates that the inequality

of Ff and Fr for CK reaction deduced by the IT approach in the previous reports is not due to the subcellualr compartment reactions, rather than IT method itself limitations: multiple exponential analyses, too many parameters entangled together and relatively large measurement error (small dynamic range and low signal noise ratio of Pi). The argument about the complication attributed by subcellular compartments based on the observation of inequality between the forward and reverse CK fluxes deduced from ^{31}P IT experiment in the literatures is not convincible. In contrast, MSS transfer measurements demonstrate that chemical exchange reaction of CK and ATPase are satisfied the thermal equilibrium condition. In other words, the ATP synthesis rates equal to its utilizations rates. In addition, MSS transfer results have also revealed that the forward ATPase flux determined by our global PCr↔ATP↔Pi exchange model reflects the oxidative phosphorylation rate [121], which is tightly linked to the mitochondrial function and activity [65]. Therefore chemical exchange fluxes based on the simple global model could predict the energy production, utilization and transportation at the global level regardless of its kinetic complexity of subcellular compartments [128]. One possible explanation is that the diffusion of substrates of CK and ATPase reactions between enzyme populations is much faster than their inter-conversion rates, hence the whole tissue could be considered as a single pool. Another possible explanation is that the flux of CK reaction is much faster than that of ATPase reaction so that it further smoothes the im-homogeneity of compartmental chemical reactions.

6.6 Conclusion

The chemical exchange reactions of CK and ATPase related to the cerebral high energy phosphates metabolism can be described by the ST and IT approaches based on the three-site global chemical exchange model. The kinetic parameters deduced from MSS transfer method satisfied well with the magnetization recovery time curves predicted by the IT approach. While the IT method itself is difficult to give the reliable results due to requirements of multiple exponential analysis with too many parameters and relatively large experimental measurement errors. The present study clearly identifies that in-equality of forward and reverse flux of CK reaction before deduced by the IT approach is not due to the two-site chemical exchange model or the complexity of sub-cellular compartmental reactions. MSS transfer approach has huge potential to be intensively used to detect high energy phosphates metabolism. These findings should be crucial for the *in vivo* ^{31}P MRS study of brain or heart bioenergetics at various physiological and/or pathological conditions.

6.7 Acknowledgements

This work was partially supported by NIH grants NS39043, NS41262, EB00329, P41 RR08079 and P30NS057091; the W.M. Keck Foundation and MIND institute. The authors gratefully acknowledge Dr. Peter Andersen for technical assistance and Dr. Xiao-Hong Zhu for insightful discussion.

In the preparation of manuscript by Fei Du, Hongyan Qiao and Wei Chen.

7. CONCLUSIONS

In this thesis, first, we briefly reviewed the background and significance of *in vivo* MRS technology and studies. Then, we focused on three specific aspects. The three specific topics addressed are as follows:

- *In vivo* ^{31}P MRS of Human Brain at High/Ultrahigh Fields: A Quantitative Comparison of Signal-to-Noise Ratio and Spectral Resolution between 4 Tesla and 7 Tesla;

The results from this study clearly indicate the great advantages and benefits of *in vivo* ^{31}P MRS at 7T in terms of improvements in both detection sensitivity and spectral resolution. Such improvements should (i) make *in vivo* high-field ^{31}P MRS more capable for precisely determining phosphate metabolites, phospholipids and chemical exchange kinetic rates noninvasively (e.g., the measurement of the ATP synthesis rate in the human visual cortex [65]); and (ii) dramatically improve the reliability and applicability of *in vivo* ^{31}P MRS for noninvasively studying high-energy phosphate metabolism and biogenetics in the human brain and other organs (e.g., heart and skeletal muscle) at both normal and diseased states.

- Differentiating High-energy Phosphate Metabolites and pH in Human Gray and White Matters by using 3D ^{31}P Chemical Shift Imaging of Entire Brain at 7 Tesla;

Excellent ^{31}P NMR sensitivity and improved spectral resolution achieved at 7 Tesla are capable of determining small differences of the measurable parameters between the gray matter and white matter reliably. This study suggests that ultra-high field strength is significantly advantageous for performing *in vivo* ^{31}P spectroscopy on human brain for better quantification, thus, it provides a great opportunity for noninvasive study of phosphate bioenergetics related to brain function and neuropathology.

- Non-invasively Determining Kinetic Network of ATP Metabolism in Human Brain: Saturation Transfer Approach and Inversion Transfer Approach.

An *in vivo* ^{31}P MT approach based on multiple single-site saturation measurements was developed to noninvasively determine all rate constants in the PCr↔ ATP ↔ Pi kinetic network and four associated ATP metabolic fluxes in the human brain. The quantification used in this approach is based on solving multiple Bloch equations that account for all three exchangeable phosphate metabolites (or spins). Our results indicate that one must treat the PCr ↔ ATP ↔ Pi chemical exchange reactions as a three-spin exchange system to accurately determine the reverse rate constants and reverse fluxes for both the CK and ATPase reactions. The ratios of forward and reverse fluxes measured in the human occipital lobe using the MSS MT approach satisfied the chemical equilibrium condition. The MSS MT approach only requires one control and three saturated ^{31}P spectra to determine all kinetic parameters involved in the PCr↔ ATP ↔ Pi

kinetic network. This noninvasive approach should provide an important neuroimaging modality for quantitatively studying the fundamental ATP metabolism and its impact on cerebral bioenergetics associated with brain function and brain activation.

The chemical exchange reactions of CK and ATPase related to the cerebral high energy phosphates metabolism can be described by the MSST and IT approaches based on the three-site global chemical exchange model. The kinetic parameters deduced from MSST method satisfied well with the magnetizations recovery time curves predicted by the IT approach. While the IT method itself is difficult to give the reliable results due to requirements of multiple-exponential analysis with too many parameters and relatively large experimental measurement errors. The present study clearly identifies that in-equality of forward and reverse flux of CK reaction before deduced by the IT approach is not due to the two-site chemical exchange model or the complexity of sub-cellular compartmental reactions. These findings should be crucial for the *in vivo* ^{31}P MRS study of brain bioenergetics at various physiological and/or pathological conditions.

In addition, our results reveal that the forward ATPase flux determined by the *in vivo* ^{31}P MT approach equals the oxidative phosphorylation rate. At normal physiological conditions, the ATP synthesis rate is tightly coupled to the oxygen metabolism rate in the brain. However, such coupling may break down in pathological conditions. For instance, damage to the mitochondrial DNA in neurons has been implicated in both Parkinson's disease and Alzheimer's disease. Also, some of the mitochondrial DNA mutations found in Alzheimer's disease patients have been associated with defects in oxidative

phosphorylation in mitochondria [118]. Thus, the *in vivo* ^{31}P MT approach may play an important role in studying a variety of neurodegenerative diseases associated with mitochondrial abnormalities and metabolic syndrome.

REFERENCES

1. Lauterbur, P.C., *Image Formation by Induced Local Interaction: Examples Employing Nuclear Magnetic Resonance.* Nature, 1973. **242**: p. 190-191.
2. Smith, I.C.a.D.E.B., *Nuclear magnetic resonance spectroscopy.* Anal Chem, 1995. **67**(12): p. 509R-518R.
3. Bloch, *Nuclear Induction.* Phys Rev, 1946. **69**: p. 127.
4. Purcell, *Resonance Absorption by Nuclear Magnetic Moments in a Solid.* Phys Rev, 1946. **69**: p. 37.
5. Moon, R.B. and J.H. Richards, *Determination of intracellular pH by 31P magnetic resonance.* J Biol Chem, 1973. **248**(20): p. 7276-8.
6. Gadian, D.G., et al., *NMR spectroscopy: current status and future possibilities.* Acta Neurochir Suppl (Wien), 1993. **57**: p. 1-8.
7. Passe, T.J., et al., *Nuclear magnetic resonance spectroscopy: a review of neuropsychiatric applications.* Prog Neuropsychopharmacol Biol Psychiatry, 1995. **19**(4): p. 541-63.
8. Dawson, B.A. and D.B. Black, *Utilizing nuclear magnetic resonance (NMR) spectroscopy for assessing nadolol racemate composition.* J Pharm Biomed Anal, 1995. **13**(1): p. 39-44.
9. Frahm J, M.K., Hanicke W., *Localized proton spectroscopy using stimulated echoes.* J Magn Reson, 1987. **72**: p. 502-508.

10. Ordidge RJ, C.A., Lohman JAB., *Imageselected in vivo spectroscopy (ISIS). A new technique for spatially selective NMR spectroscopy.* J Magn Reson, 1986. **66**: p. 283-294.

11. PA., B., *Spatial localization in NMR spectroscopy in vivo.* Ann N Y Acad Sci, 1987. **508**: p. 333-348.

12. Muller S, S.R., Weber H, Seelig J., *Multivolume selective spectroscopy.* J Magn Reson, 1988. **76**: p. 155-161.

13. Ordidge RJ, B.R., McHale G., *A general approach to selection of multiple cubic volume elements using the ISIS technique.* Magn Reson Med, 1988. **8**: p. 323-331.

14. Chen W, N.E., Rothman DL, Shulman RG., *Simultaneous measurements of regional C4 glutamate from two localized volumes in human brain using ^{1}H-(^{13}C) NMR spectroscopy.* 2nd Scientific Meeting of the Society of Magnetic Resonance,, 1994: p. 562.

15. Souza SP, S.J., Dumoulin CL, Plewes DP, Glover G., *SIMA: simultaneous multislice acquisition of MR images by Hadamard-encoded excitation.* J Comput Assist Tomogr, 1988. **12**: p. 1026-1030.

16. Goelman G, W.G., Leigh JS., *Hadamard spectroscopic imaging technique as applied to study human calf muscles.* Magn Reson Med, 1992. **25**: p. 349-354.

17. Dreher W, L.D., *Double-echo multislice proton spectroscopic imaging using Hadamard slice encoding.* Magn Reson Med, 1994. **31**: p. 596-600.

18. McDonald S, W.W., *Uses of shaped pulses in NMR.* Concepts Magn Reson, 1991. **3**: p. 55-81.

19. Brown TR, K.B., Ugurbil K., *NMR chemical shift imaging in three dimensions.* Proc Natl Acad Sci USA, 1982. **79**: p. 3523-3526.

20. Hu X, C.W., Patel M, Ugurbil K., *Chemical shift imaging: an introduction to its theory and practice.* Bronzino JD, editor. Biomedical engineering handbook., 1995: p. 1036-1045.

21. Twieg DB, H.H., Ponder SL, den Hollander J, Pohost GM., *Spatial resolution in ^{31}P metabolite imaging of the human brain at 4.1 T.* J Magn Reson B, 1994. **104**: p. 153-158.

22. Garwood M, S.T., Bendall MR, Pegg DT., *Improved Fourier series windows for localization in in vivo NMR spectroscopy.* J Magn Reson, 1985. **65**: p. 510.

23. Hendrich K, H.X., Menon R, Merkle H, Camarata P, Heros R, et al., *Spectroscopic imaging of circular voxels with a two-dimensional Fourier series Window technique.* J Magn Reson, 1994. **105**: p. 225-232.

24. Garwood M, R.P., Ugurbil K., *Fourier series windows on and off-resonance using multiple coils and longitudinal modulation.* J Magn Reson, 1987. **75**: p. 244-261.

25. Chance, B., et al., *Detection of ^{31}P nuclear magnetic resonance signals in brain by in vivo and freeze-trapped assays.* Proc Natl Acad Sci U S A, 1978. **75**(10): p. 4925-9.

26. Brown, G.G., et al., *In vivo ^{31}P NMR profiles of Alzheimer's disease and multiple subcortical infarct dementia.* Neurology, 1989. **39**(11): p. 1423-7.

27. Brown, T.R., K. Ugurbil, and R.G. Shulman, *^{31}P Nuclear Magnetic Resonance Kinetic Measurements of ATPase kinetics in aerobic escherichia coli cells.* Proc. Natl. Acad. Sci. USA, 1977. **74**: p. 5551-5553.

28. Ackerman, J.J.H., et al., *Mapping of metabolites in whole animals by ^{31}P NMR using surface coils.* Nature, 1980. **283**: p. 167-170.

29. Bourne, R.M., *A ^{31}P-NMR study of phosphate transport and compartmentation in Candida utilis.* Biochim Biophys Acta, 1990. **1055**(1): p. 1-9.

30. Thiaudiere, E., et al., *Compartmentation of inorganic phosphate in perfused rat liver. Can cytosol be distinguished from mitochondria by ^{31}P NMR?* FEBS Lett, 1993. **330**(2): p. 231-5.

31. Stier, A., et al., *^{31}P-NMR spectroscopy of phosphate compartmentation during ischaemia in hearts protected by cardioplegic treatment.* Free Radic Res Commun, 1989. **7**(3-6): p. 293-300.

32. Prichard, J.W. and R.G. Shulman, *NMR spectroscopy of brain metabolism in vivo.* Annu Rev Neurosci, 1986. **9**: p. 61-85.

33. Matthews, P.M., et al., *^{31}P-NMR studies of metabolite compartmentation in Fasciola hepatica.* Biochim Biophys Acta, 1985. **845**(2): p. 178-88.

34. Thoma, W.J. and K. Ugurbil, *pH and compartmentation of isolated perfused rat liver studied by ^{31}P and ^{19}F NMR.* NMR Biomed, 1988. **1**(2): p. 95-100.

35. Lei, H., et al., *In vivo ^{31}P magnetic resonance spectroscopy of human brain at 7 T: an initial experience.* Magn Reson Med, 2003. **49**(2): p. 199-205.

36. Adam, W.R., A.P. Koretsky, and M.W. Weiner, *Measurement of renal intracellular pH by ^{31}P NMR. Relationship of pH to ammoniagenesis.* Contrib Nephrol, 1985. **47**: p. 15-21.

37. Adam, W.R., A.P. Koretsky, and M.W. Weiner, *^{31}P-NMR in vivo measurement of renal intracellular pH: effects of acidosis and K+ depletion in rats.* Am J Physiol, 1986. **251**(5 Pt 2): p. F904-10.

38. Avison, M.J., H.P. Hetherington, and R.G. Shulman, *Applications of NMR to studies of tissue metabolism.* Annu Rev Biophys Biophys Chem, 1986. **15**: p. 377-402.

39. Ugurbil, K., *Magnetization Transfer Measurements of Individual Rate Constants in the Presence of Multiple Reactions.* J. Magn. Reson., 1985. **64**: p. 207-219.

40. Ugurbil, K., *Magnetization Transfer Measurements of Creatine Kinase and ATPase Rates in Intact Hearts.* Circulation, 1985. **72**(Supp. IV): p. IV94- IV96.

41. Kupriyanov, V.V., et al., *Combination of ^{31}P-NMR magnetization transfer and radioisotope exchange methods for assessment of an enzyme reaction mechanism: rate-determining steps of the creatine kinase reaction.* Biochim Biophys Acta, 1990. **1020**(3): p. 290-304.

42. Brindle, K.M., et al., *^{31}P NMR magnetization-transfer measurements of ATP turnover during steady-state isometric muscle contraction in the rat hind limb in vivo.* Biochemistry, 1989. **28**(11): p. 4887-93.

43. Brindle, K.M., *^{31}P NMR magnetization-transfer measurements of flux between inorganic phosphate and adenosine 5'-triphosphate in yeast cells genetically*

modified to overproduce phosphoglycerate kinase. Biochemistry, 1988. **27**(16): p. 6187-96.

44. Chen, W., et al., *Increase of creatine kinase activity in the visual cortex of human brain during visual stimulation: a ^{31}P NMR magnetization transfer study.* Magn Reson Med, 1997. **38**: p. 551-557.

45. Sheldon, J.G., et al., *^{31}P NMR magnetization transfer study of the control of ATP turnover in Saccharomyces cerevisiae.* Proc Natl Acad Sci U S A, 1996. **93**(13): p. 6399-404.

46. Chu, W.J., et al., *Lateralization of human temporal lobe epilepsy by ^{31}P NMR spectroscopic imaging at 4.1 T.* Neurology, 1998. **51**(2): p. 472-9.

47. Hoang, T.Q., et al., *Quantitative proton-decoupled ^{31}P MRS and ^{1}H MRS in the evaluation of Huntington's and Parkinson's diseases.* Neurology, 1998. **50**(4): p. 1033-40.

48. Sappey-Marinier, D., et al., *Effect of photic stimulation on human visual cortex lactate and phosphates using ^{1}H and ^{31}P magnetic resonance spectroscopy.* J Cereb Blood Flow Metab, 1992. **12**(4): p. 584-92.

49. Rango, M., et al., *Brain activation in normal subjects and in patients affected by mitochondrial disease without clinical central nervous system involvement: a phosphorus magnetic resonance spectroscopy study.* J Cereb Blood Flow Metab, 2001. **21**(1): p. 85-91.

50. Barfuss, H., et al., *In vivo magnetic resonance imaging and spectroscopy of humans with a 4 T whole-body magnet.* NMR Biomed, 1990. **3**(1): p. 31-45.

51. Twieg, D.B., et al., *Spatial resolution in ^{31}P metabolite imaging of the human brain at 4.1 T.* J Magn Reson B, 1994. **104**(2): p. 153-8.

52. Hetherington, H.P., et al., *Biological and clinical MRS at ultra-high field.* NMR Biomed, 1997. **10**(8): p. 360-71.

53. Aulabaugh, A., W.P. Niemczura, and W.A. Gibbons, *High field proton NMR studies of tryptic fragments of calmodulin: a comparison with the native protein.* Biochem Biophys Res Commun, 1984. **118**(1): p. 225-32.

54. Sharp, J.C. and M.O. Leach, *Conformal NMR spectroscopy: accurate localization to noncuboidal volumes with optimum SNR.* Magn Reson Med, 1989. **11**(3): p. 376-88.

55. Cecil, K.M., et al., *High-field proton magnetic resonance spectroscopy of a swine model for axonal injury.* J Neurochem, 1998. **70**(5): p. 2038-44.

56. Castellanos, M.E. and J.C. Rosenwald, *Evaluation of the scatter field for high-energy photon beam attenuators.* Phys Med Biol, 1998. **43**(2): p. 277-90.

57. Shulman, R.G., et al., *Cellular applications of ^{31}P and ^{13}C nuclear magnetic resonance.* Science, 1979. **205**(4402): p. 160-6.

58. Weiner, M.W., *NMR spectroscopy for clinical medicine. Animal models and clinical examples.* Ann N Y Acad Sci, 1987. **508**: p. 287-99.

59. Ross, B.M., et al., *Phospholipid biosynthetic enzymes in human brain.* Lipids, 1997. **32**(4): p. 351-8.

60. Welch, K.M., et al., *Magnetic resonance spectroscopy in cerebral ischemia.* Neurol Clin, 1992. **10**(1): p. 1-29.

61. Hetherington, H.P., J.W. Pan, and D.D. Spencer, *^{1}H and ^{31}P spectroscopy and bioenergetics in the lateralization of seizures in temporal lobe epilepsy.* J Magn Reson Imaging, 2002. **16**(4): p. 477-83.

62. Pettegrew, J.W. and N.J. Minshew, *Molecular insights into schizophrenia.* J Neural Transm Suppl, 1992. **36**: p. 23-40.

63. Frosen, S. and R.A. Hoffman, *Study of moderately rapid chemical exchange by means of nuclear magnetic double resonance.* J. Chem. Phys., 1963. **39**: p. 2892-2901.

64. Alger, J.R. and R.G. Shulman, *NMR studies of enzymatic rates in vitro and in vivo by magnetization transfer.* Quarterly Reviews of Biophysics, 1984. **17**(1): p. 83-124.

65. Lei, H., K. Ugurbil, and W. Chen, *Measurement of unidirectional Pi to ATP flux in human visual cortex at 7 T by using in vivo ^{31}P magnetic resonance spectroscopy.* Proc Natl Acad Sci U S A, 2003. **100**(24): p. 14409-14.

66. Barker, P.B., D.O. Hearshen, and M.D. Boska, *Single-voxel proton MRS of the human brain at 1.5T and 3.0T.* Magn Reson Med, 2001. **45**(5): p. 765-9.

67. Gonen, O., et al., *Multivoxel 3D proton spectroscopy in the brain at 1.5 versus 3.0 T: signal-to-noise ratio and resolution comparison.* AJNR Am J Neuroradiol, 2001. **22**(9): p. 1727-31.

68. Tkac, I., et al., *In vivo ^{1}H NMR spectroscopy of the human brain at 7 T.* Magn Reson Med, 2001. **46**(3): p. 451-6.

69. Boska, M.D., et al., *Comparison of ^{31}P MRS and ^{1}H MRI at 1.5 and 2.0 T.* Magn Reson Med, 1990. **13**(2): p. 228-38.

70. Hardy, C.J., et al., *Rapid ^{31}P spectroscopy on a 4-T whole-body system.* Magn Reson Med, 1988. **8**(1): p. 104-9.

71. Hetherington, H.P., et al., *Quantitative ^{31}P spectroscopic imaging of human brain at 4 Tesla: assessment of gray and white matter differences of phosphocreatine and ATP.* Magn Reson Med, 2001. **45**: p. 46-52.

72. Ernst, R.R., G. Bodenhausen, and A. Wokaun, *Principles of Nuclear Magnetic Resonance in One and Two Dimensions*. 1991, New York: Oxford University Press.

73. Hoult, D.I. and R.E. Richards, *The signal-to-noise ratio of nuclear magnetic resonance experiment.* J Magn Reson, 1976. **24**: p. 71-85.

74. Silver, M.S., et al., *Selective population inversion in NMR.* Nature, 1984. **310**(5979): p. 681-3.

75. Hendrich, K., et al., *Spectroscopic imaging of circular voxels with a two-dimensional Fourier-series window technique.* Journal of Magnetic Resonance, 1994. **105**: p. 225-32.

76. Wang, Z., et al., *Sensitivity of in vivo MRS of the N-delta proton in proximal histidine of deoxymyoglobin.* Magn Reson Med, 1992. **27**(2): p. 362-7.

77. Evelhoch, J.L., et al., *^{31}P spin-lattice relaxation times and resonance linewidths of rat tissue in vivo: dependence upon the static magnetic field strength.* Magn Reson Med, 1985. **2**(4): p. 410-7.

78. Mathur-De Vre, R., C. Maerschalk, and C. Delporte, *Spin-lattice relaxation times and nuclear Overhauser enhancement effect for ^{31}P metabolites in model solutions at two frequencies: implications for in vivo spectroscopy.* Magn Reson Imaging, 1990. **8**(6): p. 691-8.

79. Vaughan, J.T., et al., *7T vs. 4T: RF power, homogeneity, and signal-to-noise comparison in head images.* Magn Reson Med, 2001. **46**(1): p. 24-30.

80. Zhu, X.H., et al., *^{17}O relaxation time and NMR sensitivity of cerebral water and their field dependence.* Magn Reson Med, 2001. **45**(4): p. 543-9.

81. X.H. Zhu, e.a., Proceedings of ISMRM, 2003: p. 126.

82. Garwood, M., et al., *Improved Fourier series windows for localization in in vivo NMR spectroscopy.* J. Magn. Reson., 1985. **65**: p. 510.

83. Garwood, M., P.M. Robitaille, and K. Ugurbil, *Fourier series windows on and off-resonance using multiple coils and longitudinal modulation.* J. Magn. Reson., 1987. **75**: p. 244-261.

84. Menon, R.S., et al., *^{31}P NMR spectroscopy of the human heart at 4 T: detection of substantially uncontaminated cardiac spectra and differentiation of subepicardium and subendocardium.* Magn Reson Med, 1992. **26**(2): p. 368-76.

85. Barker, P.B., et al., *Magnesium and pH imaging of the human brain at 3.0 Tesla.* Magn Reson Med, 1999. **41**(2): p. 400-6.

86. Siesjo, B.K., *Brain energy metabolism*. 1978, New York: Wiley. 101-110.

87. Attwell, D. and S.B. Laughlin, *An energy budget for signaling in the grey matter of the brain.* Journal of Cerebral Blood Flow & Metabolism, 2001. **21**(10): p. 1133-45.

88. Slater, E.C. and F.A. Holton, *Oxidative phosphorylation coupled with the oxidation of alpha-ketoglutarate by heart-muscle sarcosomes. I. Kinetics of the oxidative phosphorylation reaction and adenine nucleotide specificity.* Biochem J, 1953. **55**(3): p. 530-44.

89. Kemp, G.J., *Non-invasive methods for studying brain energy metabolism: what they show and what it means.* Dev Neurosci, 2000. **22**(5-6): p. 418-28.

90. Saks, V.A., R. Ventura-Clapier, and M.K. Aliev, *Metabolic control and metabolic capacity: two aspects of creatine kinase functioning in the cells.* Biochim Biophys Acta, 1996. **1274**(3): p. 81-8.

91. Shoubridge, E.A., R.W. Briggs, and G.K. Radda, *^{31}P NMR saturation transfer measurements of the steady state rates of creatine kinase and ATP synthetase in the rat brain.* FEBS Lett, 1982. **140**(2): p. 289-92.

92. Balaban, R.S., H.L. Kantor, and J.A. Ferretti, *In vivo flux between phosphocreatine and adenosine triphosphate determined by two-dimensional phosphorous NMR.* J Biol Chem, 1983. **258**(21): p. 12787-9.

93. Degani, H., et al., *^{31}P magnetization transfer studies of creatine kinase kinetics in living rabbit brain.* Magn Reson Med, 1987. **5**(1): p. 1-12.

94. Bottomley, P.A. and C.J. Hardy, *Mapping creatine kinase rates in human brain and heart with 4 tesla Saturation transfer ^{31}P NMR.* J. Magn. Reson., 1992. **99**: p. 443-448.

95. Sauter, A. and M. Rudin, *Determination of creatine kinase kinetic parameters in rat brain by NMR magnetization transfer. Correlation with brain function.* J Biol Chem, 1993. **268**(18): p. 13166-71.

96. Chen, W., et al., *Increase of creatine kinase activity in the visual cortex of human brain during visual stimulation: a ^{31}P magnetization transfer study.* Magn Reson Med, 1997. **38**(4): p. 551-7.

97. Braunova, Z., et al., *Metabolic changes in rat brain after prolonged ethanol consumption measured by ^{1}H and ^{31}P MRS experiments.* Cell Mol Neurobiol, 2000. **20**(6): p. 703-15.

98. Joubert, F., et al., *CK flux or direct ATP transfer: versatility of energy transfer pathways evidenced by NMR in the perfused heart.* Mol Cell Biochem, 2004. **256-257**(1-2): p. 43-58.

99. Weiss, R.G., G. Gerstenblith, and P.A. Bottomley, *ATP flux through creatine kinase in the normal, stressed, and failing human heart.* Proc Natl Acad Sci U S A, 2005. **102**(3): p. 808-13.

100. Mlynarik v, Z.S., Brehm A, Bischof M, Roden M, *An optimized protocol for measuring rate constant of creatine kinase reaction in human brain by 31P NMR saturation transfer.* 13th Proc. Intl. Soc. Mag. Reson. Med., 2005: p. 2767.

101. Matthews, P.M., et al., *A ^{31}P-NMR saturation transfer study of the regulation of creatine kinase in the rat heart.* Biochim Biophys Acta, 1982. **721**(3): p. 312-20.

102. Mora, B.N., P.T. Narasimhan, and B.D. Ross, *^{31}P magnetization transfer studies in the monkey brain.* Magn Reson Med, 1992. **26**(1): p. 100-15.

103. Bittl, J.A., J. DeLayre, and J.S. Ingwall, *Rate equation for creatine kinase predicts the in vivo reaction velocity: ^{31}P NMR surface coil studies in brain, heart, and skeletal muscle of the living rat.* Biochemistry, 1987. **26**(19): p. 6083-90.

104. Nunnally, R.L. and D.P. Hollis, *Adenosine triphosphate compartmentation in living hearts: a phosphorus nuclear magnetic resonance saturation transfer study.* Biochemistry, 1979. **18**(16): p. 3642-6.

105. Zahler, R. and J.S. Ingwall, *Estimation of heart mitochondrial creatine kinase flux using magnetization transfer NMR spectroscopy.* Am J Physiol, 1992. **262**(4 Pt 2): p. H1022-8.

106. Ugurbil, K., et al., *Measurement of an individual rate constant in the presence of multiple exchanges: application to myocardial creatine kinase reaction.* Biochemistry, 1986. **25**(1): p. 100-7.

107. Ugurbil, K., *Magnetization-Transfer Measurements of Individual Constants in the Presence of Multiple Reactions.* Journal of Magnetic Resonance, 1985. **64**: p. 207-219.

108. Spencer, R.G., et al., *ATP synthesis and degradation rates in the perfused rat heart. ^{31}P-nuclear magnetic resonance double saturation transfer measurements.* Biophys J, 1988. **54**(5): p. 921-9.

109. Degani, H., et al., *Kinetics of creatine kinase in heart: a ^{31}P NMR saturation- and inversion-transfer study.* Biochemistry, 1985. **24**(20): p. 5510-6.

110. Gruetter, R., *Automatic, localized in vivo adjustment of all first- and second-order shim coils.* Magn Reson Med, 1993. **29**(6): p. 804-11.

111. de Graaf, R.A., et al., *B1-insensitive, single-shot localization and water suppression.* J Magn Reson B, 1996. **113**(1): p. 35-45.

112. Lorek, A., et al., *Delayed ("secondary") cerebral energy failure after acute hypoxia-ischemia in the newborn piglet: continuous 48-hour studies by phosphorus magnetic resonance spectroscopy.* Pediatr Res, 1994. **36**(6): p. 699-706.

113. Erecinska, M. and I.A. Silver, *ATP and brain function.* J Cereb Blood Flow Metab, 1989. **9**(1): p. 2-19.

114. Siesjo, B.K., et al., *Extra- and intracellular pH in the brain during seizures and in the recovery period following the arrest of seizure activity.* J Cereb Blood Flow Metab, 1985. **5**(1): p. 47-57.

115. Gilboe, D.D., et al., *NMR-based identification of intra- and extracellular compartments of the brain Pi peak.* J Neurochem, 1998. **71**(6): p. 2542-8.

116. Fox, P.T., et al., *Nonoxidative glucose consumption during focal physiologic neural activity.* Science, 1988. **241**: p. 462-464.

117. PC., H., *P/O ratios of mitochondrial oxidative phosphorylation.* Biochim Biophys Acta, 2005. **1706**: p. 1-11.

118. Wallace, D.C., *Mitochondrial genetics: a paradigm for aging and degenerative diseases?* Science, 1992. **256**(5057): p. 628-32.

119. Leibfritz, D. and W. Dreher, *Magnetization transfer MRS.* NMR Biomed, 2001. **14**(2): p. 65-76.

120. Sture Forsen, R.A.H., *Study of moderately rapid chemical exchange reactions by means of nuclear magnetic resonance.* The Journal of Chemical Physics, 1963. **39**(11): p. 2892-2901.

121. Du, F., et al., *Efficient in vivo ^{31}P magnetization transfer approach for noninvasively determining multiple kinetic parameters and metabolic fluxes of ATP metabolism in the human brain.* Magn Reson Med, 2007. **57**(1): p. 103-14.

122. Friedman, D.L. and R. Roberts, *Compartmentation of brain-type creatine kinase and ubiquitous mitochondrial creatine kinase in neurons: evidence for a creatine phosphate energy shuttle in adult rat brain.* J Comp Neurol, 1994. **343**(3): p. 500-11.

123. Hemmer, W. and T. Wallimann, *Functional aspects of creatine kinase in brain.* Dev Neurosci, 1993. **15**(3-5): p. 249-60.

124. Loan, C. and C. Moler, *Nineteen Dubious Ways to Compute the Exponential of A Matrix.* Siam Review, 1978. **20**(4): p. 801-836.

125. DeFuria, R.R., M.K. Dygert, and G.M. Alachi, *Computer simulation of the ^{31}P NMR equations governing the creatine kinase reaction.* J Theor Biol, 1985. **114**(1): p. 75-91.

126. van den Boogaart, A., et al. *MRUI: a graphical user interface for accurate routine MRS data analysis*. in *13th Annual Meeting of ESMRMB*. 1996. Prague.

127. Matsushima, K., et al., *Comparison of kinetic constants of creatine kinase isoforms.* Int J Biol Macromol, 2006. **38**(2): p. 83-8.

128. Du, F., et al., *Tightly coupled brain activity and cerebral ATP metabolic rate.* Proc Natl Acad Sci U S A, 2008. **105**(17): p. 6409-14.